ALMA MATER STUDIORUM
UNIVERSITÀ DI BOLOGNA

DOTTORATO DI RICERCA IN
ASTROFISICA

Ciclo XXXVI

# Searching for Fossil Fragments into the Galactic Bulge

Presentata da: **Chiara Crociati**

Coordinatore Dottorato:
**Prof. Andrea Miglio**

Supervisore:
**Prof. Francesco R. Ferraro**

Co-supervisori:
**Dr. Cristina Pallanca**
**Dr. Elena Valenti**
**Dr. Emanuele Dalessandro**
**Prof. Barbara Lanzoni**

Esame finale anno 2024

Settore Concorsuale: 02/C1 – Astronomia, Astrofisica, Fisica della Terra e dei Pianeti
Settore Scientifico Disciplinare: FIS/05 – Astronomia e Astrofisica

# Abstract

The exact mechanism that drove the formation of the bulge in the Milky Way and in analogous galaxies is still largely debated. Thanks to the photometric and spectroscopic surveys that had been performed over the last twenty years, the observed 3D shape of the Galactic bulge, as well as the chemistry and kinematics of its stars, were unveiled, suggesting that its formation mechanism may had been composite. Two main formation channels are currently invoked to reproduce the observed chemodynamical properties of the Milky Way's inner region: on the one hand, the global barred and X-shaped morphology, together with cylindrical kinematics, would suggest a dynamical secular evolution of the disk driven by bar and buckling instabilities; on the other hand, the dominant old ages and the chemical pattern of its stars require a very short assembly timescale ($1 - 2\,\mathrm{Gyr}$), more compatible with a strong gas accretion mechanism, early mergers or the coalescence at high redshift of massive clumps formed from the fragmentation of the turbulent primordial gas-rich disk. The latter hypothesis is known as the *clump-origin* or *merging* scenario.

More specifically, the merging scenario is supported by the ubiquitous observation of massive ($10^{7-9}\,M_{\odot}$) star forming clumps in disk galaxies at cosmic-noon, and by clumpy numerical simulations able to naturally reproduce the required timescales and the chemistry of the bulge. Yet, its actual contribution to the bulge assembly is still questioned. On the basis of current observations, it is very challenging to evaluate if high-redshift clumps survive long enough (due to feedback processes, field tidal forces, etc.) to migrate to the central region of the host galaxy. On the other hand, hints that a fraction of star-forming clumps can actually survive come from the observed gradients of their mass. Moreover, recent theoretical studies show that not only the massive clumps are able to migrate to the center, but some of them are also able to survive and to generate stellar clusters. It is likely that the primordial clumps were massive enough to retain a fraction of iron-enriched supernovae (SNe) ejecta, creating a reservoir of gas to fuel multiple bursts of star formation and giving rise to multi-iron and multi-age stellar subpopulations, at odds with commonly observed stellar clusters. *Thus, the detection of such complex stellar systems in the bulge, and their comparison with the field population, represent a key observational proof to support the involvement of clumps in building galaxies' bulges: the newly named Bulge Fossil Fragments (BFFs) scenario.*

At present, among the stellar clusters born in-situ in the Milky Way, we can include to the list of potential clumps survivors Terzan 5 and Liller 1. Indeed, these are the only bulge stellar systems that enclose different subpopulations characterized by a remarkable iron ($\Delta\,[\mathrm{Fe/H}] \sim 1\,\mathrm{dex}$) and age ($\Delta t > 3\,\mathrm{Gyr}$) spreads. This research project, summarized

by the following thesis, has been aiming at gathering new accurate observational evidences to reconstruct the origin and the evolutionary history of Liller 1 and Terzan 5. To this purpose, a multifaceted strategy has been essential. The main results, as well as related methodologies, are summarized as follows.

(1) We built deep and accurate photometric catalogs of Liller 1 and Terzan 5 exploiting the combination of high angular resolution optical and near-infrared adaptive optics images. These catalogs led the construction of high-resolution differential extinction maps in their direction. In combination with stars' proper motions computed thanks to the time baseline between the two data sets, we obtained color-magnitude diagrams through which it has been possible, for the first time, to clearly detect the presence of different stellar subpopulations. This task has proven to be challenging, because of the loci occupied by Terzan 5 and Liller 1 within the Galactic bulge, characterized by a high degree of differential extinction and field contamination. These constitute the main observational limitations that have been hampering the complex nature of these stellar systems so far. The measure of the age and metallicity, via isochrone fitting, of their stellar subpopulations revealed the coexistence of old ($\sim 12\,\mathrm{Gyr}$) and subsolar ([M/H] $\sim -0.3\,\mathrm{dex}$) stellar populations with young (up to $1-2\,\mathrm{Gyr}$) and supersolar ([M/H] $\sim +0.3\,\mathrm{dex}$) ones.

(2) We reconstructed the star formation histories (SFHs) of Terzan 5 and Liller 1 by using a synthetic CMD fitting procedure widely adopted for resolved dwarf galaxies. This methodology could benefit from the new photometric analyses of the stellar systems under investigation. The results suggest that Liller 1 and Terzan 5 experienced a prolonged, multi-episode star formation history fueled by iron-enriched gas. We concluded that alternative formation scenarios proposed for these systems, based on the merging between the proto-Liller 1/Terzan 5 and bulge/disk giant molecular clouds, fail in explaining the overall complexity of their SFHs. Indeed, because of the rarity and timescales calculated for these encounters (as computed by ad-hoc numeral simulations), stellar systems forming this alternative way are expected to produce two discrete, well separated and brief star-formation episodes.

(3) We performed a chemical and kinematical analysis of the BFFs candidates by means of the Integral Field Spectrograph facility MUSE at the Very Large Telescope. Over the past 10 years, a large number of high and intermediate resolution spectra were collected for Terzan 5, unraveling its complex and multimodal metallicity distribution. Conversely, the metallicity of Liller 1 remained basically unexplored until this thesis. We built the metallicity distribution functions (MDFs) of Liller 1 and Terzan 5, exploiting a set of low resolution MUSE spectra ($R \sim 3000$). We only measured the [Fe/H] of the stars - but along all the Reg Giant Branch extension - by means of a published calibration relation based on the equivalent width of CaII triplet lines. The high and unbiased statistics unlocked by this instrument provided two main results: first, we detected, for the first time, a bimodal iron distribution for Liller 1, that is compatible with the MDF displayed by bulge field stars, with a subsolar component at [Fe/H] $= -0.48\,\mathrm{dex}$ and a supersolar component at [Fe/H] $= +0.26\,\mathrm{dex}$; second, we measured reliable and unbiased relative fractions of metal-poor and metal-rich stars both in Terzan 5 and Liller 1, which are important ingredients for future chemical evolution and hydrodynamical models. It is

worth of underlying that the supersolar population of Liller 1 appears significantly more centrally concentrated than the subsolar one, as already found in Terzan 5 by previous spectroscopic screenings. This is more likely explainable by invoking a self-enrichment process, which, being peculiar of massive stellar systems, would link these systems to the the primordial giant star-forming clumps. In addition to the chemistry, we retrieved line-of-sight velocities for hundreds of clusters' member stars. In the case if Liller 1, this new kinematics allowed us to infer a systemic velocity remarkably different from the values reported in the literature.

The results presented in this thesis indicate that Terzan 5 and Liller 1, at odds with their appearance, did not undergo the same formation and evolution path of *genuine* globular clusters, and they formed and evolved in deep connection with the Galactic bulge. These evidences make them strong candidate present-day remnants of the massive clumps observed in high-redshift galaxies, opening a new line of investigation: these peculiar stellar systems could represent the first observational proof of the hierarchical assembling process predicted by the clump-origin scenario, shedding new light on the formation of our bulge and galaxies' bulges in a more general cosmological picture.

# Contents

# 1 Overall introduction

## 1.1 General context: the Galactic bulge

The majority of the stellar mass of the Universe is enclosed in spheroids, as indicated by Fukugita et al. (1998). The Galactic bulge, as the central structure of the Milky Way, stands as the sole spheroid where individual stars can be resolved and therefore analyzed in depth. Given its significance, comprehending the formation and evolution of this stellar component represents a pivotal objective in modern astrophysics.

The precise definition of the extent of the Galactic bulge is somewhat arbitrary. Typically, it is delineated as the region on the sky covering $\pm 10°$ both in Galactic longitude and latitude, with the central kiloparsec often referred to as the inner bulge. This region contributes at least to 20% of the total stellar mass of the Milky Way (Zoccali & Valenti 2016) and 25% to its bolometric luminosity. Due to the substantial and spatially variable extinction obscuring this area (e.g., Gonzalez et al. 2012), investigating the bulge has proven to be remarkably challenging, particularly at optical wavelengths.

Specific fields exhibit low extinction, such as Baade's Window $(l, b = 0.9°, -3.9°)$, the Plaut's Field $(l, b = 0°, -8°)$, and the Sagittarius I Field $(l, b = 1.3°, -2.65°)$. Consequently, these fields have historically been the focal points of initial photometric and spectroscopic studies on bulge stars. More recently, the introduction of near-infrared (NIR) facilities has facilitated the exploration of bulge properties even in regions heavily affected by reddening, revealing the composite nature of its stellar populations.

Current large spectroscopic and photometric surveys are providing a comprehensive view of the Milky Way bulge stellar population properties with unprecedented accuracy. As a consequence, this enables us to investigate the connection between all the properties of its stellar population (chemistry, kinematics, distribution of stellar density, age) which is essential for refining models related to the formation of the Galactic bulge and, therefore, of galaxies in a more general cosmological framework.

### 1.1.1 Morphology and structure

The most recent view on the 3D structure of the Galactic bulge establishes that it belongs to the class of the so-called boxy/peanut (B/P) bulges, which are typical for barred galaxies.

Since the first NIR maps obtained through the satellite COBE (Dwek et al. 1995), it was evident that an inner bar embodies the main component of the bulge, extending to

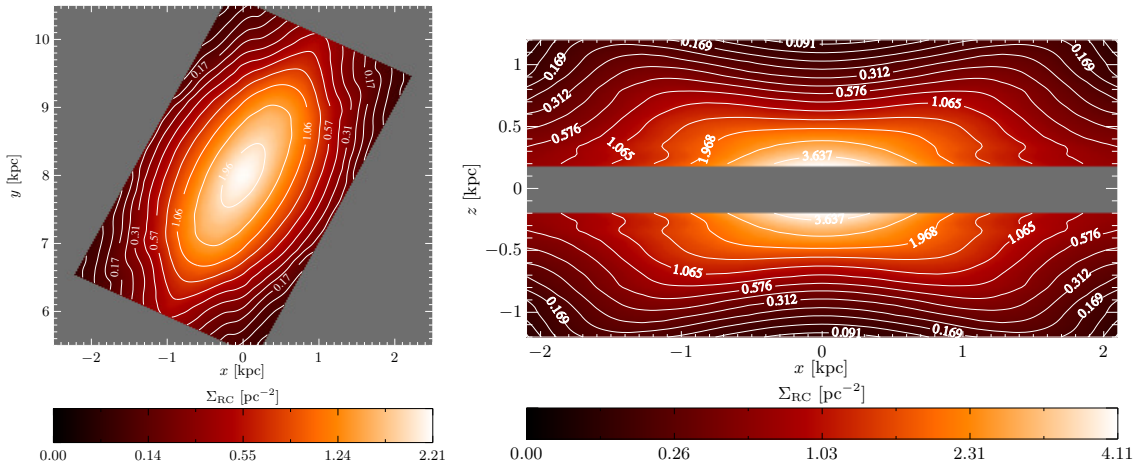


**Figure 1.1:** The Milky Way bulge three-dimensional density projected from the north Galactic pole and along the intermediate axis. Numbers give the surface density of RC stars in pc$^{-2}$, contours define isophotes separated by 1/3 mag. The extinction within 150 pc of the galactic plane is too high for reliable density measurements, and is therefore excluded from the projection (from Wegg & Gerhard 2013).

$\sim 2$ kpc from the center. This was robustly demonstrated by a series of studies based on star counts of standard candles, such as red clump (RC) stars (e.g., Stanek et al. 1997; Babusiaux & Gilmore 2005; Rattenbury et al. 2007). A benchmark work is the one by Wegg & Gerhard (2013), performed through the star catalog of the first data release of the VISTA Variables in the Vía Láctea (VVV) Survey (Minniti et al. 2010). The authors could build deprojected 3D density map of stars across the inner $\pm 2.2 \times \pm 1.4 \times \pm 1.1$ kpc, finding a strongly barred density (see left panel of Figure 1.1) with bar angle $\phi_{\rm bar} = 27° \pm 2°$ with respect to the Sun–Galactic center line, axis ratios (10 : 6.3 : 2.6), and exponential scalelengths (0.70 : 0.44: 0.18) kpc. The same VVV data set allowed to build the first proper density map of the external region, highlighting the X-shaped morphology that characterizes the outer bulge (see the right panel of Figure 1.1). The X/peanut shape of the bulge was already suggested by previous photometric studies that detected the presence of a double RC in the color-magnitude diagram (CMD) of some external fields (McWilliam & Zoccali 2010a; Nataf et al. 2010; Saito et al. 2011). Later, Wegg et al. (2015) showed - using a set of RC stars from the photometric surveys 2MASS (Two Micron All Sky Survey), UKIDSS (UK Infrared Deep Sky Survey), and VVV - that the B/P bulge continuously transits outward into a planar bar with semimajor axis of $5.0 \pm 0.2$ kpc and bar angle $\phi_{\rm bar} = 28° - 33°$.

A proper modelling of the point spread function of the sources detected in the VVV catalog, and the derived RC stellar density profile (which globally covered the area within $|l| \leq 10°$ and $|b| \leq 4.5°$), unveiled the presence of an inner, compact and axisymmetric spheroid in the central $\sim 150$ pc (Valenti et al. 2016). The same work provided the first purely empirical estimate of the stellar mass of the Milky Way bulge, obtaining $2.0 \pm 0.3 \times 10^{10}\, M_{\odot}$, which is in agreement with the value provided by state-of-the-art dynamical models ($1.8 \times 10^{10}\, M_{\odot}$; Portail et al. 2017).

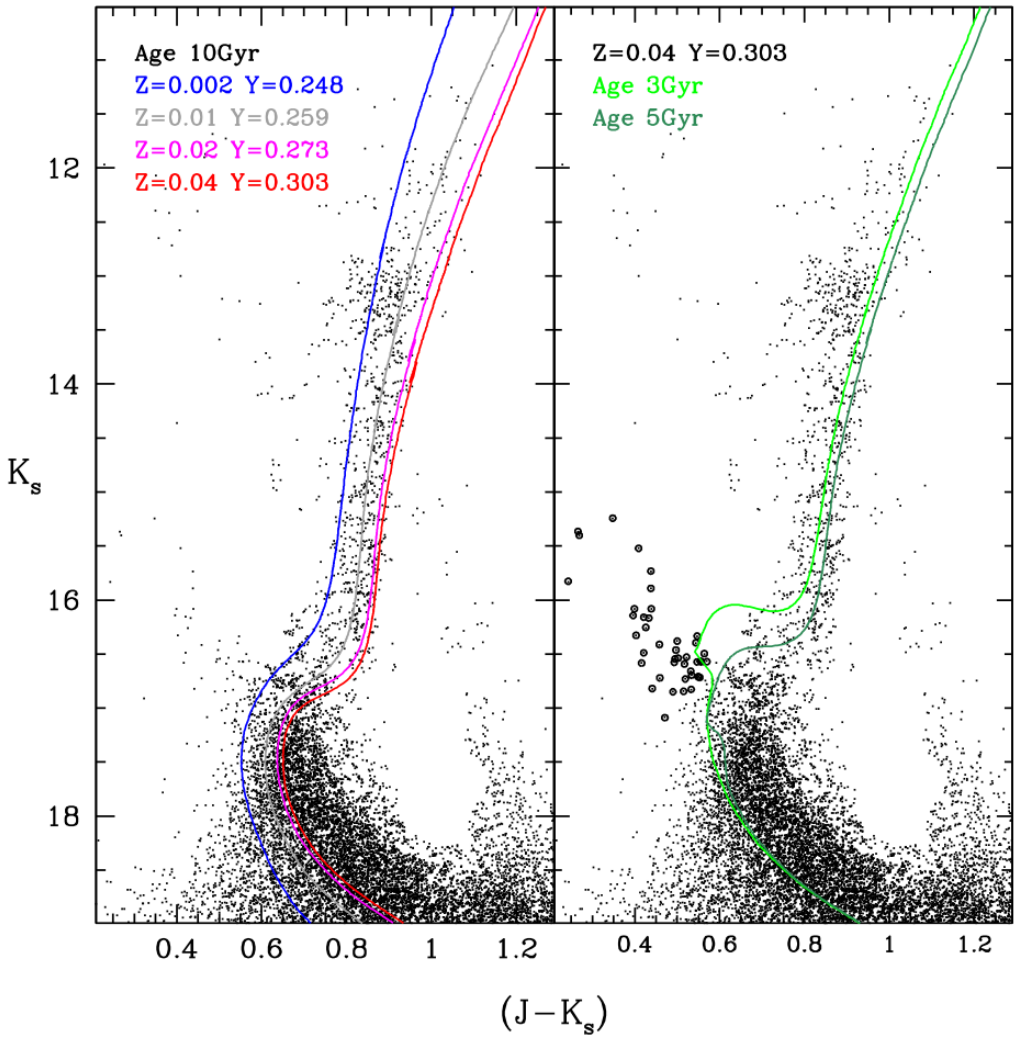


**Figure 1.2:** CMD of one of the bulge fields ($l, b = -6.8°, -4.7°$) analyzed in Valenti et al. (2013) with overplotted theoretical isochrones (Valcarce et al. 2012). Isochrone ages, metallicities, and helium abundances are indicated near the top-left corner of each panel. Subsolar isochrones are $\alpha$-enhanced, and solarscaled otherwise. The metallicity range shown in the left panel is chosen to match the observed metallicity spread for that specific bulge window. Open circles mark stars that are most likely blue stragglers.

### 1.1.2 Age

Given that it is possible to study the stellar population of the Galactic bulge by means of techniques widely adopted for resolved stellar populations, the absolute age of its stellar content has been mainly determined by CMD fitting methods. The (disk-decontaminated) CMD of the least extincted bulge fields (Ortolani et al. 1993; Zoccali et al. 2003; Clarkson et al. 2008; Valenti et al. 2013; Renzini et al. 2018) can be perfectly reproduced by an old stellar population, with an age older than 10 Gyr, as shown by the exemplifying left panel of Figure 1.2. The right panel of the same figure demonstrates that the fraction of

young stars ($t \leq 5$ Gyr) in the bulge must be small, and blue straggler stars[1], that mimic a young stellar population, can pollute the CMD (see the open circles). Indeed, the old age estimate is further reinforced by studies that expressly included the population of blue straggler stars observed in the bulge (Clarkson et al. 2011; Surot et al. 2019), confirming a low percentage of possible genuine young stars ($\sim 3\%$) orbiting within it.

On the other hand, age-dating studies based on spectra of microlensed dwarfs estimate a larger fraction of intermediate-young stars, with ages spanning from 1 to 5 Gyr. The analyses of Bensby et al. (2013, 2017) conclude that $\sim 60\%$ of bulge stars is younger than 7 Gyr, of which $\sim 25\%$ is younger than 5 Gyr. Nevertheless, the recent study by Joyce et al. (2023), who reanalyzed the same sample of dwarfs employing an updated set of isochrones and uncertainty modelling, suggests an age distribution strongly weighted toward older stars ($\geq 8$ Gyr), with the mean age of the population around 11 Gyr. They do not find stars with ages $\leq 3$ Gyr and, overall, the fraction of stars younger than 7 Gyr decreases to 16%. However, even if the latter result seems to be more in agreement with the results based on photometry, the age determination of the bulge stellar population is still a controversial and unsolved issue. Indeed, the spectral analyses based on chemical clocks (such as [C/N]; Schultheis et al. 2017; Hasselquist et al. 2020) find a non-negligible peak around $2 - 4$ Gyr in the age distribution. At this point, it is important to underline that a correlation exists between young stars and their spatial distribution and metallicity: it is more likely to find young objects at low Galactic latitudes ($|b| \leq 4°$) and characterized by supersolar [Fe/H] values. Hence, a possible way to interpret this age conundrum is to invoke a spatial selection bias: CMDs age-dating methods are based on observations of low extinction bulge windows (e.g., Baades's window), that could be dominated by older stars.

### 1.1.3 Chemodynamics

Over the past decade, the ensemble of bulge spectroscopic surveys - the Bulge Radial Velocity Assay (BRAVA, Rich et al. 2007; Kunder et al. 2012), the Abundances and Radial velocity Galactic Origins Survey (ARGOS, Freeman et al. 2013), the GIRAFFE Inner Bulge Survey (GIBS, Zoccali et al. 2014), the Gaia-ESO Survey (GES, Gilmore et al. 2012), and the Apache Point Observatory Galactic Evolution Experiment (APOGEE, Majewski et al. 2017) - provided both chemical abundances and radial velocities for tens of thousands bulge stars, clearly unveiling a multimodal metallicity distibution function (MDF) and a tight interdependence between metallicity, kinematics and spatial distribution.

Since the first high-resolution abundance analysis of eleven giant stars in the Badee's Window (McWilliam & Rich 1994), the bulge showed a broad MDF in the range of $-1 <$ [Fe/H] $< +1$ dex and a conspicuous [$\alpha$/Fe] enhancement. One of the most recent overviews of the bulge's chemical pattern is given by Queiroz et al. (2021), who analyzed a large sample of stars coming from one of the latest data release of APOGEE. Figure 1.3 shows the trend of [$\alpha$/Fe] with [Fe/H], demonstrating that the chemical pattern of bulge stars is characterized by a bimodal distribution both in iron and $\alpha$-elements: the first peak is composed of subsolar stars with enhanced [$\alpha$/Fe] ratio, the second peak is made of

[1]Blue straggler stars are anomalously massive core hydrogen-burning stars form via evolution of binaries and/or stellar collisions. These rejuvenating processes let the stars appear bluer, thus younger.

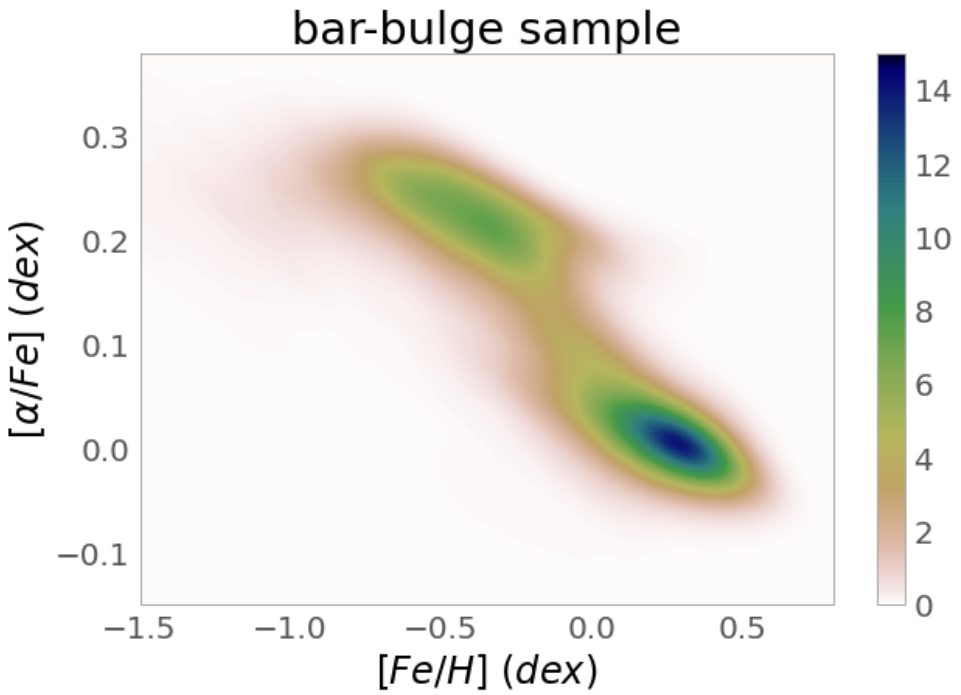


**Figure 1.3:** [$\alpha$/Fe] vs [Fe/H] distribution for the bulge region built with $\sim 26,000$ stars from the APOGEE survey, color-coded according to the probability density function (from Queiroz et al. 2021).

supersolar stars and solar-scaled [$\alpha$/Fe].

The global bimodality of the bulge MDF, as well as its dependence on the Galactic coordinates, was demonstrated by a plethora of studies based on the surveys listed above (e.g., Ness et al. 2013; Rojas-Arriagada et al. 2014, 2017, 2020; Zoccali et al. 2017; Queiroz et al. 2020). As shown in the left panel of Figure 1.4, the relative fraction of metal-poor ([Fe/H] $\sim -0.4$ dex) and metal-rich ([Fe/H] $\sim +0.3$ dex) stars changes across the bulge area. Specifically, metal-rich stars dominate close to the plane. Eventually, the big NIR survey APOGEE seems to confirm what previously found by Ness et al. (2013), revealing up to three metallicity components in the bulge, as displayed in the right panel of Figure 1.4. The density distributions of the two main populations, showed in Figure 1.5, also reveal a different spatial allocation: the metal-poor component (left hand panel) is strongly axysimmetric and centrally concentrated, while the metal-rich one (right hand panel) is clearly boxy. As computed in Zoccali et al. (2018), the metal-poor stars constitute $\sim 48\%$ of the total stellar mass of the bulge, being comparable to the metal-rich sample.

All the spectroscopic surveys agree in showing a global cylindrical rotation and increase of the velocity dispersion towards the central region of the bulge, associated to a higher mass density in the inner degrees (Kunder et al. 2012; Ness et al. 2013, 2016; Zoccali et al. 2014; Valenti et al. 2018; Rojas-Arriagada et al. 2020). The mean global maps of radial velocity and radial velocity dispersion, interpolated over the fields observed by the GIBS survey, are shown in Figure 1.6.

However, as in the case of the spatial distribution, the different bulge metallicity

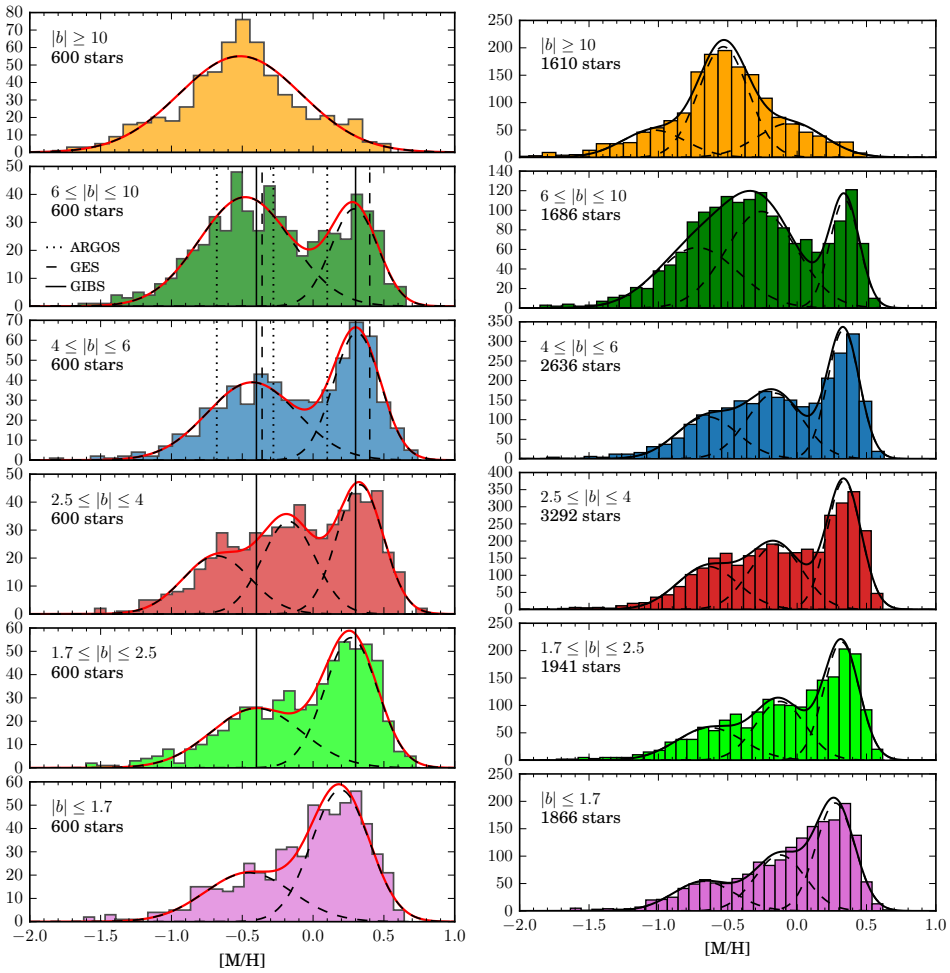


**Figure 1.4:** Figures 17 and 9 from Rojas-Arriagada et al. (2020). *Left panel:* APOGEE MDFs for six different Galactic latitude bins. The MDFs were resampled and convolved with uncertainties to match previous surveys. Solid, dashed and dotted vertical lines mark, respectively, the metallicity peaks found in the GIBS, GES and ARGOS MDFs. They are only displayed in the panels corresponding to the latitude ranges covered by the respective survey. The dashed and solid curved lines represent the individual and summed components, respectively, of the optimal GMM modelling of the data's density distribution *Right panel:* MDFs of the same latidude strips as in the left panel, but considering all the bona-fide stars from the APOGEE catalog. The specific number of objects, as well as the latitude range, for each panel are indicated in the upper-left corner. As in the left panel, solid and dashed curved lines are the global and individual functions that best reproduce the observed distributions.

components display different kinematics. A clear dichotomy in the vertex deviation[2] suggested that stars with [Fe/H] $\geq -0.5$ dex move on bar-like orbits, while the metal-poor population shows kinematics corresponding to an old spheroid or a thick disc (e.g., Babusiaux et al. 2010). Later, the progressive build-up of chemokinematics catalogs from different surveys converged towards an overall hotter kinematics for the more metal-poor stars, that means slower rotation and high, approximately constant with latitude, velocity dispersion profile.

[2]The vertex deviation quantifies the misalignment between tangential and radial motions. A stationary, axisymmetric disk will have no vertex deviation, whereas a triaxial bar necessarily introduces a vertex deviation.

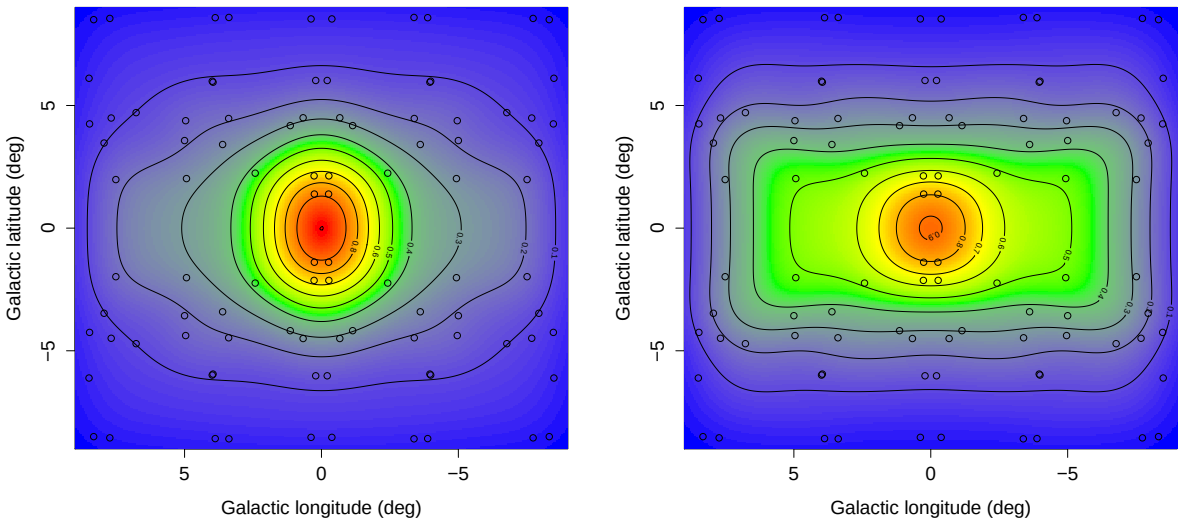


**Figure 1.5:** Density map of metal-poor (left) and metal-rich (right) RC stars obtained using the two component MDF in each field and the total number of RC stars from Valenti et al. (2016). Open circles show the grid of GIBS fields used in the interpolation. The number of RC stars of each component was normalized by the maximum number of RC stars in the metal poor map so they are color-coded to the same scale between values of 0 and 1. Contours are overplotted in both maps and correspond to differences of 0.1 in the normalized RC star counts (from Zoccali et al. 2017).

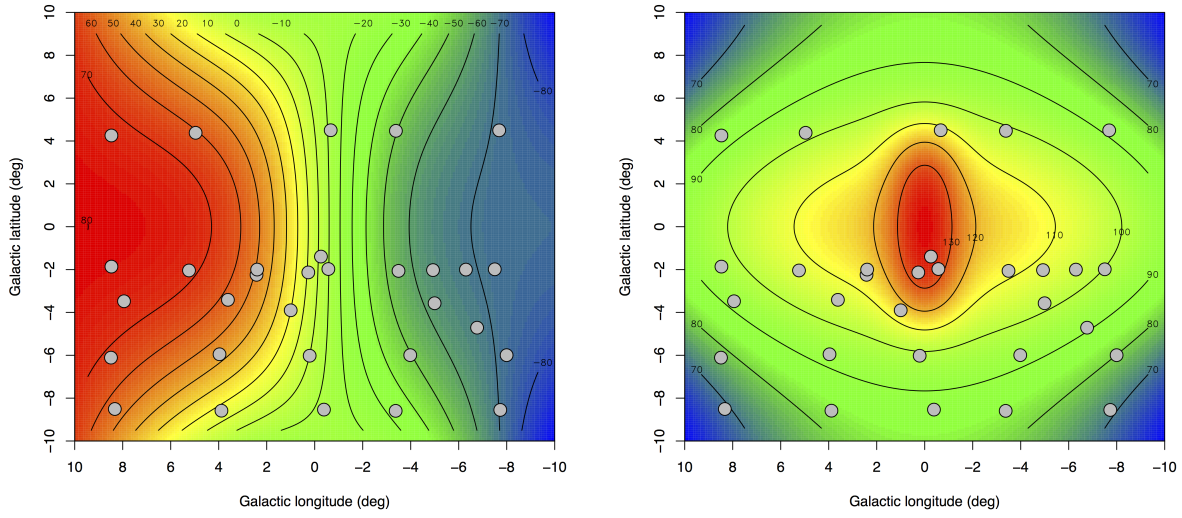


**Figure 1.6:** Mean radial velocity (left) and radial velocity dispersion (right) surface in the longitude-latitude plane constructed from the rotation profiles measured by Zoccali et al. (2014). Gray points show the positions of the observed GIBS fields, while the black contour lines are labeled with the relevant velocity and velocity dispersion in $\mathrm{km\,s^{-1}}$.

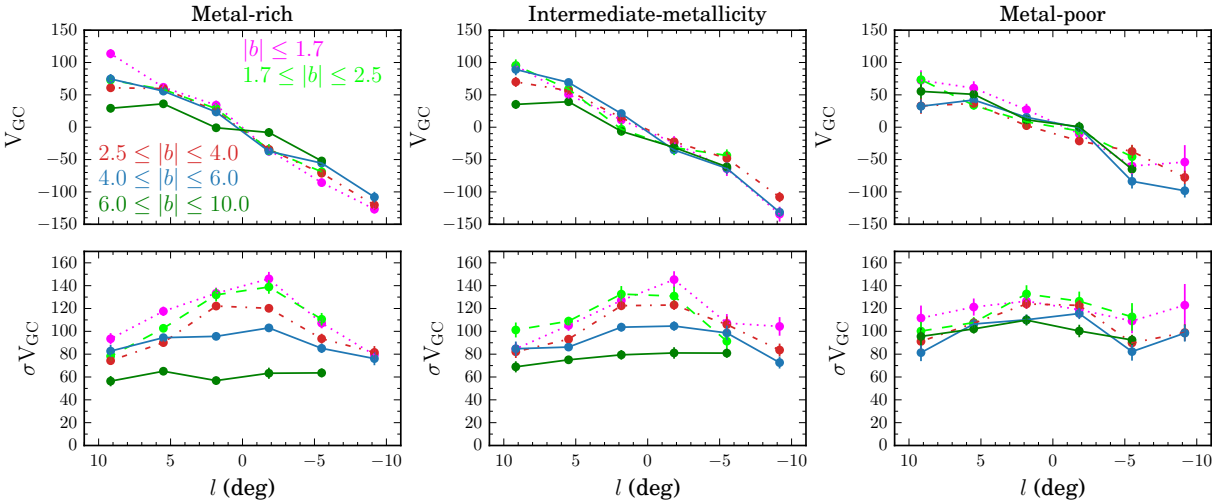


**Figure 1.7:** Mean Galactocentric velocity and velocity dispersion curves for stars in the three GMM-inferred metallicity components shown in the right panel of Figure 1.4. The color of the lines indicates different latitude range, labelled in the upper-left panel (from Rojas-Arriagada et al. 2020).

As an example, we show the results based on APOGEE stars from Rojas-Arriagada et al. (2020) (but see all the references therein). Stars were divided into three metallicity components, following the Gaussian Mixture Modelling (GMM) also shown in the right panel of Figure 1.4. Once more, the enhanced rotation pattern of the metal-rich population towards the midplane, as well as the vertical gradient of its velocity dispersion, suggest that these stars are dominated by a bar dynamics. This fact was clearly confirmed by the comprehensive chemodynamical analysis of Queiroz et al. (2021).

A third, additional component might be represented by RR Lyrae (RRL) stars. RRLs are pulsating, low-metallicity, core-helium-burning horizontal branch giants and trace an old, metal-poor population in the Bulge. Leveraging light-curve data, one can accurately determine luminosities and distances, rendering RRLs valuable markers for the oldest bulge. These RRLs exhibit metallicities [Fe/H] $= -1.0 \pm 0.2$ dex with extended [Fe/H] tails and possess a steep density profile of $\sim r^{-3}$ (Pietrukowicz et al. 2015). Notably, they do not contribute to the B/P bulge, consistent with the first ARGOS finding that only stars with [Fe/H] $> -0.5$ dex participate in the split RC (Ness et al. 2012). Recent spectroscopic analyses indicate that RRLs are kinematically different from bulge red giant branch and RCs stars (e.g., Kunder et al. 2012, 2016), with significant lower rotation and higher velocity dispersion. These characteristics imply that bulge RRLs delineate a distinct component from RCs stars. Considering the number ratio of RRLs to RCs stars, this ancient population is estimated to contribute around 1% of the bulge's stellar mass (Kunder et al. 2016).

## 1.2 Picture of the formation of the Galactic bulge

The complex nature of the Galactic bulge, disclosed by more than twenty years of investigation, points towards a multi-phase formation scenario. Nowadays, two main channels are considered while picturing its assembly: a secular, dynamical evolution of the disk coupled with a first, quick and intense star bursting phase. However, the scientific community has not converged to a general consensus on the mechanisms responsible for its formation, and a satisfactory self-consistent, fully cosmological chemodynamical evolutionary model is still missing.

### 1.2.1 The secular evolution model

The Milky Way's morphology is analogous to external barred galaxies that often contain a B/P bulge embedded in a longer, thinner bar (e.g., Erwin et al. 2023 and references therein). The outer, X-shaped extension of the bulge is a natural product of bar evolution, because dynamical instabilities produce bending and buckling of the elongated stellar orbits within the bars, resulting in the shape of a peanut (Patsis et al. 2002; Athanassoula 2005). Therefore, N-body models for bar-unstable disk evolution regularly find that B/P bulges are the inner 3D parts of a longer bar, and form through a combination of buckling instability and orbits in vertical resonance (Combes et al. 1990; Raha et al. 1991; Athanassoula 2005). In this regard, the overall cylindrical rotation pattern of bulge stars is consistent with a purely dynamical evolution of a disk buckling into a bar (Shen et al. 2010).

The tendency of metal-rich stars to trace the bar, both in the kinematics and morphology space, was predicted in theoretical studies of disks with multiple stellar populations, in which a process called "kinematic fractionation" occurs (Debattista et al. 2017; Fragkoudi et al. 2017). N-body and hydrodynamical simulations of Milky Way-like galaxies, both in isolation and not, show that the formation of bars can efficiently separate disk stellar populations that differ by their initial in-plane kinematics: hot (likely older) disk populations are lifted to large heights ending as a spheroidal population, becoming vertically thick and box-shaped, while the cooler (likely younger) disk populations reorganize themselves into stronger bars, are thinner at the centre and thus produce a peanut shape.

### 1.2.2 The first rapid and intense phase of star formation

However, the exquisite chemical measurements gathered so far unveiled a series of [$\alpha$/Fe] versus [Fe/H] patterns that are uniquely explainable by chemical evolution models that imply formation timescales shorter than 1 Gyr and an intense, in-situ star formation (e.g., Rojas-Arriagada et al. 2017; Matteucci 2021).

Specifically, as shown in Figure 1.3, $\alpha$-enhanced bulge stars are also remarkably metal-rich. This is a symptom of a fast bulge formation with an intense star formation rate (SFR) and a somewhat flat initial mass function (IMF). Indeed, the knee in such a plot, due to the ignition of type Ia supernovae (SNe) in producing mostly iron, should occur at a higher metallicity than for stars in systems with low SFR, such as irregular and dwarf spheroidal

galaxies (e.g., Tolstoy et al. 2009; Matteucci 2012). In fact, a high SFR enriches rapidly the ISM in iron by means of CC-SNe, so that when the SNe Ia start occurring (delayed with respect to CC-SNe) the iron abundance in the ISM is already high. Interestingly, even if the [$\alpha$/Fe] vs [Fe/H] trend showed in Figure 1.3 globally overlaps the one drawn by the stars belonging to the Galactic thick disk (hence, suggesting an underlying relation with it), the knee measured in the case of bulge stars is slightly more metal-rich (Rojas-Arriagada et al. 2017; Zasowski et al. 2019; Queiroz et al. 2021), suggesting that the bulge experienced a faster formation, or rather a higher SFR, than the solar vicinity. Overall, if we account also for the global old ages of the bulge stellar population, all models safely state an intense burst of star formation that took place at early epochs.

On the other hand, the chemical features of the supersolar metallicity peak perfectly match the pattern measured for Galactic thin disk stars, indicating a subsequent accretion of gas and, therefore, possibly justifying the presence of young stars in the bulge. In fact, it has been observed that bars let gas trapping and funnelling towards the inner regions, triggering new bursts of star formation (Ellison et al. 2011). In this respect, the dearth of stars in between the two overdensities shown in Figure 1.4 is evocative of two main star formation paths, with a quenching of the star formation in between (first theorized by the chemical evolution model of Chiappini et al. 1997).

Finally, an essential piece of information comes from high redshift studies. Enhanced central star formation, or even fully formed spheroids, have been observed in galaxies at $z \sim 2$, due to massive amounts of highly dissipative gas accretion (e.g., Tacchella et al. 2015). This assembly process is precedent to the bar formation, which is estimated to happen at $z \sim 1$ (Fragkoudi et al. 2020). Among the most promising way to power this first vigorous star forming phase of the bulge, there is the merging of clumps formed by disc instabilities. It has been theoretically shown that turbulent gas-rich disks can fragment into massive clumps ($\geq 10^8\, M_\odot$, computing the local Jeans mass considering the turbulence observed in high-z disks; Bournaud et al. 2007). If the clumps are massive and long-lived enough (mainly determined by different feedback prescriptions), they interact gravitationally, causing a redistribution of angular momentum outward and an accretion of clumps and other disk mass (e.g., gas) inward. Numerical simulations demonstrate that this process forms a bulge and exponential disk within $\sim 1$ Gyr for a galaxy such as the Milky Way (Noguchi 1999; Immeli et al. 2004a,c; Bournaud et al. 2007; Carollo et al. 2007; Elmegreen et al. 2008; Dekel et al. 2009). Clumps developed by hydrodynamical simulations are also characterized by high SFR densities (Clarke et al. 2019), and they provides a natural way of producing the chemical trend observed in the bulge (Debattista et al. 2023).

As a matter of fact, the clumpy morphology is a common feature of star-forming galaxies at cosmic-noon (for example, Elmegreen et al. 2009; Guo et al. 2015; Shibuya et al. 2016). The observed clumps substantially contribute to the rest-frame UV light of their host galaxies (up to $\sim 40\%$), denoting very high SFRs (e.g., Zanella et al. 2015; Messa et al. 2022); however, a fraction of redder substructures is also detected (Guo et al. 2015). At present, the only way to bypass resolution effects and limitations of current facilities is to measure the physical properties of high-z clumps in gravitationally lensed fields

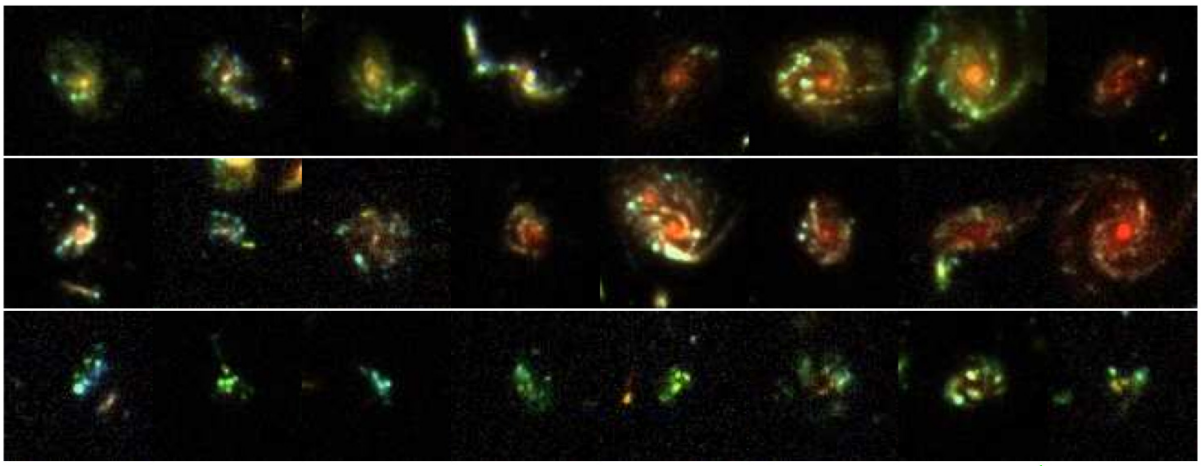

**Figure 1.8:** Collection of RGB images (F435W, F606W, and F850LP filters) of clumpy galaxies within the redshift range $0.5 \leq z \leq 3$ from the HST survey CANDELS/GOODS (from Guo et al. 2015).

(Dessauges-Zavadsky et al. 2017; Messa et al. 2022; Vanzella et al. 2022a,b; Claeyssens et al. 2023). The collection of lensed star-forming clumps estimates stellar masses ranging between $10^5$ and $10^9\,M_\odot$, and sizes from a few to hundred parsecs.

### 1.2.3 The first bulge fossil fragment candidate Terzan 5

The detection, in the Galactic bulge, of present-day remnants of a few high-z clumps would constitute a direct proof that the merging of massive structures could have also contributed to the assembly of galaxies' bulges. It is worth stressing that finding observational evidences of which exact mechanisms set up the bulge is still urgent: this is indeed crucial to our comprehension of the formation process of Milky Way-like galaxies in a cosmological context (i.e., to guide the formation of these galaxies implemented in current cosmological simulations; to have constraints on the gas fraction, turbulence and kinematics of high-redshift disk galaxies; to understand feedback processes prescriptions; etc.).

Several studies regarding observed gradients of high-z clump masses (e.g., Guo et al. 2018; Ambachew et al. 2022) suggest that a fraction of giant clumps may actually survive feedback processes and dynamical conditions of the host galaxies, migrating towards the center. In addition, theoretical works demonstrate that not only the massive clumps are able to migrate to the center, but some of them are also able to survive the total disruption and to generate stellar clusters (Bournaud 2016; Dekel et al. 2023).

These *fossil fragments* of the bulge formation process should be characterized by well-defined main features. First, they should be observable under the false identity of massive globular clusters (GCs), whose reconstructed orbit undoubtedly confirms that these systems where born in the internal region of our Galaxy. Second, considering that these giant clumps would have formed stars rapidly and with very high SFR (similarly to the bulge), the stellar population of the fossil fragments should be composed of old stars characterized by the same chemistry (in terms of both $\alpha$-elements and iron) as that observed in the Galactic bulge. Third, they should host multiple populations of stars

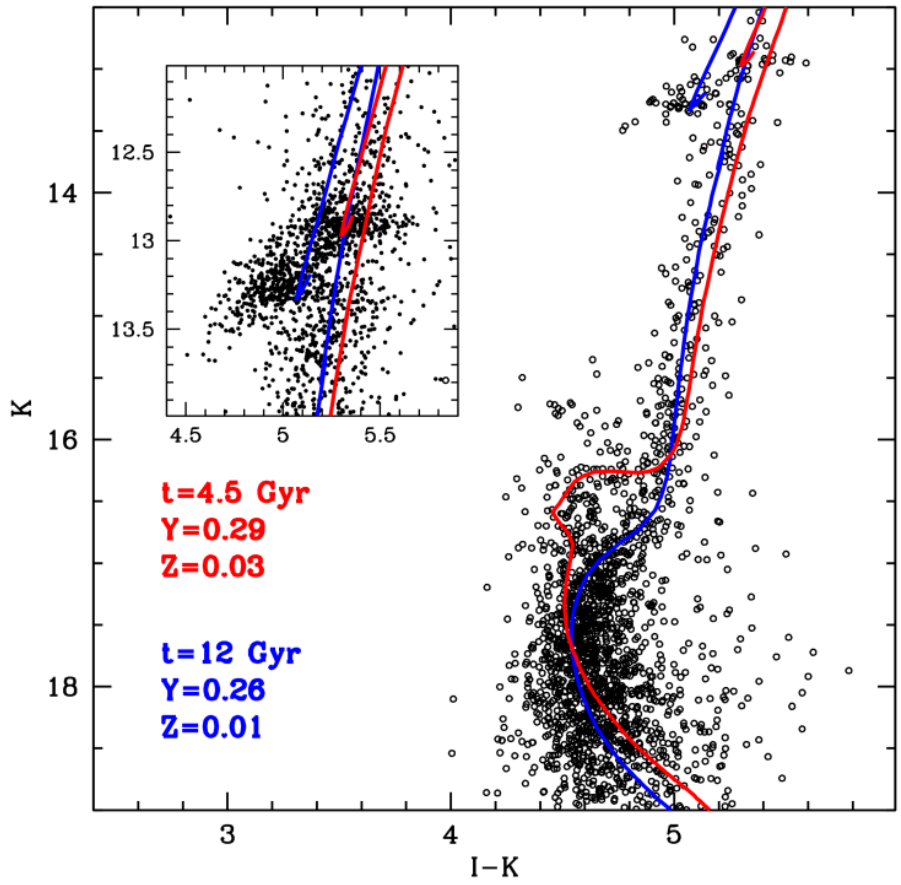


**Figure 1.9:** Differential reddening corrected CMD of Terzan 5 made with a subsample of well-measured stars. Two isochrones (Girardi et al. 2002) are overplotted: the blue line represents the main old (see ree label) and subsolar ([Fe/H] $= -0.3$ dex) population of Terzan 5; the red line corresponds to a younger (see blue label) isochrone with supersolar chemical composition ([Fe/H] $= +0.3$ dex). In order to better appreciate the agreement between the isochrones and the data at the red clump level, the inset shows a zoomed CMD, with all the measured stars (i.e., with no selections) plotted (from Ferraro et al. 2016).

with different iron abundances and different ages. Indeed, it is likely that the primordial clumps were massive enough to retain iron-enriched SNe ejecta, creating a reservoir of gas to fuel multiple bursts of star formation and giving rise to multi-iron and multi-age stellar subpopulations, following a self-enrichment process.

These are the striking characteristics identified in the stellar cluster Terzan 5, which was considered as a genuine bulge GC until a few years ago. Terzan 5 is a massive stellar cluster (with a total mass of $2 \times 10^6$ $M_\odot$; Lanzoni et al. 2010) dynamically classified as an in-situ (more precisely, a Bulge) system (Massari et al. 2019; Vasiliev & Baumgardt 2021; Callingham et al. 2022). Since it is located in the inner region of the Milky Way[3], the high extinction in its direction (equal to $E(B-V) = 2.38$; Valenti et al. 2007) hampered for a long time the proper study of its stellar content.

[3]The Galactic coordinates are $l = 3.84°, b = 1.69°$, and respective Galactocentric distance $R_{GC} = 1.65$ kpc (Vasiliev & Baumgardt 2021).

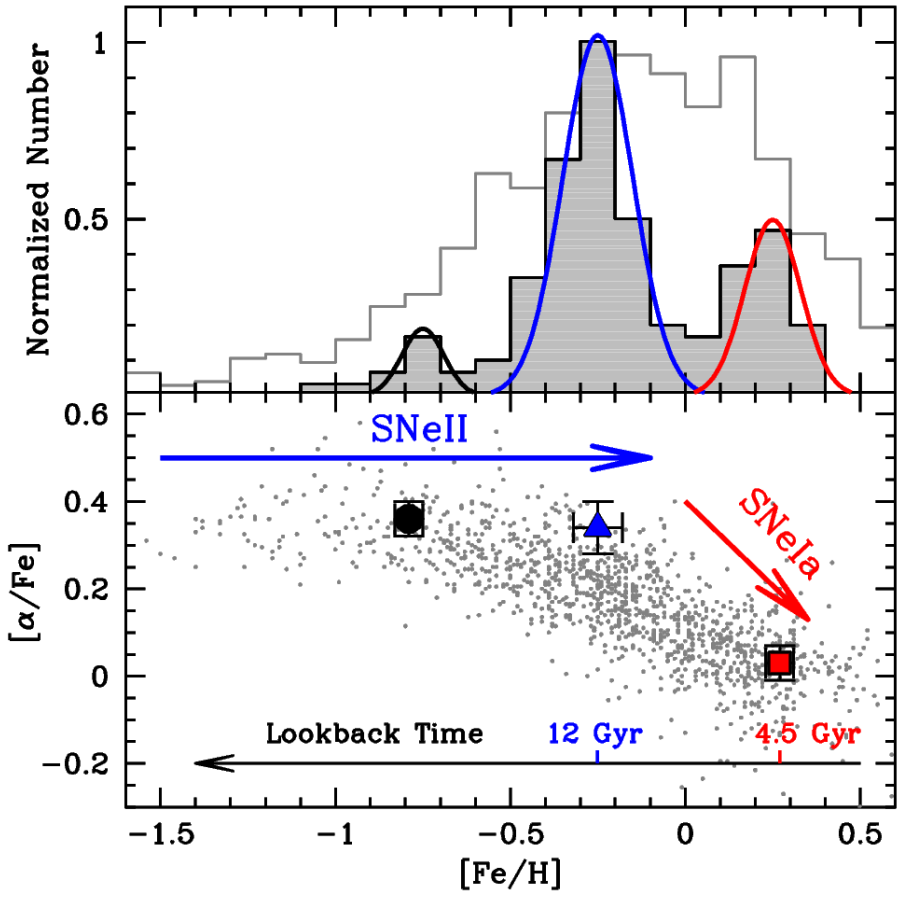


**Figure 1.10:** *Top panel:* iron distribution of the three subpopulations of Terzan 5 (gray histogram and colored lines; Massari et al. 2014) compared to that of the Galactic bulge field stars from the literature (Ness et al. 2013; Johnson et al. 2014). *Bottom panel:* [$\alpha$/Fe]-[Fe/H] distribution of the three subpopulations of Terzan 5 (extreme metal-poor: black circle; subsolar: blue triangle; supersolar: red square) compared to that of the bulge field stars from the literature (gray dots). The formation epoch of the two major Terzan 5 subpopulations is also labeled (from Ferraro et al. 2016).

Thanks to the first high-resolution and near-infrared (IR) photometric observations of Terzan 5 (Ferraro et al. 2009), coupled with high-resolution optical images acquired with the Hubble Space Telescope, it was possible to discovery multi-age and multi-iron stellar populations coexisting in this stellar system. As visible from Figure 1.9, which displays the differential reddening corrected CMD of Terzan 5 (Massari et al. 2012) composed of stars belonging to the cluster (Massari et al. 2015), it is possible to distinguish a double main sequence turnoff (MS-TO) and two well populated RCs. This clearly demonstrates the presence of at least two main populations (Ferraro et al. 2016): a 12 Gyr old population with subsolar metallicity, and a younger stellar population, with an age of $\sim$ 4.5 Gyr and supersolar metallicity.

The metallicities adopted for calculating the stellar models displayed in Figure 1.9 are based on several high-resolution chemical screenings of Terzan 5 (Origlia et al. 2011, 2013; Massari et al. 2014). These studies were based on stars selected from the two different RCs (optimally tracing the different stellar populations, see the inset of Figure 1.9), or samples

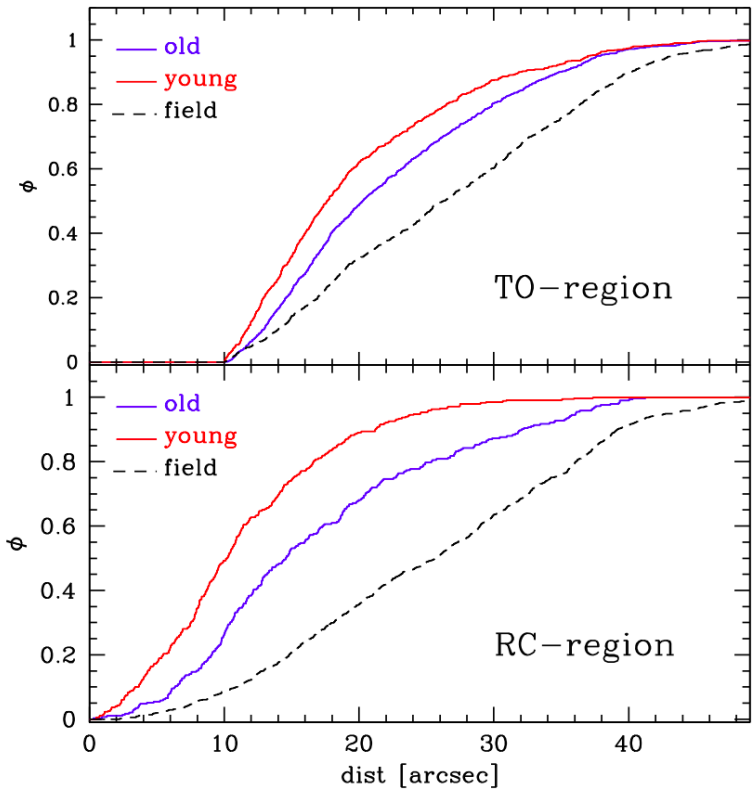


**Figure 1.11:** *Top panel*: cumulative radial distribution of MS-TO/SGB stars belonging to the young population (red line) and to the old population (blue line), compared to that of field stars (black dashed line), as a function of the projected distance from the center of Terzan 5. The field distribution has been obtained from a synthetic sample of 10,000 stars uniformly distributed over the considered observed region. *Bottom panel*: same as in the top panel, but for stars selected from the two RCs. Clearly, the young population is more centrally concentrated than the old one (from Ferraro et al. 2016).

of bright giant stars. These detailed analyses pointed out some important features, that are summarized in Figure 1.10: *i)* the dominant old population ($t = 12$ Gyr) was formed on a short timescale, from gas rapidly enriched by type CC-SNe with subsolar metallicity ([Fe/H]$= -0.3$ dex) and enhanced [$\alpha$/Fe] abundance ratio; *ii)* the younger population ($t = 4.5$ Gyr) formed from gas characterized by supersolar metallicity ([Fe/H]$= +0.3$ dex) and solar-scaled [$\alpha$/Fe]; *iii)* it seems to be present an additional and minor metal poor [Fe/H]$= -0.7$ dex population, which is also enhanced in the [$\alpha$/Fe] abundance ratio. The [$\alpha$/Fe]-[Fe/H] pattern of Terzan 5 is strikingly similar to that of bulge stars (marked by grey points in Figure 1.10, see also Section 1.1.3), and totally incompatible with what observed in the Milky Way outer disk and halo, and in local dwarf galaxies. Indeed, this specific chemical pattern is distinctive of massive and dense environments that experienced star formation at very high SFRs, like the Galactic bulge or high-z clumps.

These evidences state that Terzan 5 is not a genuine GC: it experienced a complex and prolonged star formation and chemical enrichment history, possibly driven by a self-enrichment process. The supersolar stellar population is found more centrally concentrated with respect to the subsolar one (Lanzoni et al. 2010; Ferraro et al. 2016), as demonstrated by their cumulative radial distributions shown in Figure 1.11, further supporting a self-

enrichment scenario. Moreover, the recent study by Romano et al. (2023) demonstrated that it is possible to reproduce the mass, metallicity distribution function, and chemical abundance patterns measured in Terzan 5 by assuming a chemical evolution model driven by self-enrichment. To reproduce the chemical pattern shown in Figure 1.10, the (pure) chemical model has to start from a gas clump with mass of the order of $10^7 M_\odot$, and it has to assume two main star formation episodes separated by a long period ($\sim 7$ Gyr) of quiescence or low-level star formation activity.

Lastly, it is worth mentioning the extraordinary population of millisecond pulsars (MSPs) observed in Terzan 5. This is the Galactic stellar system hosting the highest number of MSPs. This fact can be naturally explained by considering the high SFR supposed to characterize the main old population of Terzan 5. Indeed, a large number of CC-SNe is expected to have produced a large population of neutron stars, mostly retained by the deep potential well of the massive proto-Terzan 5. The large collisional rate of this system (due to its high central mass density; Lanzoni et al. 2010) may also have favored the formation of binary systems containing neutron stars and promoted the recycling process responsible for the production of the large MSP population now observed in Terzan 5.

## 1.3 This thesis: searching for fossil fragments into the Galactic bulge

An important requisite to prove the validity of the *Bulge Fossil Fragments* scenario, suggested by the peculiar features observed in Terzan 5, is the detection other similar complex stellar systems hidden in the Galactic bulge.

We thus focused on another in-situ (Vasiliev & Baumgardt 2021; Callingham et al. 2022) stellar system in the bulge, appearing as a GC, but still largely unexplored: Liller 1. This stellar system is located at only 0.8 kpc from the Galactic centre, very close to the Galactic plane ($l = 354.84°, b = -0.16°$; Harris 1996), in a region that is strongly affected by large foreground extinction (see Section 2.1.4 for details). Indeed, with an average colour excess $E(B-V)$ larger than 3, an extinction as large as 10 magnitudes can be estimated in the optical band toward the cluster. This, combined with significant evidence of differential reddening (Ortolani et al. 2001), has severely hampered the study of Liller 1 so far.

A first insight into its stellar content was recently obtained from a dedicated study based on near-IR GEMINI observations (Saracino et al. 2015). Thanks to these data, it was possible, for the first time, to have an insight into the cluster population down to its MS-TO level. The dataset was used to accurately determine the structural and physical parameters (see Table 1.1) of Liller 1, confirming that this is a massive stellar system (of $1 - 2 \times 10^6\, M_\odot$) with a very large collision rate (the second-highest after Terzan 5), all elements that makes the case of Liller 1 a very interesting one. On the other hand, as shown in Figure 1.12, this data set could not allow an estimate of the age of the system, or the detection of younger stellar populations.

The chemical composition of this system is based only on a handful of spectra. Origlia et al. (2002) estimated a metallicity of [Fe/H]$= -0.3$ dex, and some $\alpha$-enhancement

| Parameter | Value |
|---|---|
| Center of gravity | $\alpha_{J2000} = 17^{\rm h}33^{\rm m}24^{\rm s}.56$ |
| | $\delta_{J2000} = -33°23'22''.4$ |
| Reddening | $E(B-V) = 3.30 \pm 0.20$ |
| Distance modulus | $\mu_0 = 14.55 \pm 0.15$ |
| Core radius | $r_c = 5.39''^{-0.53}_{+0.61}$ |
| Effective radius | $r_e = 22.4''^{-3.3}_{+5.6}$ |
| Half-mass radius | $r_h = 30.5''^{-4.7}_{+7.9}$ |
| Tidal radius | $r_t = 298''^{-63}_{+82}$ |
| Concentration | $c = 1.74''^{-0.15}_{+0.15}$ |
| Total mass | $M_{TOT} = 2.3^{-0.1}_{+0.3} \times 10^6\,{\rm M}_\odot$ (Salpeter IMF; Salpeter 1955) |
| | $M_{TOT} = 1.5^{-0.1}_{+0.2} \times 10^6\,{\rm M}_\odot$ (Kroupa IMF; Kroupa 2001) |
| Central mass density | $\rho_0 \simeq 7.2^{-1.0}_{+1.2} \times 10^6\,{\rm M}_\odot$ (Salpeter IMF) |
| | $\rho_0 \simeq 4.8^{-1.0}_{+1.2} \times 10^6\,{\rm M}_\odot$ (Kroupa IMF) |

**Table 1.1:** Summary of the structural parameters of Liller 1 derived in Saracino et al. (2015).

([$\alpha$/Fe]$\sim +0.3$ dex), based on two IR high-resolution spectra. Horta et al. (2020), finding only four possible member stars in the APOGEE catalog (Majewski et al. 2017), estimated a metallicity of [Fe/H] $= -0.03$ dex. Another estimate comes from Stephens & Frogel 2004, who measured an iron abundance of [Fe/H] $= -0.36$ dex by analysing the equivalent width of some key chemical features (Ca triplet, Na doublet and CO band head) for eight stars. Clearly, the relative poor statistics of these studies prevented the possibility to detect stellar populations with different chemical content.

Therefore, all the analysis presented in this Thesis is aimed at unveiling the nature of Liller 1 through the detailed photometric and spectroscopic characterization of its stellar population. Clearly, a meaningful comprehension of its features is only possible by means of the comparison with the previously detected bulge fossil fragment candidate Terzan 5.

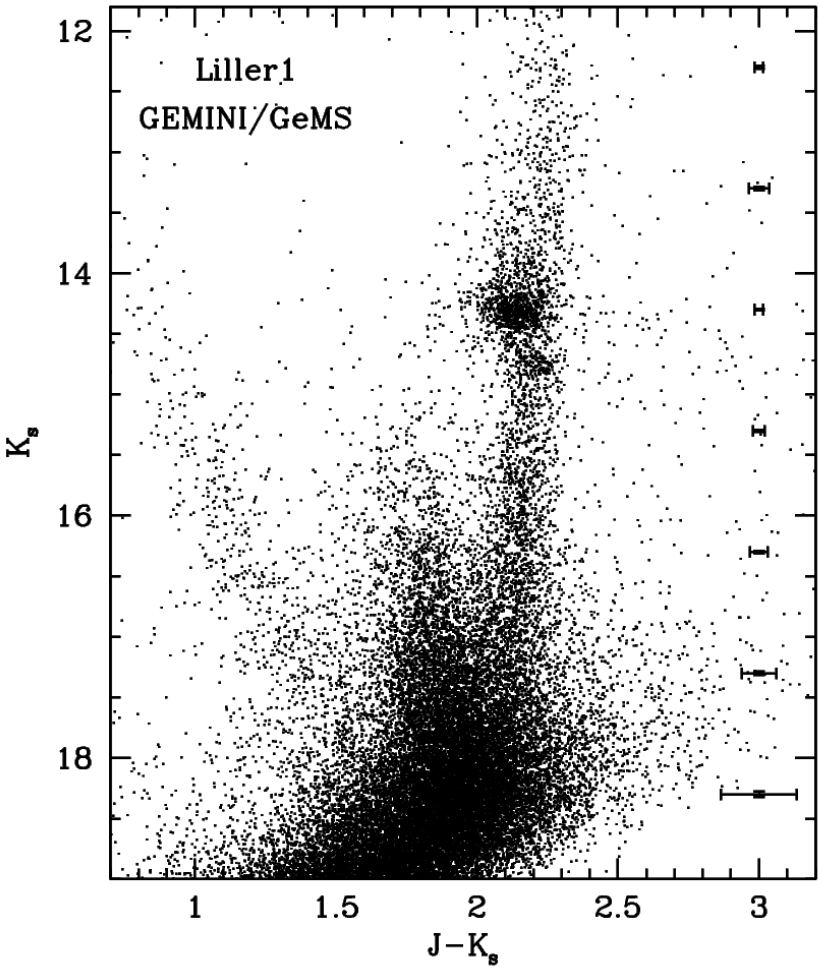


**Figure 1.12:** Near-IR differential reddening corrected CMD of Liller 1 obtained from the GEMINI observations analyzed in Saracino et al. (2015). The photometric errors for each bin of $K_s$ magnitudes are shown on the right side of the panel (from Saracino et al. 2015).

# 2 Photometric analysis of the Bulge Fossil Fragments candidates

## 2.1 Combined optical and infrared imaging unveils the complexity of Liller 1

As already mentioned in the introductory Section 1.3, a sound confirmation of the Bulge Fossil Fragments scenario would come from the discovery of other similar fossil survivors of the Galactic bulge formation process. To this aim, here we present the very first ultra-deep and high angular resolution photometric observations of Liller 1 in the F606W and F814W bands, by using the Hubble Space Telescope (HST). These observations have been combined with the NIR (J and $K_s$) images obtained with GEMINI to select the most suitable CMD for the study of the stellar populations in Liller 1.

### 2.1.1 Observations and data reduction

The photometric dataset used in this reduction combines optical and IR high spatial resolution images. The optical database includes images acquired with the HST Wide Field Channel/Advanced Camera for Survey (ACS/WFC) through the proposal GO 15231 (PI: Ferraro). It consists of 12 deep images obtained with the filters F606W (hereafter $V$) and F814W ($I$). The ACS/WFC is composed of two twin chips, each of $4096 \times 2051$ pixels, separated by a gap of approximately 30 pixels. The pixel scale is $0.05''$ pixel$^{-1}$, therefore the resulting field of view (FOV) is $204'' \times 204''$. The cluster is centered in chip 1, as shown in Figure 2.1. All images are dithered by a few pixels to allow a better subtraction of CCD defects, artifacts and false detections, and eventually a better sampling of the stellar point spread function (PSF).

The IR dataset was obtained with the camera Gemini South Adaptive Optics Imager (GSAOI) assisted by the Gemini Multi-Conjugate Adaptive Optics System (GeMS) mounted at the 8 m Gemini South Telescope (Chile; Program ID: GS-2013-Q-23; PI: D. Geisler). GSAOI is equipped with a $2 \times 2$ mosaic of Rockwell HAWAII-2RG $2048 \times 2048$ pixels arrays with a resolution of 0.02 pixel$^{-1}$ (Neichel et al. 2014). The central region of Liller 1 was sampled with a mosaic of multiple exposures acquired with a dithering pattern of a few arcseconds resulting in a global FOV of $95'' \times 95''$ on the sky (see the blue square in Figure 2.1). Specifically, a total of 7 and 10 exposures were acquired in three nights from April 20 to May 24 2013 in the J and $K_s$ (simply denoted as $K$) bands, respectively. This

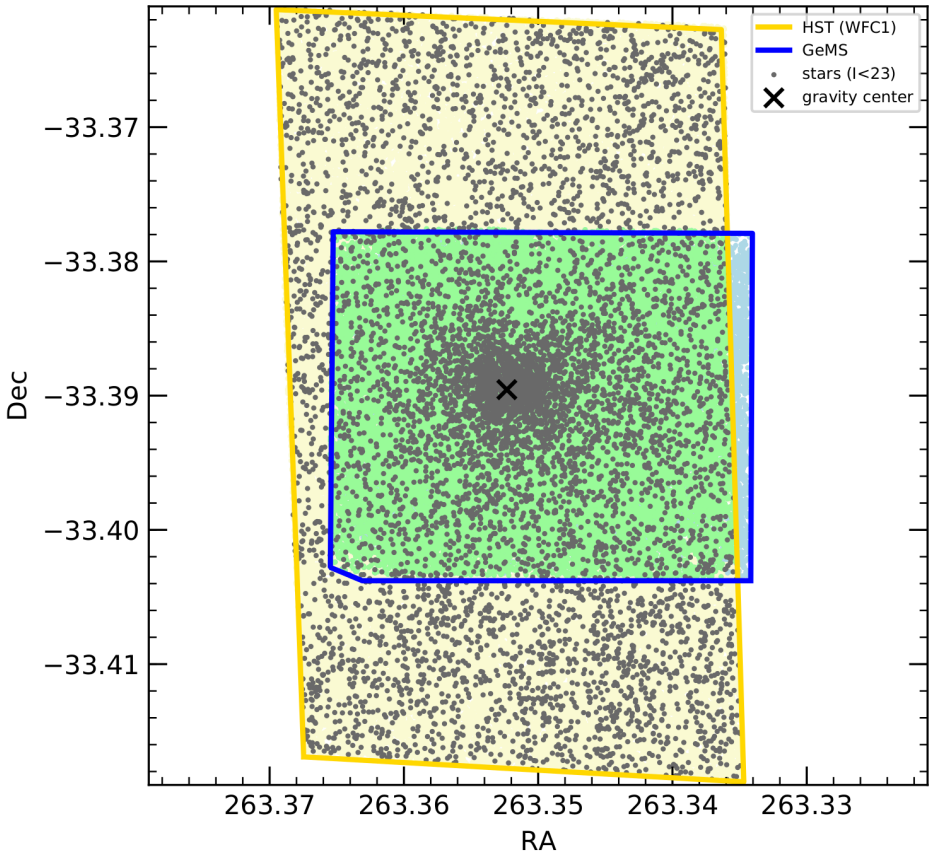


**Figure 2.1:** Field of view sampled by the observations: in yellow all the stars within the rectangular area of $\sim 200'' \times 100''$ covered by chip1 of the ACS/WFC data set, outlined in blue the objects detected within the $\sim 100'' \times 90''$ region corresponding to the GeMS/GSAOI observations, and in green the stars detected in the field of view in common between the two data. For reference, we also show the position of all the detected stars with $I < 23$ (gray dots) and the gravity center (i.e. the photometric barycenter) of Liller 1 (black cross; Saracino et al. 2015).

dataset was analyzed and presented by Saracino et al. (2015) in a first place. Here we re-analyzed only the 6 best-quality images in terms of delivered FWHM, Encircled Energy and Strehl ratio (see Dalessandro et al. 2016) for both the available filters. We summarize the photometric data set used in this analysis in Table 2.1.

The data reduction of the ACS/WFC images has been performed on the CTE-corrected (`flc`) images after a correction for Pixel-Area-Map. The photometric analysis was performed via the PSF fitting method, by using `DAOPHOT` (Stetson 1987) and following the approach used in previous works (e.g., Pallanca et al. 2017; Dalessandro et al. 2018; Cadelano et al. 2019). Spatially variable PSF models were derived for each image by using some dozens of bright and nearly isolated stars. The PSF was modelled adopting an analytical `MOFFAT` function plus a spatially variable look-up table, and it has been applied to all the identified sources with flux peaks at least $3\sigma$ above the local background. We then built a master-list containing all the stellar-like sources detected in more than 3 images in at least one filter. In order to improve the level of completeness, we performed

**Table 2.1:** Summary of the data sets used for Liller 1

| Instrument | Program ID | PI | Date [yyyy/mm/dd] | Filter | $N_{exp} \times t_{exp}$ |
|---|---|---|---|---|---|
| HST/ACS-WFC | GO 15231 | Ferraro | 2019/08/17 | F606W | $2 \times 1361\,s$, $2 \times 1360\,s$, $2 \times 1260\,s$ |
| | | | | F814W | $2 \times 855\,s$, $1 \times 854\,s$, $1 \times 837\,s$, $2 \times 836\,s$ |
| GeMS/GSAOI | GS-2013-Q-23 | Geisler | 2013/04/20 | $K_s$ | $6 \times 30\,s$ |
| | | | | $J$ | $6 \times 30\,s$ |

an accurate inspection of the residual images, in order to search for additional stellar sources missed during the first iteration of the analysis because of the serious crowding conditions. This procedure allowed us to recover a few dozens of stars, which were added to the master-list.

We then forced a fit at the position of each star belonging to the master-list, in each frame, by using the `ALLFRAME` package (Stetson 1994). For each star, multiple magnitude estimates from different exposures were homogenised by using `DAOMATCH` and `DAOMASTER`, and their weighted mean and standard deviation were finally adopted as the star magnitude and photometric error. The final optical HST instrumental catalog contains all the stars measured in at least 3 images in any of the two filters. For each star, it lists the instrumental coordinates, the mean magnitude in each filter and two quality parameters (*chi* and *sharpness*)[4]. The reduction of the ACS/WFC images has been limited to chip 1 because of the negligible overlap between chip 2 and the FOV covered by GeMS. Subsequently, we obtained the catalog containing NIR instrumental magnitudes by using the same reduction strategy applied to the GeMS/GSAOI exposures. In this case, the PSF was modelled adopting a `MOFFAT` function for the $K$ images and a `PENNY` for the $J$ ones.

At this point, the sample of stars detected in the optical and in the NIR catalogs were compared. From a first analysis it was evident that each catalog contained some objects missed in the other, mainly due to the faintness of the source and/or its vicinity to very bright objects with extreme (blue or red) colors. On the other hand, the analysis also demonstrated that, because of the large extinction in the direction of the system, the $V$-band exposures are significantly shallower that those secured through the $I$ filter, and, similarly, the $J$ images are much less deep than those obtained through the $K$ filter. This clearly indicated that the optimal solution for the accurate study of the stellar populations in Liller 1, including optical and NIR filters, consisted in combining the $I$ and the $K$ images. We thus proceeded with a second-level analysis starting from the independent reduction of the optical data set and the 6 best-quality (per each filter) NIR images. Two lists of sources have been obtained: one comprising all the stars detected in the $I$ filter and one including the objects identified in the $K$ band. The $I$-band list contained all the stars measured in at least 3 frames, over the 6 available. The $K$-band list contained all the stars measured in at least 3 over the 6 images analyzed. We thus combined the two data sets,

[4]The *chi* parameter is the ratio between the observed and the expected pixel-to-pixel scatter between the model and the profile image. The *sharpness* parameter quantifies how much the source is spatially different from the PSF model. In particular, positive values are typical of more extended sources, such as galaxies and blends, while negative values are expected in the case of cosmic rays and bad pixels.

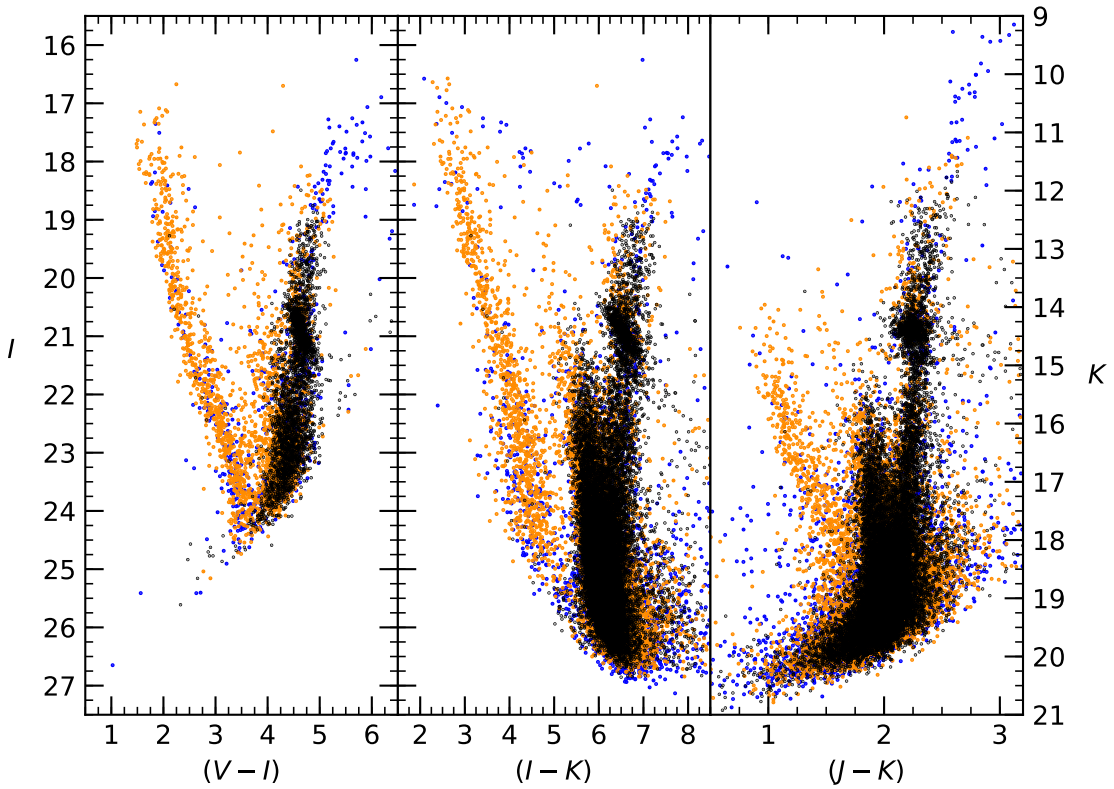


**Figure 2.2:** CMDs of Liller 1 obtained from the combination of optical HST data and GeMS NIR observations in the common field of view (the green area in Figure 2.1): from left to right, the purely optical $(I, V - I)$ CMD, the hybrid $(I, I - K)$ CMD, and the purely NIR $(K, J - K)$ diagram. Black and orange dots mark, respectively, the stars considered to be Liller 1 members and Galactic field interlopers, according to the proper motion analysis described below in Section 2.1.3 (Dalessandro et al. 2022). The blue dots correspond to stars for which the proper motion measure is not available. The effect of differential reddening is well evident from the elongated morphology of the Red Clump, especially in the optical and hybrid CMDs.

building a single master-list that contains all the detected stars (some having magnitude measured in both filters, others having only the $I$ or the $K$ measure). The sources detected only in the $I$ images were then searched and analyzed also in the $K$ images, and vice versa, thus maximizing the information provided by the two filters separately. The final optical and NIR magnitudes of this combined analysis were homogenized to stand-alone HST and GeMS catalogs, respectively.

We reported the instrumental optical magnitudes onto the VEGAMAG photometric system by using the updated recipes and zero-points available in the HST web-sites[5]. To calibrate the IR magnitudes, we used the stars in common between GeMS and the VISTA Variables in the Vía Láctea (VVV) survey (Minniti et al., 2010). The calibration zero-points were then set as the difference between the J and$K$magnitudes in the two samples, after applying an iterative $3\sigma$-clipping algorithm.

[5]https://www.stsci.edu/hst/instrumentation/acs/data-analysis/zeropoints

Instrumental coordinates (x,y) were first reported to the HST ACS/WFC reference frame. Then they were corrected for geometric distortions by using prescriptions by Anderson & Bedin (2010) and Ubeda et al. (2012) and were then transformed to the absolute coordinate $(\alpha, \delta)$ system by using stars in common with the publicly available early Gaia Data Release 3 (Gaia eDR3) catalog (Gaia Collaboration et al., 2021). About 200 stars have been matched by using the cross-correlation tool `CataXcorr`, thus allowing a very precise determination of the stellar absolute positions. We note in passing that almost all the stars in common with the Gaia catalog are disc field stars. The resulting $1\sigma$ astrometric accuracy is $\sim 0.1''$.

The magnitudes of the brightest stars ($K < 12.5$), which are saturated in the Gemini observations, have been recovered (up to $K \sim 10$) from the PSF photometry of VVV survey data performed by Mauro et al. (2013). The final catalog reports the $I$ and $K$ band magnitudes (together with the $V$ and $J$ ones, if measured) for 43,629 stars detected in both HST and GeMS images.

Their CMD distribution is shown in three different color and magnitude combinations in Figure 2.2: from left, to right, the optical $(I, V-I)$ CMD, the "hybrid" $(I, I-K)$ CMD, and the NIR $(K, J-K)$ one. As expected, extinction along the line of sight limits the deepness of the sample especially in the optical diagram. The differential effect of the reddening is particularly visible in the deformed morphology of the red clump, which appears to be largely stretched along the direction of the reddening vector (from top-left, to bottom-right), especially in the optical and hybrid CMDs. Moreover, as expected given its position in the Galaxy, the evolutionary sequences of Liller 1 are quite strongly contaminated by a significant fraction of field stars. Very prominent is the sequence visible at $I < 25$ and $(I-K) < 5.5$ and likely populated by young disk stars. This clearly shows that any meaningful analysis of the stellar populations of Liller 1 requires an appropriate modelling of the differential reddening effects (see Section 2.1.4), and the computation of proper motions (PMs) of the stars in its direction (see Section 2.1.3).

### 2.1.2 The deepest color-magnitude diagram of Liller 1

Figure 2.2 also shows that the best images (in terms of both spatial resolution and limiting magnitudes) are those acquired through the $I$ and the $K$ filters. For this reason, the upper panel of Figure 2.3 shows the $(I, I-K)$ CMD obtained from these observations, sampling a $\sim 90'' \times 90''$ region (green area in Figure 2.1) centered on the centre of gravity of the stellar system (Saracino et al. 2015). In spite of the evident effect of differential reddening, the main evolutionary sequences are defined and the analysis of the CMD reveals a few major intriguing features:

1. a sparse stellar population defining a sequence at the blue edge of the CMD;

2. a dominant population typical of an old star cluster, consisting of cool and bright stars at the red side of the CMD, at $(I-K) \sim 6.5$, joining a rich MS extending down to $I \sim 26.5$;

3. a prominent Blue Plume (hereafter BP) at $(I-K) \sim 5.7$, appearing as an extension

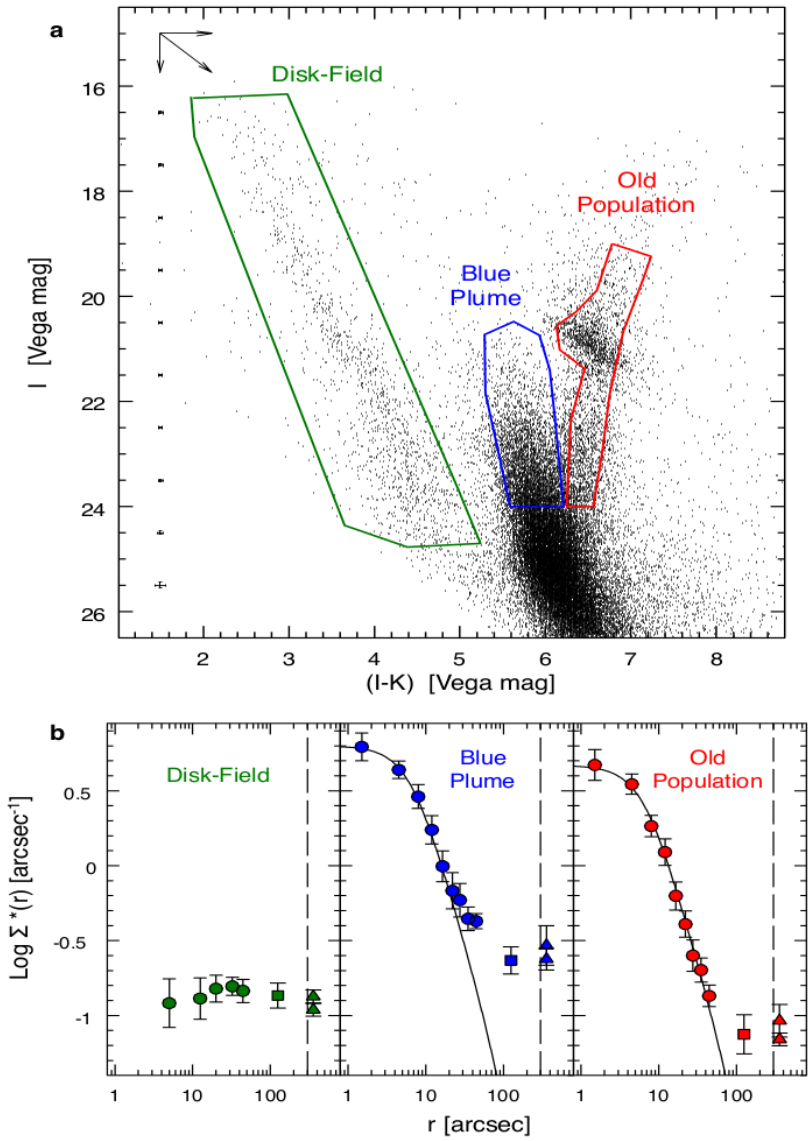


**Figure 2.3:** Panel (a): optical/NIR colour-magnitude diagram of Liller 1, approximately sampling the $90'' \times 90''$ central region of the system, as obtained from the combination of HST/ACS and GeMS/GEMINI observations. Three main subpopulations can be distinguished: (1) a sparse blue population at $(I - K) < 5$ that is related to the MS of the Galactic disk (thus it is named Disk-Field population), indicated by the green box; (2) a group of bright red stars, with $(I - K) \sim 6.5$, that joins a well populated MS extending from $I \sim 24.5$ down to $I \sim 26.5$, tracing an old metal-rich component (Old Population, OP), marked with the red box; and (3) a peculiar Blue Plume (BP) tracing a sub-population of young stars, evidenced with a blue box. The mean errors (1 s.e.m.) in magnitude and colour are reported on the left for 1 magnitude-wide bins. The reddening vector is also shown. Panel (b): star density profiles of the three subpopulations identified in the direction of Liller 1. The colored circles correspond to the stellar density values measured in the HST-GEMINI ($r < 50''$) field of view. Squares and triangles symbols correspond to stellar density values obtained from archival HST/NICMOS (GO 7318) and parallel HST/WFC3 (GO 15231) observations. They sample, respectively, an intermediate ($110'' < r < 140''$) and external ($r > 300''$) field of view. The error bars refer to the $1\sigma$ uncertainty. The vertical shaded line marks the tidal radius of Liller 1. The solid line is a King model with core radius $r_c = 7''$.

of the old MS, which was also visible in the pure NIR CMD at $(J - Ks) \sim 1.8$ and $15.5 < K < 17.5$.

While the first component is related to the MS of the Galactic disk (see below; we thus name it Disk-Field population), the dominant one shows all the properties typical of an old metal-rich component, with a well populated Red Giant Branch (RGB) extending more than 6 magnitudes and a well-defined RC at $I \sim 21$. Hereafter, we refer to this component as Old Population (OP). The most astonishing feature in the CMD is the BP, which is very populated, extends for approximately 4 magnitudes, and flows with no discontinuity into the MS of the OP: indeed, such a component is totally unexpected in the CMD of an old GC.

To understand the nature of this component, we determined the star density profile of the three sub-populations selected in Figure 2.3 a, with respect to the Liller 1 centre (Saracino et al. 2015), by following the same procedure already adopted in previous papers (Lanzoni et al. 2007, 2010, 2019). In short, we divided the HST-GEMINI field in 9 concentric annuli centred on the gravitational centre of the system, each one split in (typically) four subsectors. For the three selected subpopulations, we then counted the number of stars lying within each subsector and divided it by the subsector area. The stellar density in each annulus was finally obtained as the average of the subsector densities, and the standard deviation among the subsectors densities was adopted as error. The resulting stellar density profiles $\Sigma_\star(r)$, in units of number of stars per square arcsecond, are shown (circles) in Figure 2.3 b. While the Disk-Field population shows the standard flat profile expected for a pure field population, the BP and the OP appear highly concentrated toward the cluster centre, designing a well peaked profile nicely reproduced by the same King model (solid lines). This clearly indicates that, although affected by some level of field contamination (manifested by the flattening of the profile at large distances $r > 100''$), both populations belong to Liller 1.

### 2.1.3 Proper motion analysis

However, to properly separate cluster members from Galactic field interlopers, stellar PMs are of prime necessity. Unfortunately, Gaia eDR3 PM measures exist for only $\sim 200$ stars in the system. They are mostly distributed along the brightest portion of blue disk population, and, because of their intrinsic faint magnitudes, the available astrometric measurements suffer from significant uncertainties (up to $\sim 0.5$ mas yr$^{-1}$). Therefore, to clean the observed CMD from field star interlopers, we performed a relative PM analysis. In Saracino et al. (2019) it is shown that it is possible to efficiently use GeMS images in combination with the HST data to derive reliable relative PMs also in dense GCs (see also Fritz et al. 2017).

We used the ACS/WFC and the GeMS/GSAOI data sets, which are separated by a temporal baseline of $\sim 6.3$ yr, as first and second epochs, respectively. PMs were derived by following the approach adopted by Saracino et al. (2019) (see also Dalessandro et al. 2013). The procedure consists in determining the displacement of the centroids of the stars measured in the two epochs, once a common coordinate reference frame is defined.

The first step is to adopt a distortion-free reference frame, which we will call master frame hereafter. The master frame catalog contains stars measured in all the ACS/WFC $I$ band single-exposures. Their coordinates were corrected for geometric distortions as described in Section 2.1.1. To derive accurate transformations between the second epoch catalogs and the master catalog, we selected a sample of $\sim 3300$ bona-fide stars having magnitude $20 < I < 24.5$ (corresponding approximately to magnitudes $13.0 < K < 18.5$), which we judged to be likely cluster members on the basis of their position in the CMD (i.e., stars distributed along the lower RGB, SGB and upper MS). We then applied a six-parameter linear transformation to report stars in the second epoch catalogs to the master coordinate reference frame, by using the stars in common. We treated each chip separately, in order to maximize the accuracy. Moreover, we carefully corrected the coordinates of stars in the second epoch catalogs for the important geometric distortions affecting the GSAOI camera by using the geometric distortions solutions published in Dalessandro et al. (2016).

The mean position of a single star in each epoch ($x_m$, $y_m$) has been measured as the $3\sigma$ clipped mean position calculated from all the $N$ individual single-frame measurements. The relative rms of the position residuals around the mean value divided by $\sqrt{N}$ has been used as associated error ($\sigma$). Finally, the displacements are obtained as the difference of the positions ($x_m$, $y_m$) between the two epochs for all the stars in common. The error associated with the displacement is the combination of the errors on the positions of the two epochs. We should stress here that the first epoch is by construction in the same coordinate reference frame as the master catalog. The relative PMs ($\mu_x, \mu_y$) are finally determined by measuring the difference of the mean x and y positions of the same stars in the two epochs, divided by their temporal baseline $\Delta T = 6.3$ yr. Such displacements are in units of pixels yr$^{-1}$. We then iterated this procedure a few times by removing likely non-member stars from the master reference frame based on the preliminary PMs obtained in the previous iterations. The convergence is assumed when the number of reference stars that undergoes this selection changes by less than $\sim 10\%$ between two subsequent steps. At the end we derived relative PMs for 35,761 stars in the area where the HST and GeMS datasets overlap (see Figure 2.1).

The leftmost panels of Figure 2.4 show the derived vector point diagrams (VPDs) at different magnitude levels. As expected, the PM distributions get broader for increasing magnitudes because of the increasing uncertainties of the centroid positions of faint stars. To build a clean sample of stars with a high membership probability, we defined for each magnitude bin a different fiducial VPD region centered on (0,0). The fiducial regions have radii of $3 \times \sigma$, where $\sigma$ is the average PM error in that magnitude bin. The sample of stars thus selected corresponds to the observational catalog made of likely Liller 1 member stars. As shown in Figure 2.4, the Disk-Field population is removed by the PM analysis and the level of contamination from field stars along the OP and the BP is appreciable from the comparison between the field and the cluster member CMDs.

The cluster member CMD shows the indisputable presence of the BP, fully confirming that this population does belong to Liller 1. Figure 2.4 c shows the VPD of the three subpopulations selected from the boxes depicted in Figure 2.3 a. Interestingly, the Disk-Field and the OP distributions are very different, and the BP appears to host both these

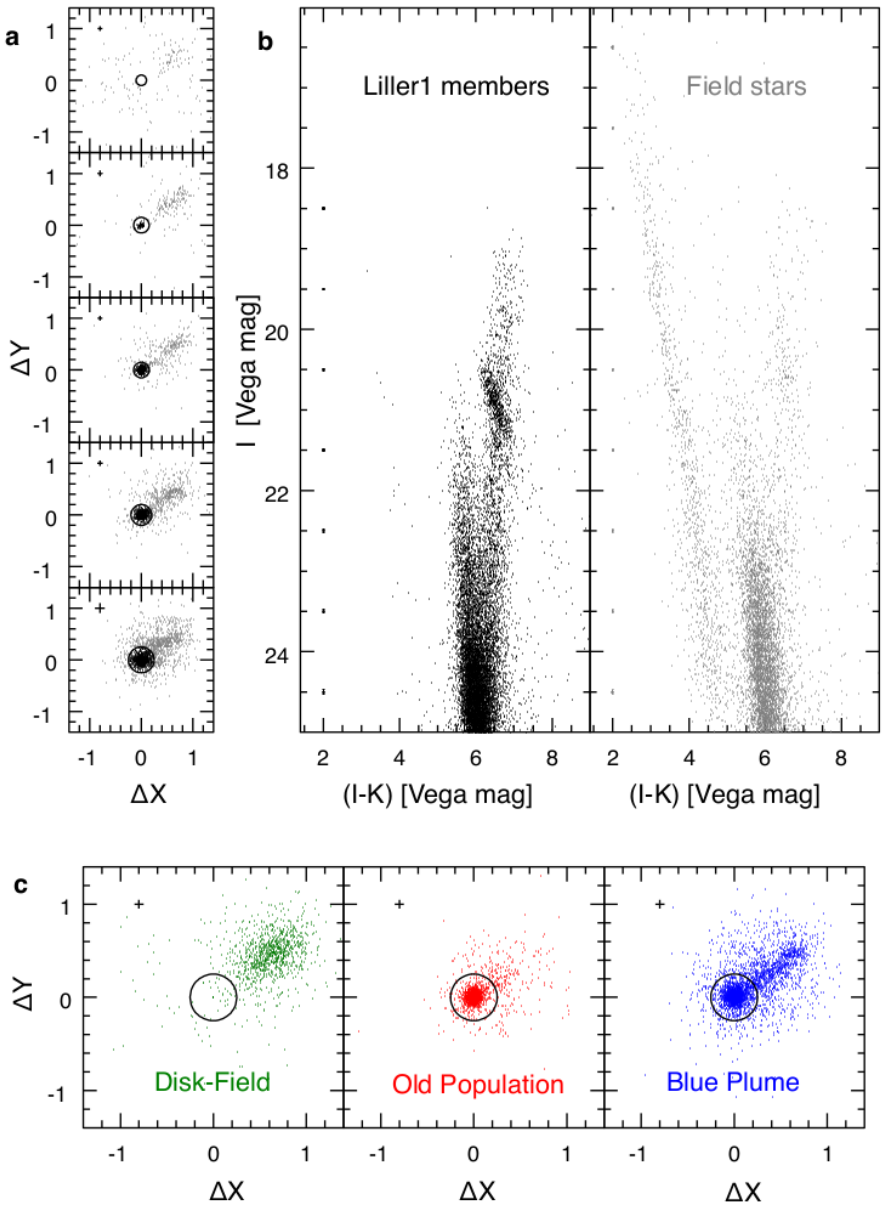


**Figure 2.4:** Panel (a): vector-point diagrams (VPD) of the relative PMs (in units of the ACS/WFC pixel, corresponding to 0.05″) measured for stars in five magnitude bins. The stars included within the circles centred on (0,0) are selected as cluster members (black dots), while those outside the circles are considered as field interlopers (grey dots). The radius of each circle corresponds to 3 times the typical PM error in the magnitude bin (which is marked with the crosses shown in each panel). Panel (b): CMDs of Liller 1 members (left, in black) and field stars (right, in grey) as obtained from the PM analysis. Both panels show the mean errors (1 s.e.m.). Panel (c): VPDs for the three subpopulations (Disk-Field, OP, BP) selected by adopting the boxes shown in Fig 2.3. The Disk-Field component shows an elongated PM distribution avoiding the central portion of the VPD. Conversely, a circularly symmetric distribution around (0,0) is observed (as expected) for the OP.

components: a main population with kinematics perfectly consistent with that of the OP, and another component with elongated PM distribution similar that of the Disk-Field. The two components of the BP are well distinguished by the PM analysis, confirming beyond any doubt that the majority of the BP stars do belong to Liller1. The sample of

stars for which PMs have been measured corresponds to $\sim 80\%$ of the total.

To more precisely define the evolutionary sequences in the CMD, the next mandatory step is the correction for the effects of differential reddening, which is highly variable on small scales in the direction of Liller 1.

### 2.1.4 High spatial resolution extinction map in the direction of Liller 1

Liller 1 lies very close to the Galactic plane, in a region that is affected by large and spatially variable foreground extinction. This is the main reason hindering detailed photometric investigations of its stellar population. One of the first works about the extinction toward Liller 1 dates back to the eighties, when Armandroff & Zinn (1988) estimated a color excess $E(B-V) = 2.7$. Then, Frogel et al. (1995) found $E(J-K) = 1.7$, corresponding to extinction coefficients $A_K = 0.87$, $A_V = 9.5$ and $E(B-V) = 3.0$. In the same work the authors analyzed an offset field and found a larger extinction coefficient, thus suggesting the presence of differential reddening. Later works, both in the optical (Ortolani et al., 1996) and mainly in the NIR (Ortolani et al. 2001; Barbuy et al. 1998; Davidge 2000; Valenti et al. 2010), found values of $E(B-V)$ ranging from 3 up to 3.13, and also highlighted the presence of differential absorption along the line of sight. Gonzalez et al. (2011, 2012) used data from the VVV Survey and derived the mean $(J-K)$ color of RC giants in 1835 sub-fields in the bulge region (also including the area covered by Liller 1); then, through the comparison with the color of similar stars in the Baade's window, they derived a reddening map with a maximum resolution of $2'$. According to the online simulator[6] based on this work, a color excess $E(J-K) = 1.42 \pm 0.16$, corresponding to $E(B-V) = 2.70$ is found in the direction of Liller 1. More recently, Saracino et al. (2015) built a reddening map of the central region of Liller 1 with a a spatial resolution of $18'' \times 18''$, finding a mean color excess $E(B-V) = 3.3 \pm 0.2$ and a maximum variation $\delta E(B-V) = 0.34$ within the surveyed FOV. Here we determine the first high-resolution differential reddening map in the direction of the system.

#### Reddening Laws

As is well known, interstellar reddening is due to the absorption and scattering of the radiation caused by dust clouds along the light path to the observer. This phenomenon makes the flux of a given source systematically fainter and the color systematically redder than their true (emitted) values, with an efficiency that strongly depends on the wavelength (increasing at shorter wavelengths). The entity of reddening is usually parametrized by the color excess $E(B-V)$, defined as the difference between the observed color $(B-V)$ and the intrinsic color $(B-V)_0$ that, for stars, is mainly fixed by the temperature of the source.

The extinction law, i.e., the dependence of the absorption coefficient on wavelength ($\mathrm{A}_\lambda$) can be expressed as (see also the formulations by Cardelli et al. 1989; O'Donnell 1994; Fitzpatrick 1999):

$$\mathrm{A}_\lambda = \mathrm{R}_V \times c_{\lambda,\mathrm{R}_V} \times \mathrm{E}(B-V), \tag{2.1}$$

[6] *http://mill.astro.puc.cl/BEAM/calculator.php*

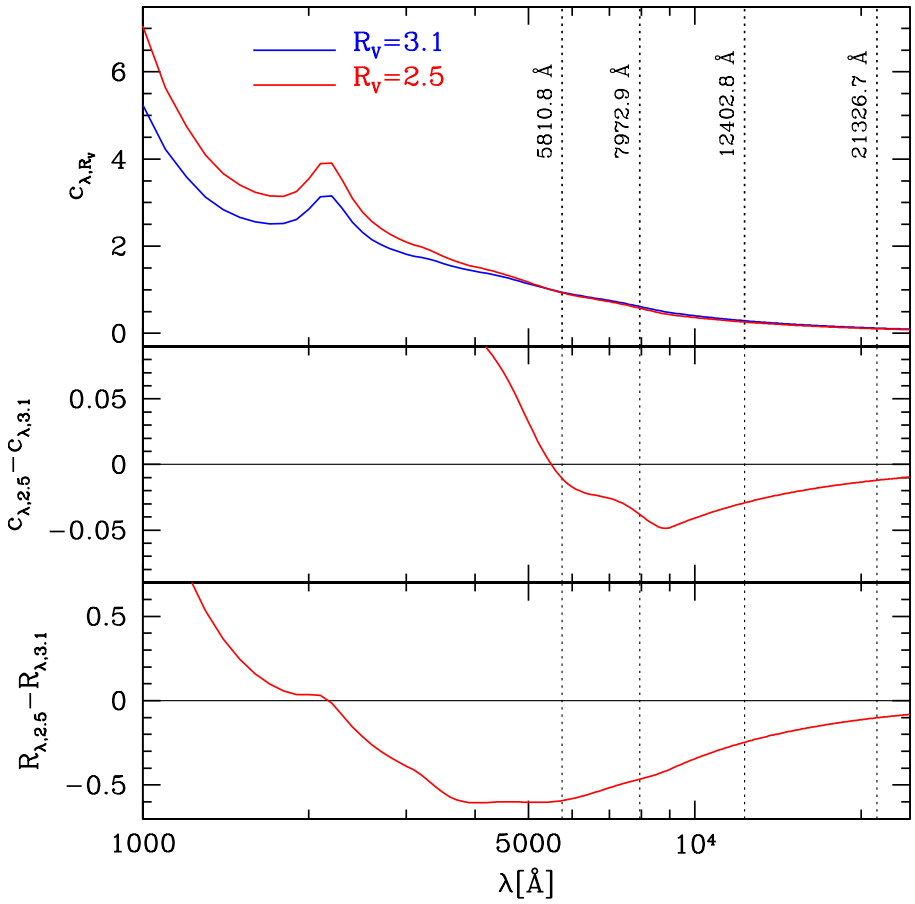


**Figure 2.5:** *Upper panel:* Dependence of the extinction law $c_{\lambda,\mathrm{R}_V}$ (or $\mathrm{A}_\lambda/\mathrm{A}_V$) on wavelength for two different assumptions of the $\mathrm{R}_V$ coefficient: the standard value for diffuse interstellar medium $\mathrm{R}_V = 3.1$ (blue line), and $\mathrm{R}_V = 2.5$ (red line). The vertical dotted lines are drawn in correspondence of the central wavelengths of the four photometric filters used in this work (see labels). *Middle panel:* Difference between $c_{\lambda,2.5}$ and $c_{\lambda,3.1}$ as a function of wavelength. *Lower panel:* Difference between $\mathrm{R}_{\lambda,2.5}$ and $\mathrm{R}_{\lambda,3.1}$ as a function of wavelength, with $\mathrm{R}_{\lambda,\mathrm{R}_V}$ defined as the product between $\mathrm{R}_V$ and $c_{\lambda,\mathrm{R}_V}$, or the ratio between the absorption coefficient $\mathrm{A}_\lambda$ and the color excess $E(B-V)$.

where $c_{\lambda,\mathrm{R}_V} = 1$ is commonly adopted at the $V$-band wavelength ($c_{V,\mathrm{R}_V} = 1$). The parameter $\mathrm{R}_V$ is usually set equal to 3.1, which is the standard value for diffuse interstellar medium (Schultz & Wiemer 1975; Sneden et al. 1978). This is indeed the value assumed in all previous works devoted to the estimate of reddening in the direction of Liller 1 (see previous paragraph). Particular attention, however, has to be given to the extinction toward the inner Galaxy (Popowski 2000; Nataf et al. 2013; Alonso-García et al. 2011; Casagrande & VandenBerg 2014; Pallanca et al. 2021a, and references therein), where the $\mathrm{R}_V$ value seems to vary along different directions. For example Nataf et al. (2013) suggested that $\mathrm{R}_V = 2.5$ is more appropriate to reproduce the bulge populations, while some other authors quote larger values (e.g., $\mathrm{R}_V = 3.2$; Bica et al. 2016; Kerber et al. 2019).

Decreasing the value of $\mathrm{R}_V$ makes the parameter $c_{\lambda,\mathrm{R}_V}$ (thus, the extinction law $\mathrm{A}_\lambda/\mathrm{A}_V$)

more steeply dependent on wavelength. This is illustrated in the upper panel of Figure 2.5, where the two curves refer to the canonical $R_V$ value ($R_V = 3.1$, blue line) and to $R_V = 2.5$ (red line). As shown in the central panel of the figure, the difference between $c_{\lambda,2.5}$ and $c_{\lambda,3.1}$ is quite small in the photometric bands considered in this analysis (marked by the dashed vertical lines). However, this difference increases by one order of magnitude when these coefficients are multiplied by their respective value of $R_V$: this is shown in the bottom panel of the figure, plotting $R_{\lambda,R_V} \equiv R_V \times c_{\lambda,R_V}$. In turn, recalling that $E(B-V) = A_\lambda/R_{\lambda,R_V}$, this implies that any given value of the absorption coefficient $A_\lambda$ corresponds to a significantly different color excess $E(B-V)$ if $R_V = 2.5$ is assumed in place of the standard value $R_V = 3.1$. Hence, the value of $E(B-V)$ and the distance modulus ($\mu_0$) necessary to superpose an isochrone onto an observed CMD change if $R_V = 2.5$ is adopted instead of $R_V = 3.1$. The bottom panel of Figure 2.5 also shows that the difference between $R_{\lambda,2.5}$ and $R_{\lambda,3.1}$ is not constant, but significantly increases (in absolute value) for decreasing wavelength in the range relevant for the present study: it varies between $\sim 0.1$ at $\lambda \simeq 21326.7$ Å (the $K$ band) and $\sim 0.6$ at $\lambda \simeq 5810.8$ Å (the effective wavelength of the F606W filter; Rodrigo et al. 2012; Rodrigo & Solano 2020)[7]. In turn, the increasing difference between $R_{\lambda,2.5}$ and $R_{\lambda,3.1}$ for decreasing wavelength necessarily implies that the two isochrones - the one shifted to the observed plane by adopting $R_V = 3.1$, the other shifted under the assumption of $R_V = 2.5$ - cannot simultaneously reproduce the NIR and the optical CMDs of a stellar system.

This is illustrated in Figure 2.6, where the optical $(I, V-I)$, hybrid $(I, I-K)$ and NIR $(K, J-K)$ CMDs of Liller 1 are shown together with an isochrone (Bressan et al. 2012; Marigo et al. 2017) computed for an age $t = 12$ Gyr and a global metallicity [M/H] $= -0.3$ dex (the choice of the age-metallicity parameters is driven by the values adopted in Ferraro et al. 2016 in the case of Terzan 5). The black dashed line shows the location in the three CMDs of the isochrone obtained by assuming $R_V = 3.1$, $E(B-V) = 3.30$ and $\mu_0 = 14.55$, which are the values needed to make it reproduce the observed NIR CMD (Saracino et al. 2015). However, no reasonable match of the observations can be simulatenously obtained in the optical and hybrid CMDs. Conversely, by adopting $R_V = 2.5$ (red line) all the evolutionary sequences of the cluster in any wavelength combination are well reproduced. This demonstrates that the canonical reddening law is not appropriate in that direction of the sky, and a much lower value of $R_V$ is needed toward Liller 1, in agreement with what suggested in the pioneering work of Frogel et al. (1995) and what previously found for other bulge directions (e.g.,Popowski 2000; Nataf et al. 2013; Alonso-García et al. 2017; Casagrande & VandenBerg 2014; Saha et al. 2019; Pallanca et al. 2021a).

The manifest inadequacy of $R_V = 3.1$ in the direction of Liller 1 came not into light in previous works because they were all based on NIR or optical datasets separately: it is indeed the simultaneous analysis of these CMDs that finally revealed the necessity of a much lower value of $R_V$. Of course, however, a proper comparison between theoretical isochrones and observations first requires to correct the CMDs for the effects of differential

[7]Following the prescriptions of Cardelli et al. (1989) and O'Donnell (1994), we find that, if $R_V = 3.1$, the corresponding values in the four photometric bands here considered are: $R_{606} = 2.89$, $R_{814} = 1.90$, $R_J = 0.89$, and $R_K = 0.37$. If $R_V = 2.5$, then: $R_{606} = 2.30$, $R_{814} = 1.43$, $R_J = 0.64$, and $R_K = 0.27$.

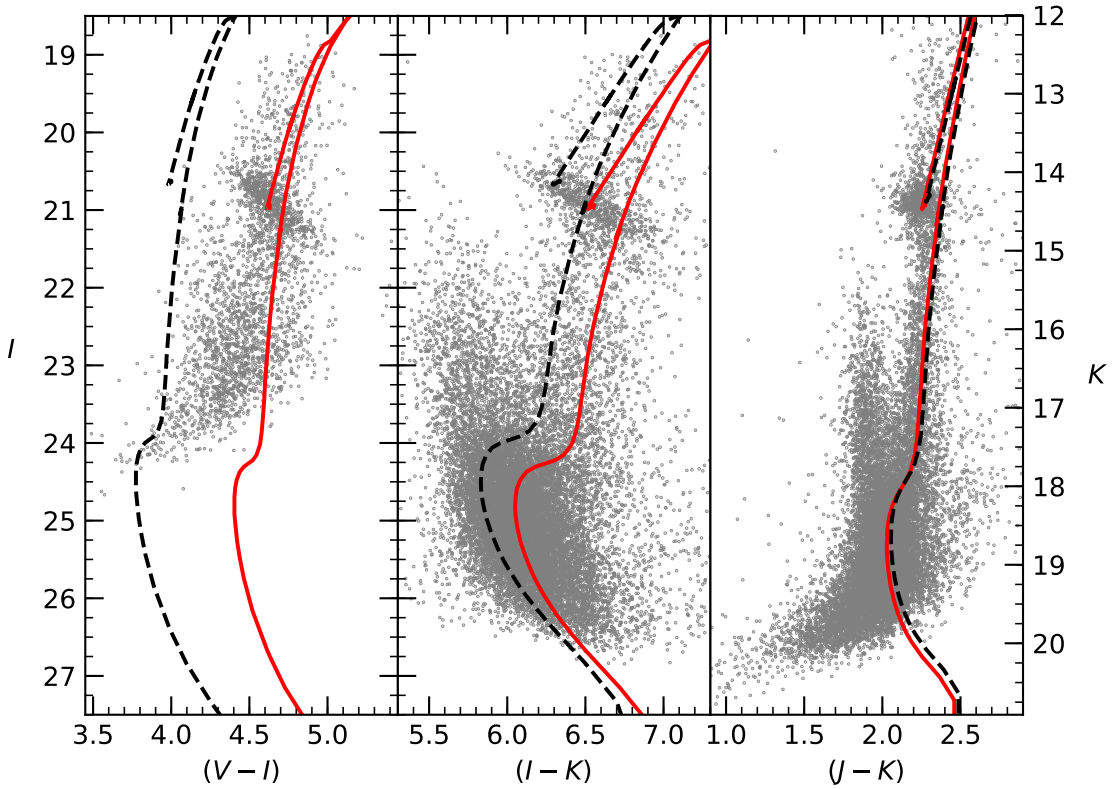


**Figure 2.6:** Optical, hybrid and NIR CMDs of Liller 1 obtained from well-measured and PM-selected member stars (grey dots), with a 12 Gyr old, [M/H] = −0.3 dex isochrone superposed. The black dashed line marks the position of the isochrone in the three CMDs obtained under the assumption of $R_V = 3.1$ by requiring that it well reproduces the NIR CMD: the corresponding values of mean absolute color excess and distance modulus are: $E(B-V) = 3.30$ and $\mu_0 = 14.55$ (Saracino et al. 2015). It is clearly unable to also match the hybrid and optical CMDs. The red solid line marks the position of the isochrone under the assumption of $R_V = 2.5$ and the request to well match the black dashed line in the NIR CMD, implying $E(B-V) = 4.52$ and $\mu_0 = 14.65$. As apparent, it well reproduces the observations in all the available color combinations.

reddening, which is responsible for the distortions of the evolutionary sequences clearly visible in Figure 2.6.

### Computation of the differential reddening map

The interstellar extinction along the Galactic plane and in the direction of the Galactic center can be highly spatially variable (differential reddening), on scales that can be as small as a few arcseconds. Since this spatial dimension is significantly smaller than the apparent size of most Galactic stellar systems, the CMD of star clusters affected by differential reddening shows a systematic elongation of all the evolutionary sequences along the direction of the reddening vector. In turn, this prevents the accurate characterization of their photometric properties, with a non negligible impact on the determination of fundamental parameters such as, for instance, the distance and age (e.g., Bonatto et al.

2013).

To model and correct for the effect of differential reddening in GCs, two main approaches have been adopted in the literature. Schematically: (1) the "cell by cell" method, which consists in dividing the observed FOV in a number of cells, build the CMD of the stars included in each cell, and calculate the reddening value in each cell from the color and magnitude displacements with respect to the bluest CMD (Piotto et al. 1999; von Braun & Mateo 2001; McWilliam & Zoccali 2010b; Nataf et al. 2010; Gonzalez et al. 2011, 2012; Massari et al. 2012; Bonatto et al. 2013; Saracino et al. 2015), and (2) the "star by star" approach, which consists in estimating the reddening of each star in the catalog from the relative displacement between its "local CMD", i.e., the CMD built with the spatially closest objects, and the cluster mean ridge line (Milone et al. 2012; Bellini et al. 2013; Saracino et al. 2019; Pallanca et al. 2021a; Cadelano et al. 2020). In the cited papers, different authors used stars in different evolutionary sequences as reference for the determination of the color and magnitude displacements: MS, horizontal branch, red giant branch (RGB) stars, and even variable RR Lyrae (Alonso-García et al. 2011 and references therein). In all cases, the spatial resolution is driven by the need for a statistically reliable sample of stars to build the cell or local CMDs. To determine the differential extinction map in the direction of Liller 1 we used the "star by star" method, adopting the RGB, sub-giant branch (SGB) and bright MS stars as reference, as already tested in a previous work (Pallanca et al., 2021a). In addition, because of the results discussed in the previous section, we adopted $R_V = 2.5$.

The first step consists in the definition of the reference mean ridge line (MRL) of the OP of Liller 1. This has been determined in the proper motion cleaned, hybrid $(I, I-K)$ CMD, which is significantly deeper than any other available color-combination (even more than the $(K, J-K)$ CMD which is likewise deep but with a worst signal to noise ratio in the $J$ filter at the bottom of the MS; see Figure 2.2), thus allowing us to also use stars along the SGB and MS phases. In turn, this implies a significant increase of the spatial resolution of the output reddening map, with respect to the case where only RGB stars could be used. In order to remove poorly measured objects that can bias the procedure, we first considered only stars with high-quality photometry, by adopting $3\sigma$ cuts in the *chi* and *sharpness* parameter distributions. The considered sample, comprising the RGB, SGB and the upper MS of the OP, was divided in magnitude bins of variable size (ranging from 0.25 to 1 mag), in order to best sample the morphological changes of the sequence in the MS turnoff region. The mean color of each considered bin was then determined after a $3\sigma$-clipping rejection, in order to remove any residual interlopers.

Once the MRL is defined, we considered all the stars in the catalog (i.e., not only the high-quality objects) and for each of them we selected, from the high-quality pool (and proper motion selected) sample, the $N_*$ sources spatially lying in the vicinity of the star under investigation. The method consists in determining the value of $\delta E(B-V)$ required to shift the MRL of the system along the direction of the reddening vector until it fits the local CMD defined by these $N_*$ nearby sources. Of course, the larger the number of sources ($N_*$) is, the better defined the local CMD is. However, to keep the spatial resolution as high as possible, we constrained $N_*$ below a maximum value and we assumed

a limiting radial distance ($r_{\rm lim}$) within which the nearby sources can be selected. We set $N_{*,\rm max} = 30$ and $r_{\rm lim} = 3''$. As soon as one of these two conditions is satisfied, the other one is no longer considered. Since the stellar density is higher in the center and decreases with radius, this approach naturally yields an "adaptive grid" producing reddening maps with higher (lower) spatial resolution in the central (external) regions.

As described in the previous section, the sub-sample with measured PM represents about 80% of the entire sample. In particular due to dithering patterns adopted in the GeMS/GSAOI observations (aimed at covering the inter-chip gaps), a sort of external corona and a central cross of the FOV was not properly sampled by all the considered NIR exposures to allow accurate PM measures. Thus, the procedure aimed at the construction of the reddening map has been applied twice. The first time, only stars classified as Liller 1 members from their measured proper motion were included in the high-quality pool. The second time, in order to cover the entire FOV, no proper motion selection was used. The differential reddening estimates obtained from these two approaches are fully compatible (as already found for NGC 6440 in Pallanca et al. 2021a), demonstrating that the potential presence of a few field interlopers does not affect the result. Hence, the final differential reddening value assigned to each star has been obtained, whenever possible, from the (formally more rigorous) proper motion based method, and complemented with the value derived neglecting the proper motion selection in the other cases.

Because of the large central densities, the number of stars within a circle of $3''$ radius is typically much larger than 30 in the inner cluster regions; hence the $N_{*,\rm max}$ closest sources are typically selected within a distance much smaller than $r_{\rm lim}$ from each star under investigation in this region. The opposite is true in the outskirts, where the driving parameter for the selection of nearby sources becomes $r_{\rm lim}$. This is clearly visible in the left panel of Figure 2.7: the distance used for the selection of the nearby stars defining the local CMD can be as small as $1''$ in the central regions, while it increases up to the maximum value ($r_{\rm lim} = 3''$) close to the boundaries of the analysed FOV, where only semicircles toward the center can be drawn. The few spots visibile on the map correspond to local increases of the selection radius due to the presence of saturated stars. The discontinuities in the innermost spot and at the outermost edge of the FOV are due to the transition between reddening estimates that take into account/neglect the proper motion condition (which is unavailable in these regions: by keeping larger numbers of stars, this allows us to use a slightly smaller selection radius).

The comparison between the MRL of the cluster OP and the local CMDs has been performed in the magnitude range $19.5 < I < 26$, in order to discard potentially saturated and too faint (hence not well measured) objects. We also performed a $3\sigma$ rejection in order to exclude from the analysis all the stars with a color distance from the MRL significantly larger than that of the bulk of the selected objects. This is useful to exclude field interlopers not removed by the proper motion analysis and/or discard non canonical stars with intrinsic colors different from those of the cluster main populations (Pallanca et al. 2010, 2013, 2014; Cadelano et al. 2015; Dalessandro et al. 2014; Ferraro et al. 2015, 2016, 2018a).

The comparison was performed by shifting the MRL along the reddening direction

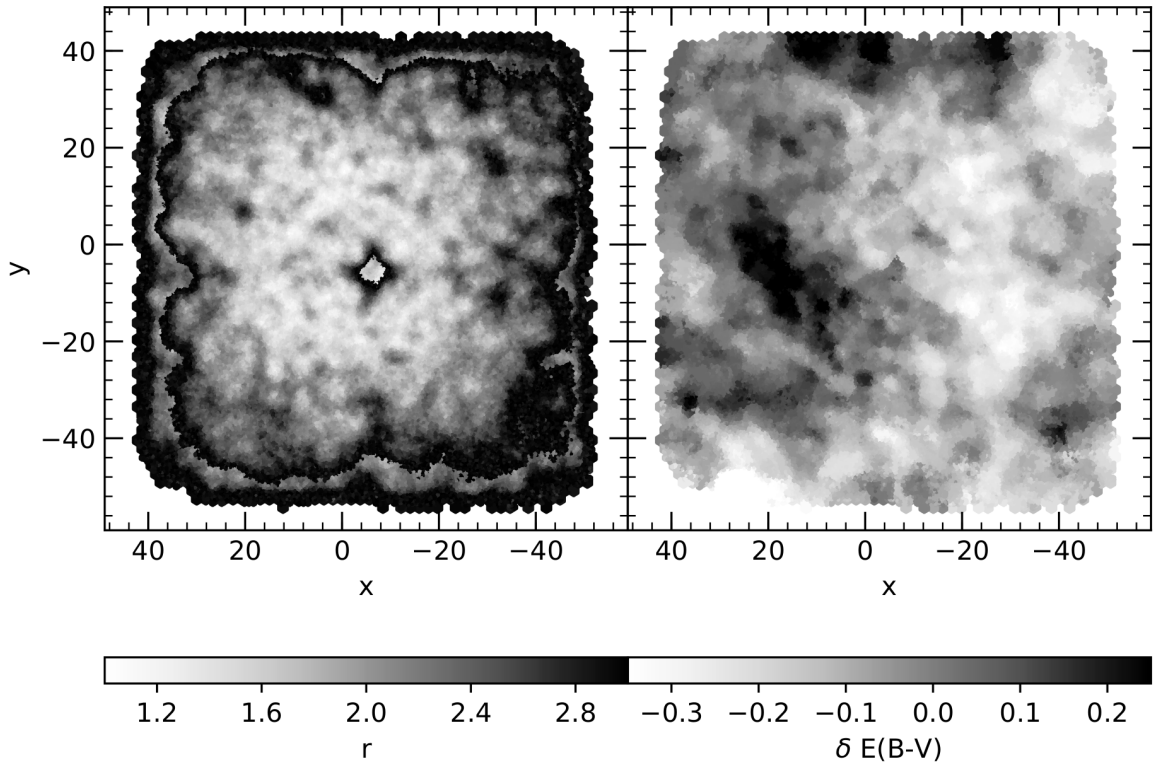


**Figure 2.7:** *Left panel:* Map of the radial distances ($r$, arcsec) used to select the samples of nearby sources for the construction of the "local CMD" of every star in the procedure adpoted to determine the differential reddening map. Lighter colors are associated to the best reached spatial resolution ($\sim 1''$), while darker colors correspond to the regions where $r_{\rm lim} = 3''$ is reached. The discontinuities in the $r$ distribution are due to the two different catalogs (with and without the proper motion information) used to estimate the differential reddening. See Section 2.1.4 for more details. *Right panel:* Differential reddening map. The values of $\delta{\rm E}(B-V)$ are both negative and positive since they are referred to the MRL of the OP. The associated colorbar codifies the $\delta{\rm E}(B-V)$ values ranging from less extincted regions (lighter colors) to more extincted areas (darker colors).

(which is fixed by the adopted extinction law) in steps of $\delta{\rm E}(B-V)$. For each considered step, we calculated the residual color $\Delta IK$ as:

$$\Delta IK = \sum_{i=1}^{N_*} \left( |IK_{{\rm obs},i} - IK_{{\rm MRL},i}| + w_i \cdot |IK_{{\rm obs},i} - IK_{{\rm MRL},i}| \right), \tag{2.2}$$

where $IK_{{\rm obs},i}$ is the $(I-K)$ color observed for each of the $N_*$ selected objects constituting the local CMD, $IK_{{\rm MRL},i}$ is that of the MRL at the same level of magnitude, and the weight $w_i$ takes into account both the photometric error on the color ($\sigma$) and the spatial distance ($d$) of the $i^{\rm th}$ source from the star under investigation, according to the following

expression:

$$w_i = \frac{1}{d_i \cdot \sigma_i} \left[ \sum_{j=1}^{N_*} \left( \frac{1}{d_j \cdot \sigma_j} \right) \right]^{-1} . \tag{2.3}$$

The second term is meant to give more weight to the closest stars, thus increasing the accuracy of the local reddening estimate, reducing the impact of using large selection distances where the level of dust absorption could change. Note that we cannot reduce equation (2.2) to the second term only, because a bright object (with small photometric errors) close to the central star would dominate the weight and make the reddening estimate essentially equal to the value needed to move the MRL exactly on that object. The final differential reddening value assigned to each star is the value of the step $\delta E(B-V)$ that minimises the normalised residual color ($\Delta IK/N_*$). The spatial distribution of differential extinction values thus derived for each star constitutes the differential reddening map shown in the right panel of Figure 2.7.

We emphasize that in the adopted procedure, the value of $\delta E(B-V)$ assigned to each star is not guided by its position in the CMD with respect to the cluster MRL, but by the position of its $N_*$ neighboring stars (i.e., the $N_*$ stars spatially adjacent on the plane of the sky to the object under analysis). This ensures that we are correcting for a phenomenon - differential reddening - affecting the region of sky where the star is located, not for possible intrinsic properties of the star itself (e.g., its chemical abundance).

Following the procedure described above, we built the differential reddening map in the direction of Liller 1, over a total FOV of about $90 \times 90''$, and with an angular resolution smaller than $3''$(right panel of Figure 2.7). It appears patchy on spatial scales of just a few arcsecs, and it presents two main highly-reddened blobs located on the east and north sides of the sampled FOV. The less absorbed region (lighter color in the figure) is located in an almost vertical strip on the west side, flowing into the north-west and south-east corners. Overall, the map graphically demonstrates a large amount of differential reddening, with $\delta E(B-V)$ ranging between $-0.57$ to 0.37. This corresponds to differential absorptions of 2.16, 1.35, 0.60 and 0.25 mag in the $V$, $I$, $J$ and $K$ filters, respectively. Note that the maximum variation of E$(B-V)$ found here ($\sim 0.9$) is significantly larger than that estimated in Saracino et al. (2015), who quote $\delta E(B-V) = 0.34$. This is however expected both because of the larger $E(B-V)$ (for a constant percentage of variation, the larger is the absolute value, the larger is the variation), and because of the different spatial resolution of the two reddening maps. In fact, the much larger cells ($18'' \times 18''$) in the map of Saracino et al. (2015) have the effect of smoothing local fluctuations, hence decreasing the amplitude of the $E(B-V)$ variations.

### 2.1.5 The detection of multi-age stellar populations in Liller 1

The CMD of the PM-cleaned and differential reddening corrected (DRC) stellar population of Liller 1 is shown in Figure 2.8 a. It clearly confirms the complexity of the system: Liller 1 hosts an ensemble of stars not following the evolutionary sequences typical of an old stellar population. This BP appears very well populated, counting a number of objects comparable to that of the OP in the same magnitude range. The cumulative

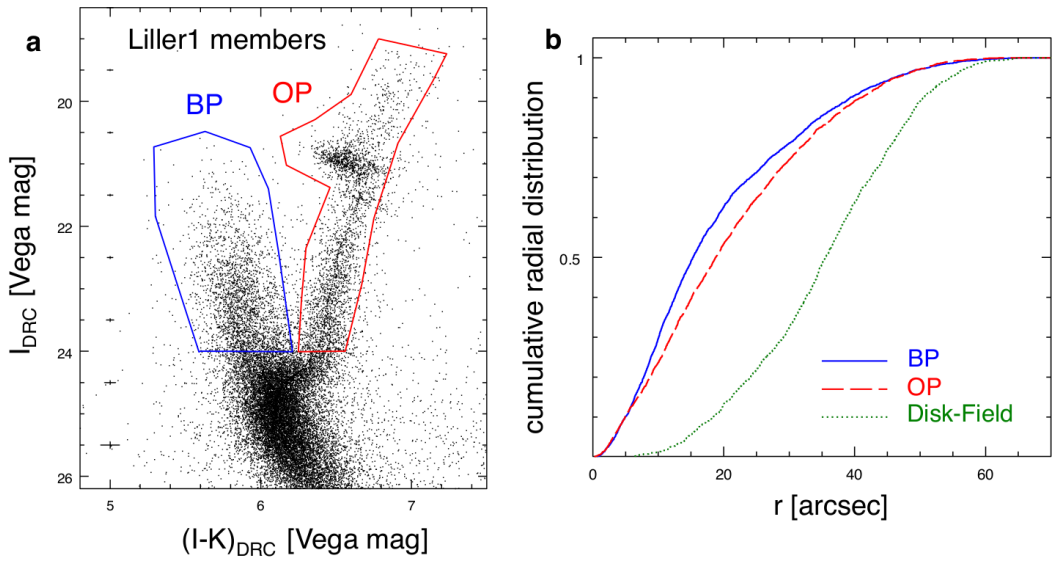


**Figure 2.8:** Panel (a): CMD of the PM-selected members of Liller 1 with magnitudes ($I_{\rm DRC}$) and colours ($(I-K)_{\rm DRC}$) corrected for differential reddening. The selection boxes of the BP (in blue) and OP (in red) used for the study of their radial distribution are also shown. The mean errors (1 s.e.m.) in magnitude and colour are reported on the left for 1 magnitude-wide bins. Panel (b): cumulative radial distributions of the three sub-populations observed in the PM-selected CMDs of Liller 1. The numbers of stars counted in the selected components are: 2480 in the BP, 2916 in the OP, and 1109 in the Disk-Field.

radial distributions of the PM-cleaned samples (Figure 2.8 b) fully confirm the conclusions above: following the Kolmogov-Smirnov test, the probability that the BP and the OP are extracted from the parent distribution describing the Disk-Field population is zero. Indeed, the BP appears even more centrally segregated toward the gravitational centre of Liller 1 than the OP, once more demonstrating its secure membership to the system and providing some additional insights on its origin (see below).

The BP population lies in the region of the CMD usually occupied by Blue Straggler Stars (BSSs, Ferraro et al. 1992). BSSs are anomalously massive (typically $\sim 1.2 M_{\odot}$, Raso et al. 2019) core hydrogen-burning stars thought to form through the evolution of binaries and stellar collisions (Ferraro et al. 2009). Since they originate from sporadic and uncorrelated events, only limited numbers of BSSs are expected to be produced and, in fact, they usually appear as a sparse population in the CMD of star clusters: only small numbers of BSSs are commonly observed - typically, less than 100-150 BSSs are found even in the most massive GCs (Ferraro et al. 2018a), the richest population detected so far counting about 300 BSSs in $\omega$ Centauri (Ferraro et al. 2006) - and their fraction with respect to RGB and horizontal branch stars in the cluster central regions typically amounts to less than 10-15%. In Liller 1, the BP counts a population of stars comparable to that of the OP: we observe 2480 BP stars brighter than $I_{\rm DRC} < 24$, compared to 2916 stars at the same level of magnitude along the OP. Once corrected for completeness (see Section 3.3.2 for further details), these numbers becomes even more similar: 3030 and 3100, respectively. Hence, the richness and the morphology of the BP population are more

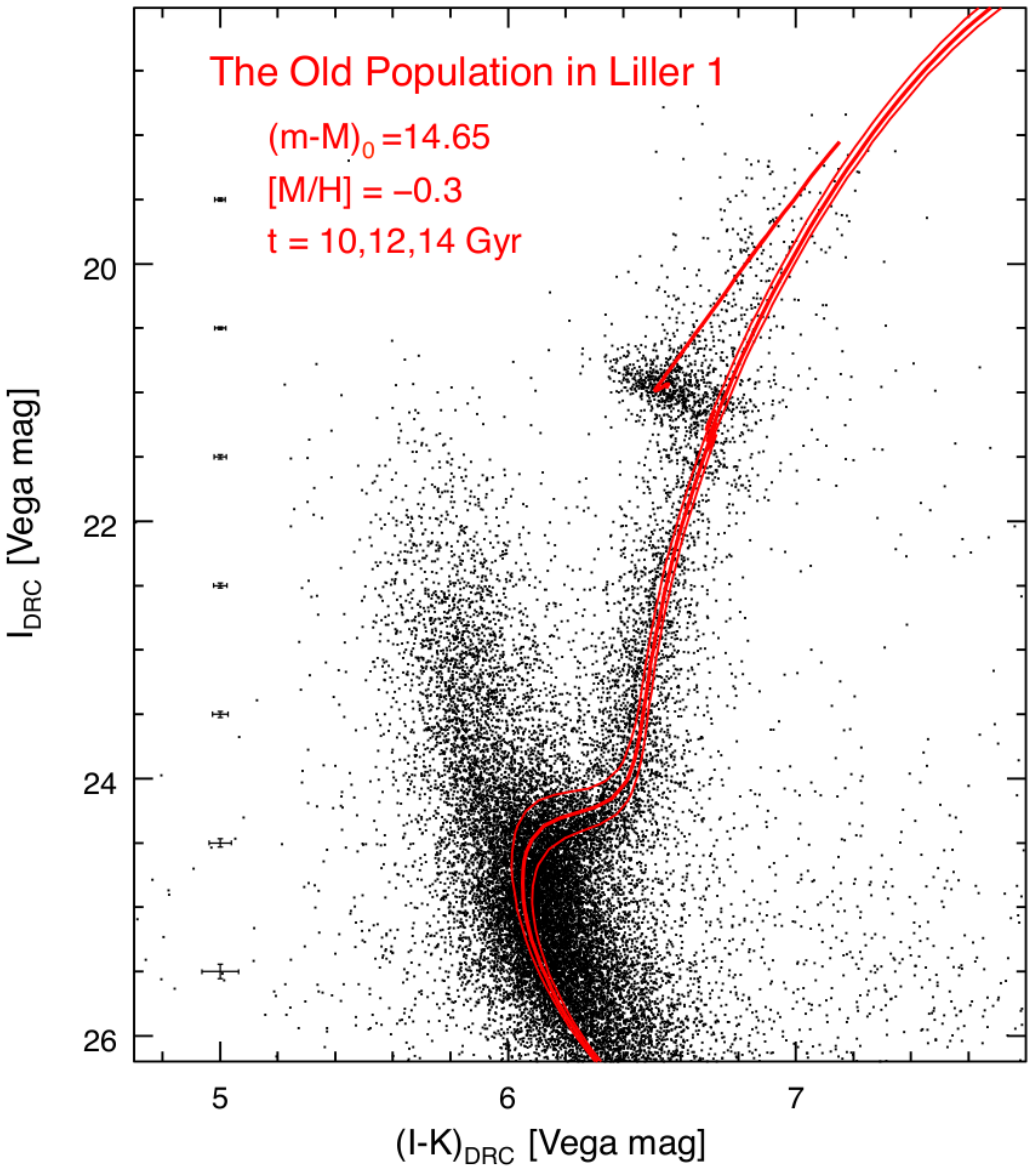


**Figure 2.9:** Differential reddening corrected CMD of Liller 1 with three isochrones of different ages (10, 12 and 14 Gyr, from top to bottom) superimposed in red. The adopted distance modulus and metallicity are also labelled. The mean errors in magnitude and colour are reported on the left for each magnitude-wide bin.

suggestive of a coherent and recent episode of star formation, than a population of BSSs.

The next step therefore is the dating of the two subpopulations of Liller 1, which also requires the knowledge of their metallicity. Here we adopted a provisional global metallicity of [M/H] $= -0.3$ dex (corresponding to [Fe/H] $= -0.3$ dex with no $\alpha$-enhancement, or, e.g., [Fe/H] $= -0.4$ dex and $[\alpha/\mathrm{Fe}] \sim +0.2$ dex) for the bulk population of Liller1. This assumption is based on IR spectroscopy of a few bright giants only (Origlia et al. 2002).

By adopting PARSEC isochrones with ages between 10 to 14 Gyr, we found that the RGB colour and the magnitude level of the Red Clump of the OP are best reproduced with $E(B-V) = 4.52 \pm 0.10$ (which is larger than previous estimates, see Section 2.1.4) and a distance modulus $\mu_0 = 14.65 \pm 0.15$ (consistent with the latest determination from

Saracino et al. 2015). With these values, the morphology of the MS-TO and SGB provides a best-fit age of $t = 12 \pm 1.5$ Gyr for the OP. Specifically, we first selected the portion of the CMD that is most sensitive to age variations: the SGB and the MS-TO region. Thus, stars tracing the OP have been selected in the $(I, I-K)_{\rm DRC}$ CMDs at $23.5 < I_{\rm DRC} < 25.3$, and isochrones of different ages have been over-plotted adopting the quoted values of metallicity and distance modulus (see Figure 2.9). For each isochrone we performed a $\chi^2$ analysis. The $\chi^2$ parameter has been computed by comparing the colour of each star to that of the isochrone at the same magnitude:

$$\chi^2 = \sum_{j=1}^{N_*} \frac{(IK_{\rm obs,j} - IK_{\rm iso,j})^2}{IK_{\rm iso,j}} \tag{2.4}$$

where $IK_{\rm obs,j}$ is the observed colour of star j, $IK_{\rm iso,j}$ is the corresponding value of the colour read along the isochrones. By plotting the $\chi^2$ values obtained for isochrones of different ages, we found a well-defined minimum in correspondence of the 12 Gyr old isochrone. The analysis indicates an uncertainty of $\pm 1$ Gyr. By taking into account also the uncertainties in the reddening and distance modulus, we finally adopted conservative estimate of $12 \pm 1.5$ Gyr. This finding confirms that Liller 1 harbours a very old stellar component, formed during the remote epoch of the Milky Way formation.

The accurate dating of the BP population is a much more difficult task. In fact, from the analysis of the CMD, it is evident that significantly younger isochrones are needed to reproduce the BP, but no metallicity measurements for stars along this sequence are available at the moment. While the simpler assumption is to adopt the OP metallicity also for the BP, a self-enrichment scenario would predict an increased metal content for the younger population. We thus explored the following two reference scenarios: (1) the stars in the two subpopulations (BP and OP) share the same metallicity ([M/H] $= -0.3$), and (2) the BP is more metal-rich than the OP, with iron and $\alpha$-element abundances consistent with those observed in Terzan 5 ([Fe/H] $= +0.3$ dex and $[\alpha/{\rm Fe}] = 0$ dex, Origlia et al. 2011; Massari et al. 2014). Figure 2.10 a summarizes the results. For illustrative purposes, three isochrones (of 1, 2 and 3 Gyr) are superimposed on the CMD, by assuming the OP metallicity (left panel), and a supersolar Terzan 5-like iron content (right panel). As can be seen, the brightest portion of the BP turns out to be much better reproduced by the supersolar, 1 Gyr old isochrone. In any case, independently of the exact value of the metal content, both scenarios show that the distribution of stars observed in the BP requires the presence of a population as young as 1 Gyr. While the presence of a centrally segregated young population (see Figure 2.8 b) is hard to explain in a scenario where Liller 1 comes from the merger of two star clusters (which is strongly disfavoured also by the fact that young and massive stellar systems are very rare in the Milky Way), it is well consistent with an auto-enrichment process, where a new generation of (more metal-rich) stars formed in the central regions of the system and possibly further sank toward the centre because of mass segregation (in fact, according to Harris 1996, the central relaxation time of Liller 1 is of the order of $10^6$ yr only and, according to their age, these stars should be a factor of 2-2.5 more massive than the MS-TO mass of the OP). Indeed, the preliminary comparison with synthetic CMDs (see Figure 2.10 b) indicates

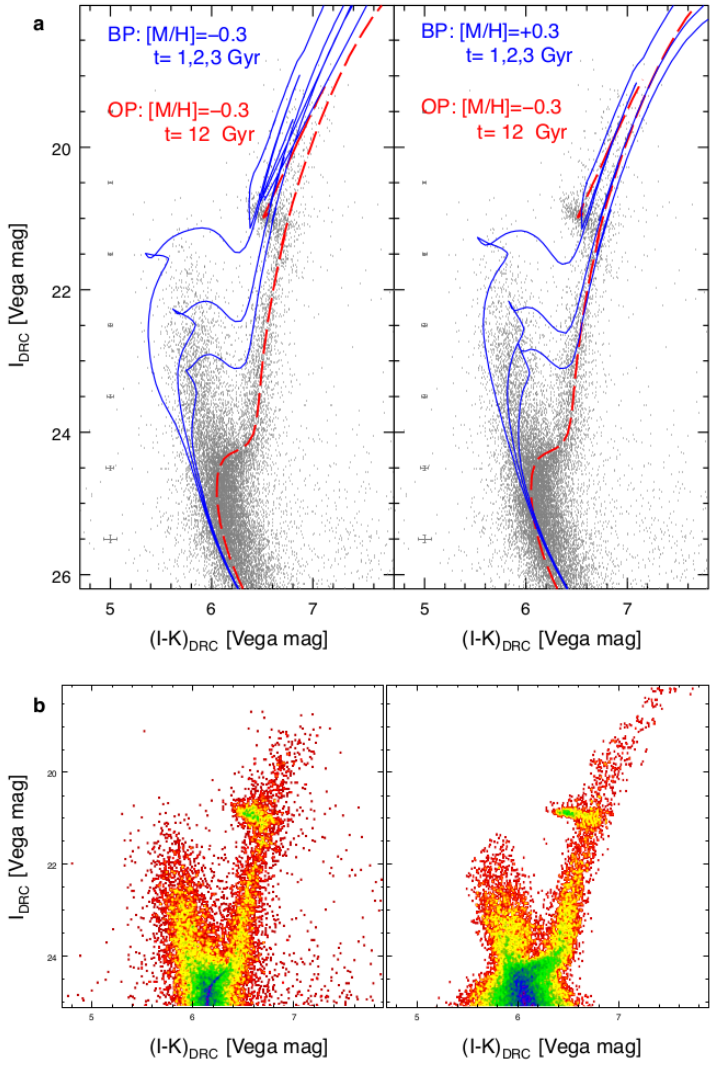


**Figure 2.10:** Panel (a): three young isochrones (of 1, 2 and 3 Gyr, solid blue lines from top to bottom) are overplotted to the CMD of Liller 1, where also the best-fit isochrone of the OP is shown (red dashed line). Since the metal content of the BP is currently unknown, for the sake of illustration, the isochrones have been calculated by assuming the same metallicity of the OP (left panel), [M/H] = −0.3 dex, and a significantly larger value, [M/H] = +0.3 dex (right panel). The mean errors are reported. Panel (b): Comparison between the CMD of the PM-selected members of Liller 1 (left) and a synthetic CMD (right) obtained by combining a 12 Gyr old stellar population with a set of young populations with ages in the range 1-3 Gyr. The stellar density in the CMD is colour-coded as follows: from blue, to green, yellow and red, for decreasing density

that the observed BP is accurately reproduced in a self-enrichment scenario, with a second star formation burst starting $\sim 3$ Gyr ago and lasting until 1 Gyr ago[8].

[8]We refer to Section 3.3 for a complete and detailed analysis of the star formation history of Liller 1 by means of synthetic CMDs

## 2.2 New photometry of Terzan 5 exploiting infrared and optical data

### 2.2.1 Observations and data reduction

As shown in Section 2.1.1, the combination of high-resolution IR and optical photometric data is a powerful choice for analyzing the stellar population of heavily extincted bulge stellar systems like Terzan 5 and Liller 1. The data set employed in this analysis is a combination of archival images covering both optical and IR bands. Specifically, the IR images were acquired with the Multi-conjugate Adaptive Optic Demonstrator (MAD) at the ESO/VLT (Science Demonstration Proposal, PI: Ferraro). The adaptive optics correction enabled to obtain images near to the diffraction limit, with a spatial resolution of $0.02''\text{pixel}^{-1}$. This data set is composed of 15 exposures in the $K$-band[9] centered on the cluster, with a dither pattern resulting in a final FOV of $1' \times 1'$ (Figure 2.11). The IR images are a subsample of a larger data set, selected on the basis of the seeing quality (with a stable FWHM in the $K$-band of $0.1''$ across the entire MAD FOV). The integration time of each exposure is $t_{exp} = 120\,\text{s}$. The optical images consist of 10 exposures in the filters F606W ($V$) and F814W ($I$) acquired with the ACS/WFC on board on HST, secured through the proposal GO 12933 (PI: Ferraro). All the exposures are $t_{exp} = 365\,\text{s}$ long.

The aforementioned database was already utilized in previous photometric studies. Specifically, the optical set of images was employed by Massari et al. (2015) to measure the PMs of stars included in the ACS/WFC FOV; while the IR ones, in combination with a large collection of HST images, was used in the work of Ferraro et al. (2016) to clearly detect for the first time the presence of a double MS-TO in the CMD of Terzan 5 (see Figure 1.9). However, the result of Ferraro et al. (2016) is limited to the small fraction of stars lying on the least extincted portion of the MAD field of view[10], with an additional strict selection applied to the photometric parameters related to the quality of the reduction (photometric error, $\chi$ and sharpness). Therefore, following the same strategy adopted in the case if Liller 1, we reanalyzed the photometric data set in order to increase the statistics, the photometric accuracy and depth.

The photometric reduction was performed through PSF fitting by using the software `DAOPHOTIV` (Stetson, 1987). First, PSF models were determined via the `DAOPHOTIV/PSF` routine for each exposure, selecting $\sim 200$ isolated, bright and not saturated stars homogeneously distributed across the entire FOVs. The analytical PSF functions were complemented by a spatially variable lookup table, following a cubic polynomial spatial variation. We applied the best PSF models to all the sources corresponding to flux peaks at least $3\sigma$ above the local background by using the `ALLSTAR` routine.

Differently from previous photometric analyses of Terzan 5, these first catalogs of instrumental magnitudes and positions were combined together, generating an input master list for `DAOPHOT/ALLFRAME` (Stetson, 1994) which includes the information coming from both optical and IR images. Specifically, the master list was created considering the

[9] As adopted in Section 2.1.1, we refer to the filters F606W, F814W and $K_s$ with the labels $V$, $I$ and $K$ respectively.

[10] Following the differential extinction map built in Massari et al. (2012)

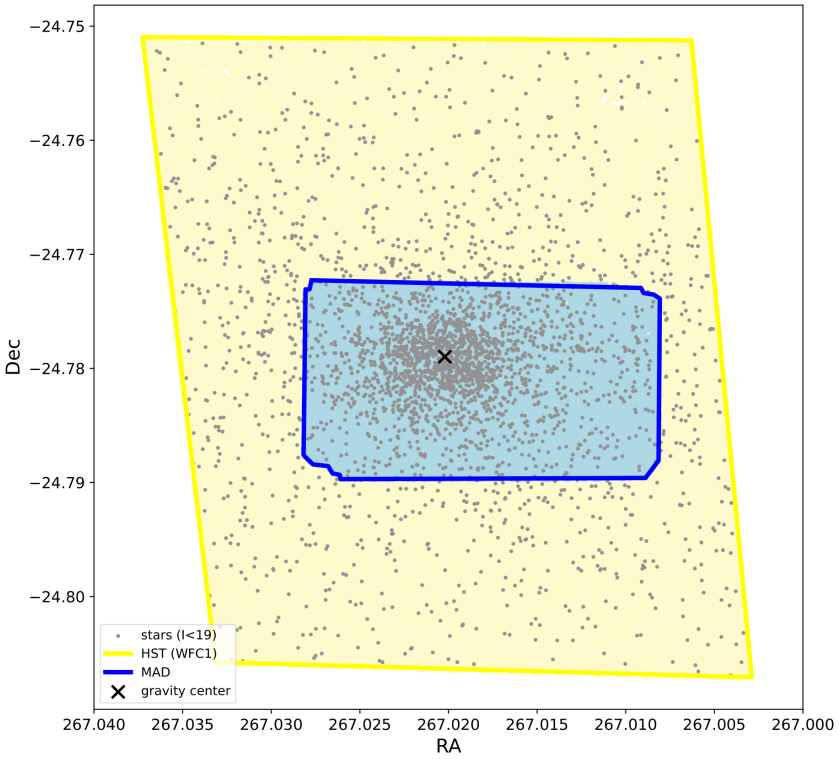


**Figure 2.11:** Field of view sampled by the observations: in yellow all the stars within the rectangular area of $\sim 200'' \times 100''$ covered by chip1 of the ACS/WFC data set, outlined in blue the objects detected within the $\sim 60'' \times 60''$ region corresponding to the MAD observations. For reference, we also show the position of bright stars with $I < 19$ (gray dots) and the gravity center of Terzan 5 (black cross; Lanzoni et al. 2010).

sources detected in more than five images in the $K$ filter, and in more than three images in at least one of the optical ones. The strength of this analysis is that stars detected only in the optical images were then searched and analyzed also in the $K$ images (and vice versa), because the routine `ALLFRAME` forces a fit at the corresponding positions of stars in the master list. The information provided by the two filters separately is thus maximized, with fruitful results in terms of photometric accuracy and statistics (as successfully done in the case of Liller 1, see Section 2.1.1).

The final raw magnitude for each recovered star, in a specific filter, is the weighted mean of multiple magnitude estimates (one for each exposure) once homogenized via `DAOMATCH` and `DAOMASTER`, while the photometric error is the corresponding standard deviation. The final catalog includes 30,834[11] objects that have both $I$ and $K$ magnitudes. Therefore, it is limited to the overlapping region between the ACS/WFC and MAD field of view (see the blue area in Figure 2.11).

We calibrated the optical instrumental magnitudes into the HST VEGAMAG system by applying the recipes and time-dependent ACS zero points provided by the STScI web interface[12]. Aperture corrections were determined with respect to a radius of 8 pixel,

[11] For comparison, the previous photometric catalog from Ferraro et al. (2016) counts $\sim 20,000$ stars within the same FOV.

[12] https://www.stsci.edu/hst/instrumentation/acs

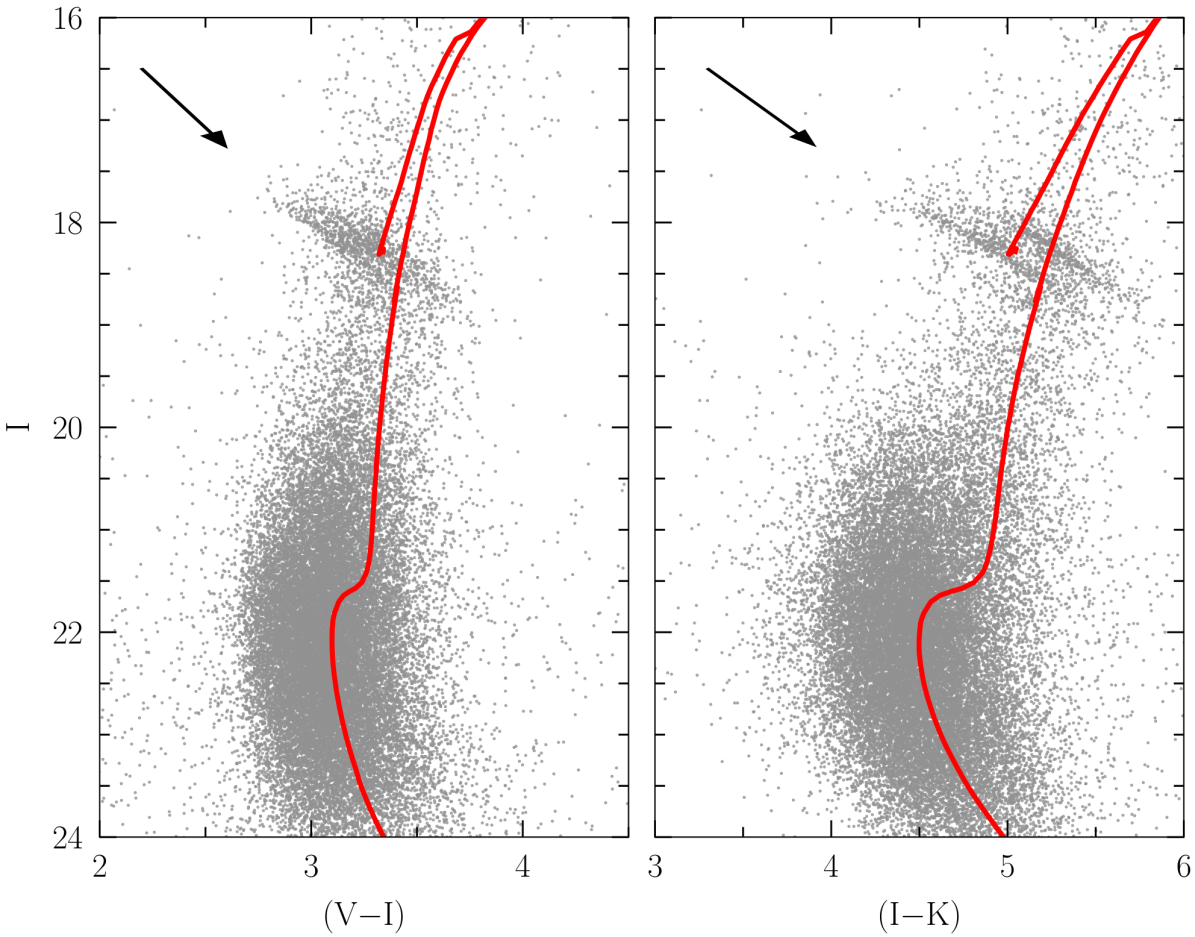


**Figure 2.12:** Optical $(I, V-I)$ and hybrid $(I, I-K)$ CMDs of Terzan 5 obtained through the combined HST and MAD observations, corresponding to the FOV delimited by the blue box in Figure 2.11. No quality cuts and DRC corrections are applied to these diagrams. It is worth noticing the distortion of the evolutionary sequences (especially the two RCs) along the reddening vectors, displayed by the black arrows in the upper-left part of the panels. The red line corresponds to a 12 Gyr old isochrone (Bressan et al. 2012) with [M/H] $= -0.2$ dex, $E(B-V) = 2.38$, and $\mu_0 = 13.87$.

selecting a subsample of bright and isolated stars across the FOV, and referring to the value of Encircle Energy tabulated in the HST website. The IR raw magnitudes were calibrated onto the 2MASS photometric system by computing the offset of the common stars between our catalog and the public available VISTA Variables in the Vía Láctea (VVV) survey (Minniti et al., 2010). Among the stars in common, we kept the ones with low photometric error ($\sigma_K < 0.075$), and we adopted as zero-point the median of the difference after a $3\sigma$ rejection. The resulting CMDs, both in optical and hybrid $(I, I-K)$ set of filters, are shown in Figure 2.12. The distributions of photometric errors and `DAOPHOT` parameters $\chi$ and sharpness, which are related to the quality of the PSF fitting, are displayed in Figure 2.13, and they will be used to clean the CMDs from spurious objects or badly fitted stars.

We corrected the instrumental coordinates for the ACS/WFC geometric distortions following the prescription of Anderson & Bedin (2010), and subsequently we cross-matched

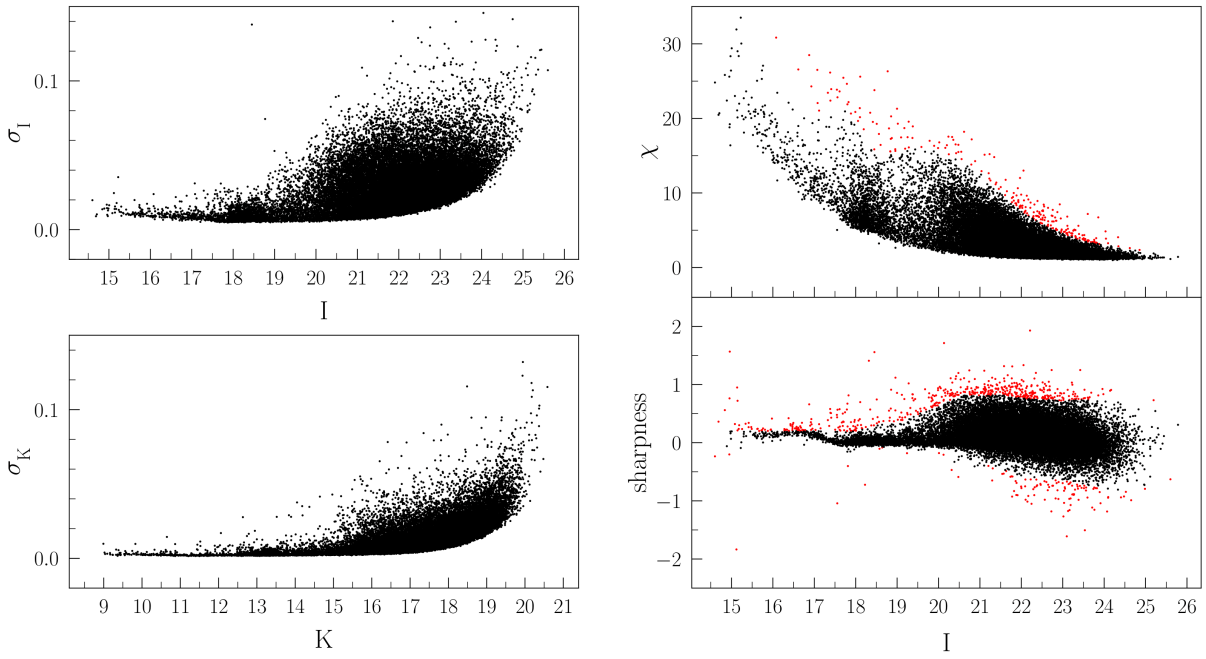


**Figure 2.13:** *Left panels:* Trends of the photometric error as computed by DAOPHOT as a function of I and $K$ magnitude. *Right panels:* Photometric quality parameters $\chi$ and *sharpness* resulting from the combined optical-IR reduction. Red points are stars excluded by the $3\sigma$ clipping procedure.

our catalog with the one from Ferraro et al. (2016) to retrieve HST ACS/WFC based high-resolution PMs calculated by Massari et al. (2015) and absolute coordinates $(\alpha, \delta)$ based on the astrometric 2MASS catalog.

### 2.2.2 New high-resolution reddening map in the direction of Terzan 5

The effect of the high degree of heterogeneity of the interstellar medium across the observed FOV is clearly visible in Figure 2.12, where all the evolutionary sequences of the CMD result blurred and elongated along a precise direction given by the *reddening vector*[13] (see the black arrows in Figure 2.12). Given the high extinction in the direction of Terzan 5 and its location within the Galaxy ($E(B-V) = 2.38$; $l, b = 3.81°, 1.67°$; Valenti et al. 2007), this problem is exacerbated, and the correction for differential reddening effects becomes a crucial step in the identification and characterization of its subpopulations (as demonstrated in the case of Liller 1, see Section 2.1.5). Hence, we decided to build a new high-resolution differential reddening map in the direction of Terzan 5, aiming at reaching the arcsecond scale. Indeed, the study of Ferraro et al. (2016) was based on the differential extinction map presented in Massari et al. (2012), which reached a spatial resolution of $8'' \times 8''$. This resolution provided an overall good correction for differential reddening effects, but it led the detection of a double MS-TO only selecting the least extincted region of the MAD FOV, that corresponds to an area of $\sim 25'' \times 25''$ in the south-west direction.

It has been extensively shown that, when constructing differential reddening maps of stellar clusters, techniques based on the so-called *star-by-star method* can provide maps

[13]Specifically for the hybrid CMD, the components of the reddening vector are $V_x = A_I - A_K$; $V_y = A_I$.

with a spatial scale of few arcseconds (see Section 2.1.4). Thanks to the improved statistics and photometric accuracy, we could model the differential reddening in the field of view covered by our observations with this novel approach, following the guidelines provided in several recent papers (e.g., Saracino et al. 2019; Pallanca et al. 2019; Cadelano et al. 2020) that we successfully tested in Section 2.1.4.

### The star-by-star reddening correction

The star-by-star method estimates the differential reddening of each star in the catalog by computing the shift, along the reddening vector, needed to minimize the residuals between the mean ridge line (MRL) of the cluster and the "local" CMD. The latter is defined as the CMD built with the spatially closest objects to the targeted star. We extensively described the theory behind this method in Section 2.1.4. Here we applied the same strategy to the cluster Terzan 5.

First of all, as done for Liller 1, we checked which value of $R_V$ is suitable for this case of study. In fact, it was recently shown that the coefficient $R_V$ can change depending on the observed region of the Milky Way, especially in the direction of the bulge (see, for example, Nataf et al. 2013, Pallanca et al. 2021b, Legnardi et al. 2023). A powerful tool to discriminate the value of $R_V$ for the specific case of study is to simultaneously employ a set of optical and IR filters, as shown in Section 2.1.4. As explained in the mentioned section, changing the value of $R_V$ makes the extinction law more or less steeply dependent on the wavelength, especially in the optical regime. Therefore, we checked if the classical assumption $R_V = 3.1$ is a reasonable choice for the case of Terzan 5. To this aim, we computed an isochrone (Marigo et al. 2017) with age t = 12 Gyr (Ferraro et al. 2016) and global metallicity [M/H] $= -0.2$ dex (Valenti et al. 2007, Massari et al. 2014), and we checked if it simultaneously matches the observed optical and hybrid CMDs, assuming the value of $R_V = 3.1$ to redden it[14]. As shown in Figure 2.12, the isochrone nicely reproduces the evolutionary sequences of the cluster both in the optical and hybrid plane. Therefore, we adopted the extinction coefficients calculated considering $R_V = 3.1$, the extinction law from O'Donnell (1994), and effective wavelengths of the F814W and $K$ filters tabulated in Rodrigo & Solano (2020)[15]. Under these assumptions, the extinction coefficients are $A_I = 1.90$ and $A_K = 0.36$.

We then proceed to estimate the reddening of each stars of the catalog, following the same procedure as in Section 2.1.4, which is also widely explained in Pallanca et al. (2021b). The corrections were computed in the PMs cleaned and hybrid $(I, I-K)$ CMD. Briefly, we first determine the mean ridge line that approximates the upper MS, SGB and RGB of the old (and more populated) stellar component of Terzan 5. To do so, we divided the CMD in different magnitude bins adapting the bin size to the evolutionary sequence (from 0.2 to 1 mag). We calculated the mean values of color and magnitude of each bin by considering only a subsample of high-quality and PMs selected stars, chosen through a $3\sigma$ rejection applied to the distributions of $\chi$ and sharpness (see black points in Figure 2.13). We then determined the value of differential reddening $\delta E(B-V)$ for

[14] We also considered $E(B-V) = 2.38$ and $\mu_0 = 13.87$ from Valenti et al. (2007).

[15] $\lambda_{eff,\mathrm{F814W}} = 7973.39$ Å ; $\lambda_{eff,\mathrm{K}} = 21590$ Å

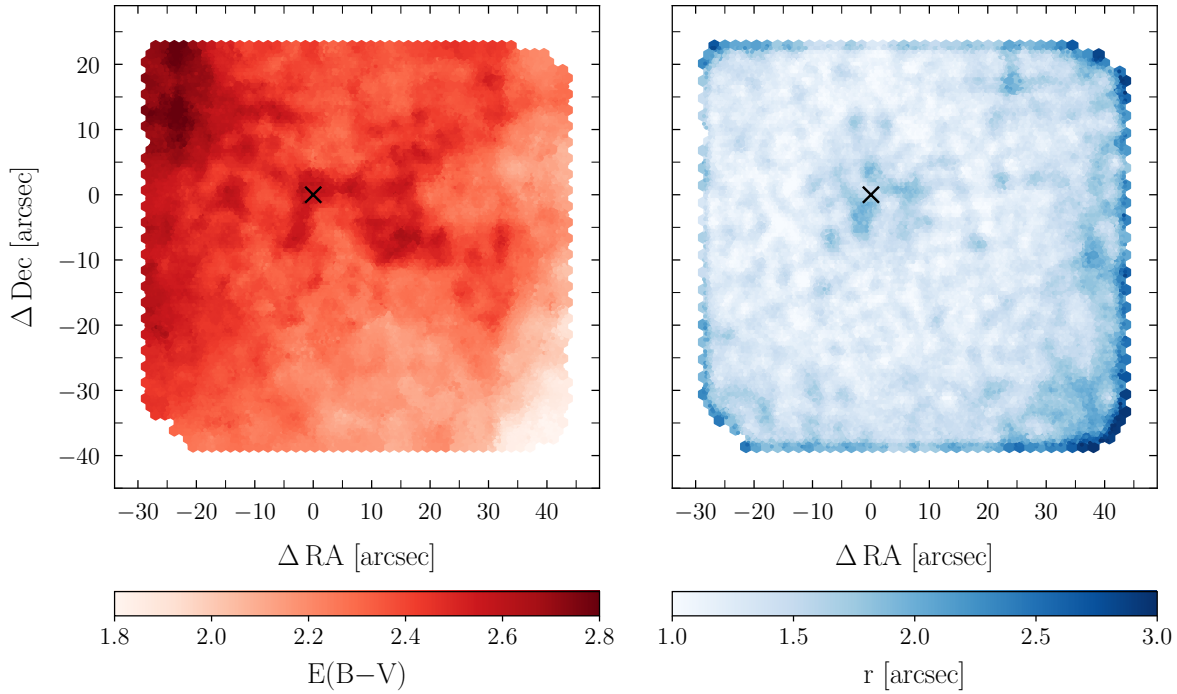


**Figure 2.14:** *Left panel:* map of the absolute reddening $E(B-V)$ in the direction of Terzan 5. Darker colors indicate the more extincted areas within the observed FOV (see the black box in Figure **??** FOV). The black cross marks the gravity center of Terzan 5 (Lanzoni et al. 2010). North is up, while east is on the left. *Right panel:* map of the radial distances used to select the samples of nearby high-quality sources for the construction of the *local CMD* of every star in the photometric catalog. Lighter (darker) colors are associated to regions with higher (lower) reached spatial resolution.

all the stars. Specifically, for each stars of the catalog, we first built the local CMD by considering the closest $N_\star$ (usually 30) stars from the high-quality pool. However, we also set a maximum radial distance of $r = 3''$, imposing that one of the two conditions should hold. Subsequently, the MRL is shifted along the direction of the reddening vector in steps of $\delta E(B-V)$, until it fits the local CMD. The value of reddening that minimize the distance between the MRL and the local CMD is found by following the Equation 2.2.

The resulting absolute differential reddening map in the direction of Terzan 5 (assuming the average color excess estimated in Valenti et al. 2007) is shown in the left panel of Figure 2.14. For construction, this map has a spatial resolution smaller than $3''$, as visible in the right panel of Figure 2.14, where we show the distribution of the radial distances used to select high-quality stars for constructing the local CMDs. It is worth noticing that, despite the small area covered by the IR camera ($60'' \times 60''$), the maximum variation of $E(B-V)$ across the FOV is $\sim 1$ mag, demonstrating that it is necessary to properly model the patchy absorption pattern of the dust clouds on small arcsecond scales. Indeed, the differential extinction map from Massari et al. (2012), built which a larger cell size ($8'' \times 8''$), quoted an extinction variation of $\delta E(B-V) \sim 0.67$ mag.

The benefit from both the new differential reddening corrections and photometric analysis is particularly evident in Figure 2.15, where we compare the new (upper panel) and the old (lower panel) CMD of Terzan 5, including stars across the entire IR field of

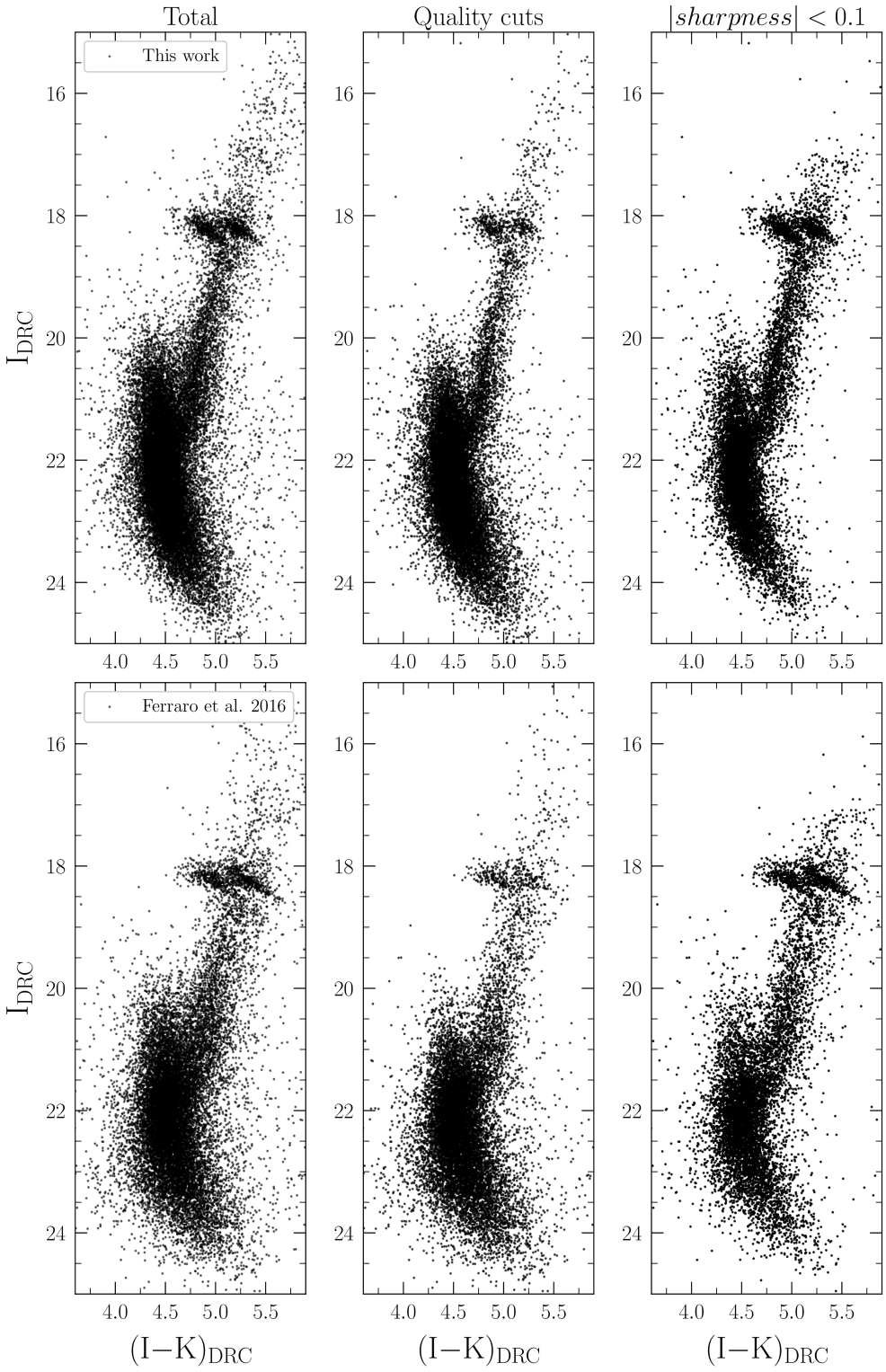


**Figure 2.15:** Comparison between the hybrid $(I, I-K)$ and PM-cleaned CMD of Terzan 5 obtained through this novel photometric reduction and differential reddening correction (upper panels), and the study of Ferraro et al. (2016) with the differential reddening correction from Massari et al. (2012) (lower panels). The first, second and third column display, respectively, the total sample of stars in the two catalogs, the subsample of stars with good values of $\chi$ and *sharpness* (black points in Figure 2.13), and absolute *sharpness* value lower than 0.1.

view. The CMDs displayed in Figure 2.15 are made of only member stars according to their PMs (Massari et al. 2015, see also the rightmost panel of Figure 3.15): we show in the first column all the cluster's stars; in the second column a subsample obtained through quality cuts, that is stars beyond the first 15″ from the center (to avoid the most crowded region) and within $3\sigma$ in the *sharpness* and $\chi$ parameter distributions (black points in Figure 2.13); finally, in the third column, we retained only stars with an absolute value of *sharpness* less than 0.1. This strict cut in the *sharpness* distribution is meant to exclude all possible blends or spurious objects, such as cosmic rays and foreground galaxies, allowing to better visually detect all the subpopulations of Terzan 5. As appreciable from all the panels, the new photometric reduction resulted in a deeper CMD, lower photometric errors, and a higher number of detected objects; while the new differential reddening map revealed a clear blue plume (at $4.2 < (I-K)_{\rm DRC} < 4.8$) and likely younger MS-TOs (at $I_{\rm DRC} \sim 21$), which are features barely visible in the lower panels. We stress that the improved statistics and photometric accuracy, i.e. the possibility to have a CMD showing the features descibed above, was a mandatory prerequisite to properly compare these two peculiar stellar systems, and, especially, it has been essential to the analysis presented in the next chapter (see Chapter 3).

## 2.3 Liller 1 and Terzan 5: differences and similarities

The results presented in Section 2.1.5 clearly classify Liller 1 as a non-genuine GC, and collocate it in the class of GC-like structures in the Galactic bulge harbouring multi-age stellar components, which was initiated by the discovery of the complex stellar populations in Terzan 5. Therefore, the comparison of the stellar populations in these two stellar systems is quite instructive. In Figure 2.16, their CMDs have been aligned by requiring that the faintest RC of Terzan 5 matches that of Liller 1. The comparison shows both gross differences and some relevant similarities in the properties of the stellar populations in these two systems.

The main difference between the two CMDs concerns the morphology of the young population. In Terzan 5 the major manifestation of this component is the presence of a RC brighter and redder than that of the old population. In Liller 1 no relevant features are detected in the evolved portion of the CMD and the young population manifests its own presence in the form of an extended MS, suggesting a quite recent burst of star formation (occurred $\sim 1-3$ Gyr ago). The post-MS evolutionary timescale of such young stellar population is so fast that no relevant features are expected to be observable in the evolved portion of the CMD, apart from the RC. Theoretical isochrones (Bressan et al. 2012; Marigo et al. 2017) indicate that the RCs of the young and old components overlap in the CMD (see Figure 2.10 a), and should therefore be indistinguishable in the diagram. However, the existence of the BP should produce a numerical excess with respect to the amount of RC stars expected if only the OP was present, that is confirmed by star number counts. In order to estimate the expected number of RC stars belonging to the OP, we used the number of objects counted at the base of the RGB ($15 < K_{\rm DRC} < 17$), where negligible contribution from the young component is expected because of the fast evolutionary time

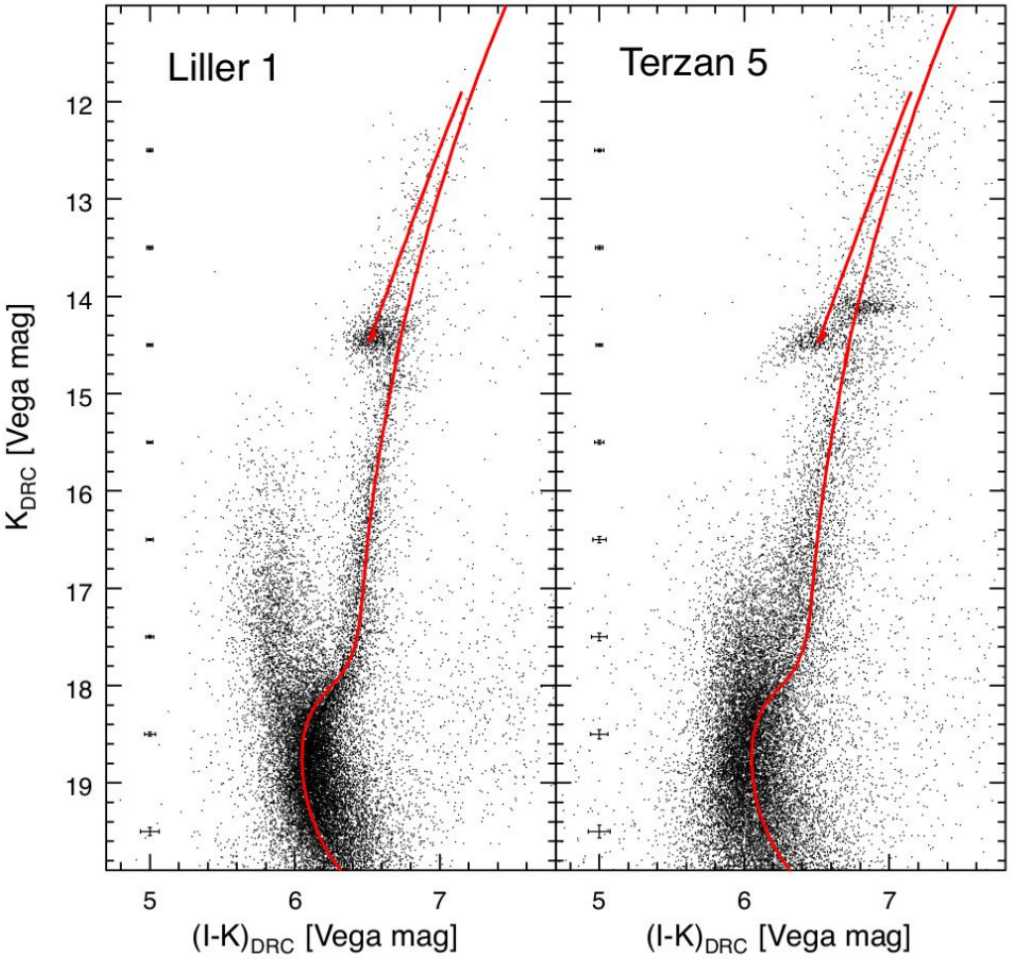


**Figure 2.16:** *Left panel:* CMD of Liller 1 with the isochrone used to estimate the age of its OP ($t = 12$ Gyr and [M/H] $= -0.3$ dex) superposed as a red line. *Right panel:* CMD of Terzan 5 shifted in magnitude and color to make its old (faintest) RC match the RC of Liller 1, with the same isochrone shown in panel a superposed in red. The photometric errors are reported on the left.

of this phase at such small ages. Theoretical tracks for stars of $0.9\,M_{\odot}$ (as appropriate for OP objects) indicates that the ratio between the evolutionary times in the RC and in this RGB magnitude range is approximately $t_{RC}/t_{RGB} = 0.9 \times 108/3.04 \times 108 = 0.3$. Hence, since the completeness-corrected counts of RGB stars in the adopted magnitude range are 1175, we expect $\sim 352$ RC objects. By conservatively considering an additional 30%, due to the fact that RGB stars lying adjacent to the RC region appear indistinguishable from RC objects in the CMD, we expect a total of $\sim 457$ stars belonging to the OP population in the RC region. We observe, instead, 765 stars. This clearly indicates that the young population is significantly contributing to the observed number counts, and suggests that the fraction of the young component, with respect to the total mass of Liller 1, can be as large as 40%, although detailed simulations are required to firmly assess this estimate.

The comparison of the two CMDs also shows a striking similarity between the two old stellar populations. Indeed, if the RCs of the two systems are aligned, also their RGB–bumps, SGBs and the MS-TO points appear to be at the same magnitude levels.

In other words, the old populations in the two stellar systems are strikingly similar and they are reproduced by the same isochrone (with $t = 12\,\mathrm{Gyr}$ and $[\mathrm{M/H}] = -0.3\,\mathrm{dex}$). This finding suggests that both stellar systems formed at the epoch of the Galaxy formation ($\sim 1\,\mathrm{Gyr}$ after the Big-Bang), from gas clouds with similar chemistry. The detailed study of the $\alpha$-element abundance patterns of the OP in Liller 1 is needed to confirm this hypothesis.

## 2.4 Summary

The challenging environmental condition (in terms of extreme dust extinction and field contamination) affecting the bulge region hosting Terzan 5 and Liller 1 had been hampering for a long time the proper photometric study of these two remarkably peculiar stellar systems. Here, we performed PSF fitting on high-resolution optical (HST-ACS/WFC) and IR adaptive optics assisted (GeMS/Gemini and MAD/VLT) images, combining the complementary information coming from the two set of filters to built the cleanest, deepest and most accurate CMDs ever obtained for Liller 1 and Terzan 5. This combination of data sets also allowed to exploit the valuable wavelength baseline and numerical statistics for building differential extinction maps with the highest spatial resolution ever reached. Thanks to this analysis, we detected, for the first time, a conspicuous fraction of young stars belonging to Liller 1.

The analysis of the CMD of Liller 1, and the comparison with different sets of isochrones, suggest that the BP is made of stars not only with an age of just 1-3 Gyr, but probably also with a higher metallicity than the OP (see the isochrones plotted in Figure 2.10). This finding unquestionably demonstrates that Liller 1 is not a GC: it is a stellar system characterized by a much more complex star formation history that gave rise to younger stellar populations. This is the second case (after Terzan 5; Ferraro et al., 2009, 2016) of a GC-like system in the Galactic bulge showing these peculiarities. The presence of young stellar populations in Terzan 5 is now even more visible in the new CMD (upper panels of Figure 2.15), constituting an important basis for a more detailed investigation of its stellar subcomponents.

As shown in Section 2.1.4 and 2.2.2, the correct evaluation of the reddening map in the direction of these highly obscured stellar systems is a crucial requirement to probe their stellar populations and reconstruct their star formation histories (see Chapter 3). Moreover, we underline that, as in the case of Liller 1, it is possible to measure in the Galactic bulge values of $R_V$ that deviate from the canonical 3.1.

To summarize, the analysis reported in this chapter allowed us to detect in Terzan 5 and Liller 1 all the main features that are expected from the Bulge Fossil Fragments scenario. Specifically: (1) they are indistinguishable from massive genuine GCs in their appearance; (2) they have (photometric) metallicity and abundance patterns compatible with those observed in the bulge field stars; (3) they host an old stellar population, testifying that they formed at an early epoch of the Galaxy assembling; (4) they host a young stellar population, several to many Gyrs younger than the old one, testifying their capacity of triggering multiple events of star formation.

This chapter is based on the results presented in
Ferraro, Pallanca, Lanzoni, Crociati et al. (2021)
Pallanca, Ferraro, Lanzoni, Crociati et al. (2021)
Crociati et al. (2024, in prep.)

# 3 The Star Formation Histories of Liller 1 and Terzan 5

## 3.1 The star formation history as a key piece of information

Among the vast population of Galactic stellar aggregates traditionally classified as globular clusters, three systems, namely Terzan 5, Liller 1 and $\omega$ Centauri, stand out for their significantly peculiar properties. With masses larger than some $10^6 M_\odot$, these objects are among the most massive cluster-like systems in the Galaxy. More importantly, they are the only ones hosting multiple populations characterized by both significant iron and age spreads ($\sim 1$ dex and up to $5-8$ Gyr respectively - e.g., Norris et al. 1996; Lee et al. 1999; Pancino et al. 2000; Ferraro et al. 2009, 2021).

$\omega$ Centauri is a metal-poor (average metallicity [Fe/H] $\sim -1.5$ dex) system orbiting the Galactic halo and hosting at least 4-5 discrete populations, as revealed by a large number of detailed photometric and spectroscopic analyses (e.g., Norris et al. 1996; Lee et al. 1999; Pancino et al. 2000; Ferraro et al. 2004; Sollima et al. 2005; Bellini et al. 2009; Johnson & Pilachowski 2010). These populations span a wide metallicity range, going from [Fe/H]$\sim -2.2$ dex to $-0.5$ dex, and a possible age range of about $3-4$ Gyr. This evidence led to the early suggestion that $\omega$ Centauri is the remnant core of an accreted dwarf galaxy captured during its approach to the Milky Way (Zinnecker et al. 1988; Majewski et al. 2000). Indeed, more recently, thanks to the exquisite Gaia astrometry (Gaia Collaboration et al. 2021), $\omega$ Centauri has been associated with either Gaia-Enceladus or Sequoia (Massari et al. 2019), which are two of the most prominent accretion events experienced by the Galaxy.

On the contrary, both Terzan 5 and Liller 1 are suspected to be the result of a different and very peculiar formation process. All the evidence gathered so far (see Section 1.2.3) disfavor the possibility that Terzan 5 formed in a satellite galaxy later accreted by the Milky Way, and rather suggest that it is a genuine Galactic system, which formed and evolved in and with the bulge. These stellar systems could be interpreted as the surviving relics of much more massive primordial structures that generated or contributed to the Galactic bulge formation (Ferraro et al. 2009, 2016, 2021), similarly to the giant clumps observed in the star-forming regions of high-redshift galaxies (see Section 1.2). Terzan 5 and Liller 1 would therefore belong to a new class of stellar systems called Bulge Fossil Fragments (BFFs): these are stellar aggregates with the appearance of massive GCs orbiting the Galactic bulge, formed at the epoch of the Galaxy assembling, and harboring

in addition to the old population, a younger component (see Chapter 2).

An alternative formation scenario for Terzan 5 and Liller 1 has been recently proposed by Bastian & Pfeffer (2022). The authors argue that their peculiar properties might be the result of an interaction between an ancient massive stellar cluster and a giant molecular cloud (GMC) that took place a few Gyrs ago, thus forming the younger population observed in both systems. Based on the hydrodynamical simulations by McKenzie & Bekki (2018), they suggest that, as a result of such interaction, the massive cluster may be able to accrete gas from the GMC and eventually experience a new event of star formation. In this scenario, the probability of encounters between clusters and GMCs increases for massive systems on disky orbits, as in the case of Liller 1 and Terzan 5, but in general it remains pretty low. As these are rare events, only an handful of systems is expected to undergo this formation process within a Hubble time. In addition, because of their rarity, the star formation history (SFH) of stellar systems forming this way is expected to exhibit at most two discrete star-formation episodes.

Therefore, in this ongoing and exciting discussion about the physical processes behind the formation of Terzan 5 and Liller 1, constraining the detailed SFHs of their stellar populations represents an important piece of information. Driven by this motivation, we undertook a detailed analysis of their CMDs using a synthetic CMD approach[16] aimed at deriving and analyzing the SFHs of such complex stellar systems.

## 3.2 The synthetic color-magnitude diagram method

In the study of the SFH of stellar systems, a huge amount of information about the stellar populations and their histories can be derived from the detailed analysis of the observed CMD, once a deep and accurate photometry is achieved. Indeed, all the key characteristics of a stellar population are enclosed in the CMD: age, mass, metallicity, IMF and SFR. A successful and widely used method for recovering the SFH of resolved galaxies is the so-called synthetic CMD method (e.g., Tosi et al. 1991; Tolstoy & Saha 1996; Dolphin 1997, 2002; Hernandez et al. 1999; Cignoni & Tosi 2010; Aparicio & Hidalgo 2009; Weisz et al. 2012; Ruiz-Lara et al. 2018). This method is based on the comparison between the observed CMD and a set of simulated (or *synthetic*) ones, generated from theoretical isochrones.

Once collected a wide library of stellar models, with a fine binning both in age and metallicity, the first step is to built a repository of "basic" synthetic CMDs, or *basis functions* (BFs). Indeed, any observed CMD can be reproduced by a linear combination of BFs, since each BFs can be considered as a burst of star formation with a duration $\Delta t$ (centered at the time step $j$) and a $\Delta Z$ (centered at the metallicity step $k$). The BFs are populated following a Monte Carlo procedure, once the parameters of the stellar population (IMF, binary fraction, distance modulus, reddening and metallicity) are constrained. First, couples of synthetic masses and ages (i.e. synthetic stars) are extracted from the assumed IMF to cover a uniform distribution of metallicity and star formation steps, and then converted to absolute magnitude and colors by using the library of

[16] In collaboration with Prof. Michele Cignoni of the Department of Physics, Pisa University.

isochrones. Based on the chosen binary fraction, a percentage of synthetic stars is coupled with a companion star, whose mass is extracted from the same IMF and whose flux is added to the primary one. Second, theoretical photometry (the "clean" BF) is degraded to match the observational characteristics of the data. This translates into including extinction and distance effects, and convolving the synthetic photometry with completeness and photometric errors/systematics. To ensure that all the evolutionary phases are well populated (i. e., to overcome the short duration of some evolutionary phases), the BFs are typically populated with a high number (of the order of $10^6$) of synthetic stars. Third, BFs and the observed CMD are binned in $n$ bins of color and $m$ bins of magnitude, constructing their density maps (Hess diagrams). The final result is a library of $j \times k$ 2D histograms ($\mathrm{BF}_{m,n}(j,k)$), whose elements can be linearly combined (Equation 3.1) to reproduce the observed CMD:

$$N_{n,m} = \sum_j \sum_k a(j,k) \times \mathrm{BF}_{m,n}(j,k) \tag{3.1}$$

The coefficients $a(j,k)$ are the weights of each $\mathrm{BF}_{m,n}(j,k)$, representing the SFR at the time step $j$ and metallicity step $k$. The sum over $j$ and $k$ of $a(j,k) \times \mathrm{BF}_{m,n}(j,k)$ provides the total star counts $N_{n,m}$ in the CMD bin $(m,n)$. The final step is to find the superimposition of BFs that best reproduces the observed CMD, minimizing the residuals between the model and the data.

### 3.2.1 The SFERA code

To construct synthetic CMDs, as well as statistically compare them to the observed one, we made use of the population synthesis routine Star Formation Evolution Recovery Algorithm (SFERA, Cignoni et al. 2015). The SFERA code requires in input the following parameters:

- library of stellar tracks/isochrones,
- IMF,
- binary fraction,
- metallicity, distance and foreground reddening range,
- limit age and $\Delta t$ intervals to calculate the BFs,
- CMD bin size.

The routine does not assume any age-metallicity relation a priori. The stellar models are populated through a Monte Carlo extraction of $10^6$ stars from a flat mass distribution, then weighted based on the assumed IMF. A star will be visible in the synthetic CMD according to its lifetime as read from the stellar model. Conversely, if a star is considered dead, it will only contribute to the total mass of the system. Subsequently, clean model CMDs are placed at the distance of the object, reddenened, and convolved with photometric errors and incompleteness. These observational uncertainties are quantified by means of

extensive *artificial stars experiments* (see Section 3.3.2 for details). To derive the SFH and identify the best-fit model, SFERA first constructs a Hess diagram for the observed data, and then attempts to match it by linearly combining Hess diagrams from the library of synthetic CMDs. The best-fit solution is found by minimizing the residuals between data and models following a Poissonian statistics. Specifically, SFERA searches the combination of BFs - which corresponds to the most likely SFH that generated the observed CMD - that minimizes the likelihood distance between models and data (Equation 3.2):

$$\chi^2_P = 2 \sum_{i=1}^{N_{bin}} e_i - o_i + o_i \ln \frac{o_i}{ei} \tag{3.2}$$

where $e_i$ and $o_i$ are, respectively, the expected and the observed number of stars contained in the $i$th cell of the binned CMD. The uncertainty on the best-fit solution is computed via data bootstrap and deriving the SFH using different age and CMD binnings.

To explore the wide parameter space resulting from the choice of age and metallicity steps, SFERA combines a genetic algorithm (GA) (Pikaia[17]) with a local search routine. On the one hand, the GA allows to explore the parameter space in more points simultaneously, being less sensitive to the initial conditions and local minima; on the other, the local search speeds up the convergence time and increases the accuracy of the solution (see Cignoni et al. 2015).

### 3.2.2 Input parameters

To derive the SFHs of Liller 1 and Terzan 5, we built the library of isochrones based on the latest PARSEC-COLIBRI stellar models (Bressan et al. 2012; Marigo et al. 2017). We downloaded a set of isochrones from the PARSEC webpage thanks to the python interface package `EZPADOVA`[18], covering an age range from 2 Myr to 13.4 Gyr, with a step of $\log(t/\mathrm{yr}) = 0.05$ dex, and a metallicity range from $[\mathrm{M/H}] = -2$ dex to $[\mathrm{M/H}] = +0.3$ dex[19], with a step of 0.025 dex. This metallicity range has been chosen to include the available metallicity derivations of Terzan 5 and Liller 1 (see Section 1.2.3, 1.3) and, at the same time, to secure a quite large tolerance for the iron abundance to vary. The isochrones were computed in the HST/ACS-WFC and 2MASS photometric systems, since these are the photometric bands used to build the observed CMDs. The basic synthetic CMDs are Monte Carlo realizations of all possible combinations of 14 equally spaced age bins, between the youngest and the oldest available isochrone. Within each age bin, a range of metallicities is allowed, from the lowest to the highest. A Kroupa (2001) IMF between 0.1 and 300 $M_\odot$ is then used to fully populate the synthetic CMDs. The adoption of other commonly used IMFs, such as Salpeter (1955) or Chabrier (2003) IMFs, is expected not to impact significantly the main results of the present analysis. In fact, the quoted IMFs do not differ significantly for stellar masses larger than $\sim 1\,M_\odot$, which is approximately the mass regime we focus on. Unresolved binaries are also considered and 30% of synthetic stars are

[17] This is a public available routine developed at the High Altitude Observatory.

[18] https://github.com/mfouesneau/ezpadova

[19] We adopt $[\mathrm{M/H}] = \log(Z/Z_\odot)$, with $Z_\odot = 0.0152$. We report also that $[\mathrm{M/H}] = [\mathrm{Fe/H}] + \log\left(0.638 \cdot 10^{[\alpha/\mathrm{Fe}]} + 0.362\right)$ from Salaris et al. (1993).

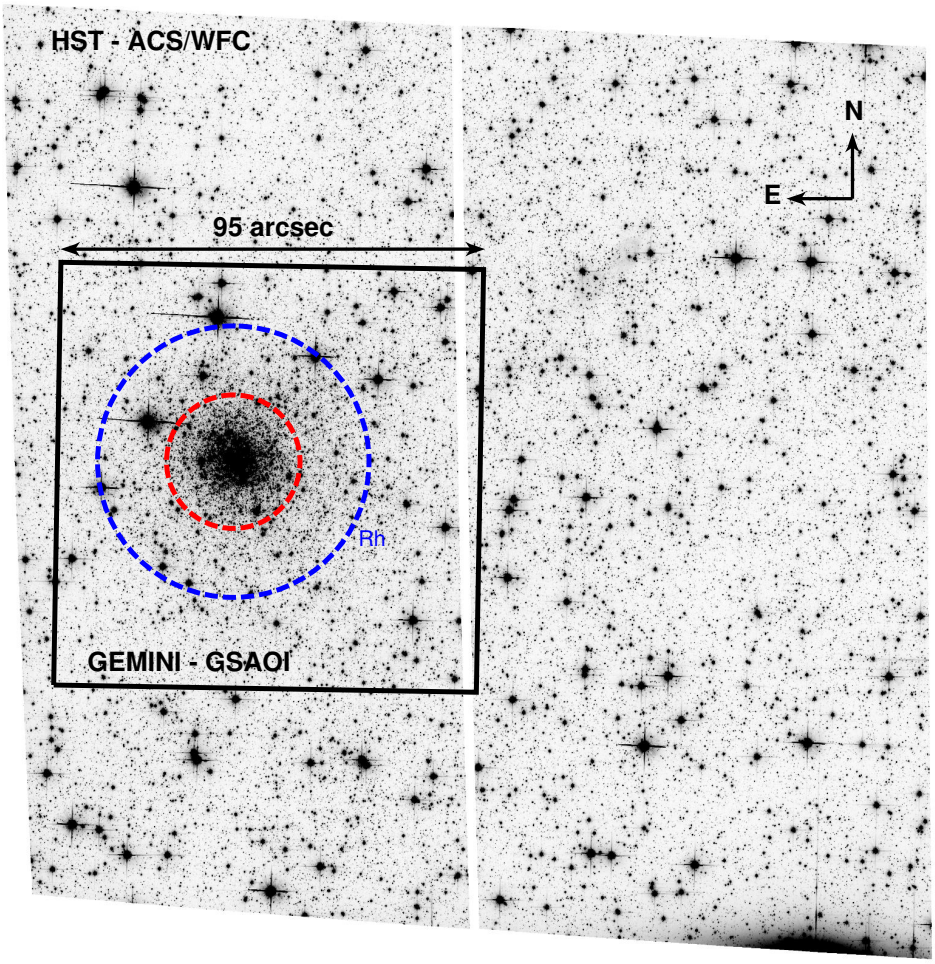


**Figure 3.1:** HST ACS/WFC image of Liller 1 in the F814W filter. The field of view is $204'' \times 204''$. The black box corresponds schematically to the GeMS-GSAOI pointing ($95'' \times 95''$). The region used for the SFH reconstruction is that beyond the red circle (having a radius of $15''$). The blue circle marks the half-mass radius of Liller 1 ($r_h = 30.5''$, from Saracino et al. 2015). North is up, east is to the left.

coupled with a stellar companion sampled from the same IMF. Distance and foreground extinction are also free parameters, whereas differential extinction is not considered as it has been corrected star by star as discussed above in the observations. The CMD bin size is chosen as a compromise between the photometric error, resolution of the selected stellar models, and computational time, ranging from 0.1 to 0.05 both in magnitude and color.

## 3.3 Clues to the formation of Liller 1 from its complex Star Formation History

In this Section we perform the very first attempt to reconstruct the SFH of these complex stellar systems by using Liller 1 as a test-bench. In fact, the available photometric data set for Liller 1 is less affected by incompleteness and the main sequence turn-off of the younger population is brighter than in Terzan 5.

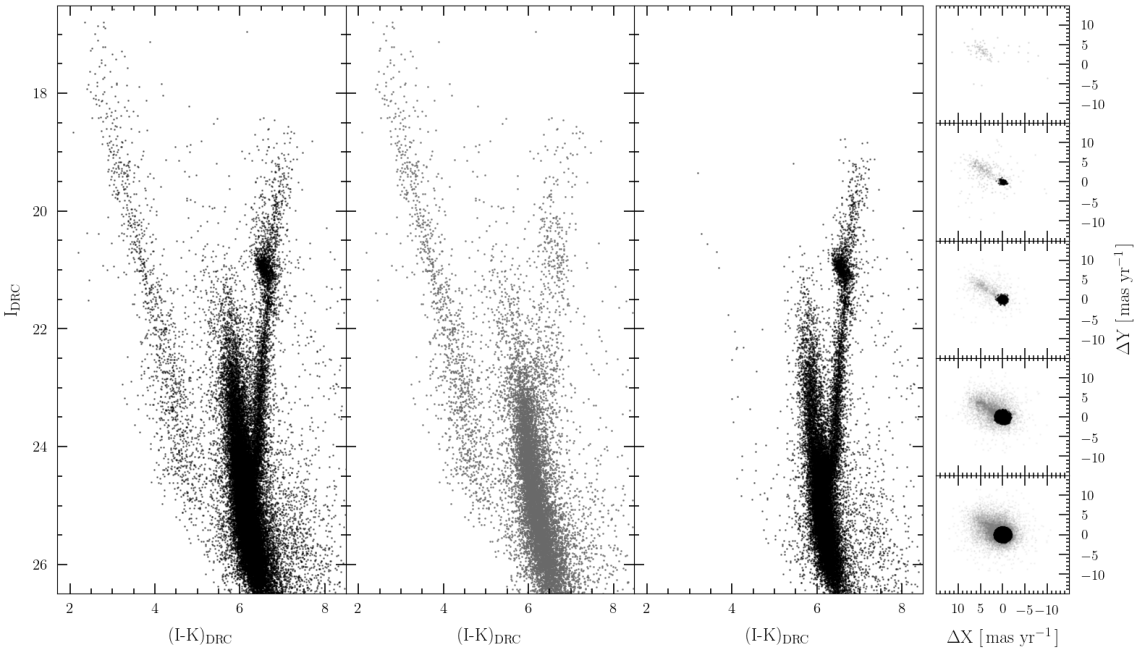


**Figure 3.2:** Panel (a): differential reddening corrected (I,I-K) CMD of the stars in common between GEMINI and HST, and with measured PMs. Panel (b): CMD of the field population as selected from the VPDs as those with PMs not compatible with that of Liller 1. Panel (c): PM-cleaned CMD of Liller 1 obtained by using only the likely cluster members selected from the VPDs shown in the rightmost column. Rightmost column: VPDs of the measured stars divided in 5 bins of 2 mag each, starting at $I_{\rm DRC} = 16.5$. Black dots represent the stars selected as likely cluster members.

### 3.3.1 The photometric catalog

The photometric catalog used for reconstructing the SFH of Liller 1 is the output of the data sets and photometric reduction described in Section 2.1.1 of the previous chapter. The catalog contains magnitudes in the F814W ($I$) and $K_s$ ($K$) filters acquired with the HST-ACS/WFC and GeMS/GSAOI camera, respectively (we refer the reader to the dedicated paragraph for all the details). Here, we display in Figure 3.1 the resulting FOV of $95'' \times 95''$ on the sky covered by the combined optical and infrared observations. The resulting CMD is shown in the leftmost panel of Figure 3.2, after the application of the corrections for differential extinction derived in Section 2.1.4.

In addition to the magnitudes, we exploited PMs that were computed for all the stars within the field of view covered by the GeMS exposures (see the black box in Figure 1.12) as explained in Section 2.1.3. Figure 3.2 shows that, as expected given its position in the Galaxy, the evolutionary sequences of Liller 1 are quite strongly contaminated by a significant fraction of field stars, whose CMD is shown with grey dots. Very prominent is the blue sequence visible at $I_{\rm DRC} < 25$ and $(I-K)_{\rm DRC} < 5.5$ and populated by young disk stars. As a sanity check, we estimated the fraction of not accounted field population by using the "Besançon model of stellar population synthesis of the Galaxy" (Robin et al., 2003). We retrieved the output of the model in the direction of Liller 1 for a solid angle corresponding to the area sampled by the Gemini data. Following the PM selection

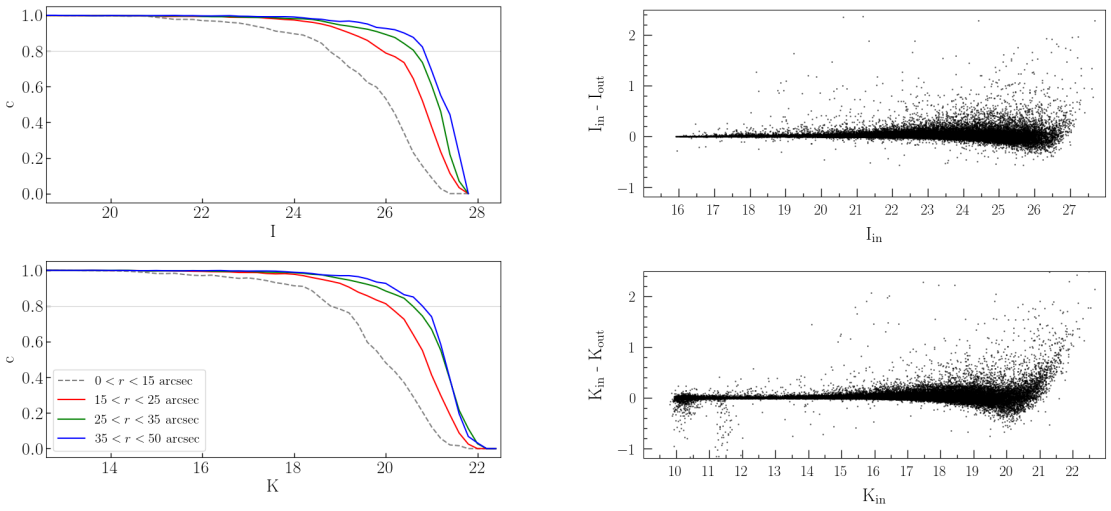


**Figure 3.3:** Left panels: Completeness curves as a function of the $I$ and $K$ obtained in three concentric annuli at different cluster-centric distances. The horizontal grey lines marks the 80% completeness level for reference. Right panels: differences between the input and output magnitudes in the $I$ and $K$ bands (upper and bottom panels respectively) for the artificial stars recovered by the photometric analysis.

described before, we selected stars moving with the same transverse velocity components as Liller 1 ($(\mu_\alpha cos\delta, \mu_\delta) = (-5.403, -7.431)\,\mathrm{mas\,yr^{-1}}$; from Vasiliev & Baumgardt 2021) within a tolerance range corresponding to the $3 \times \sigma$ selection adopted in Figure 3.2 (rightmost panel). In the Besançon simulation we find 2635 residual contaminating stars out of 22861 Liller 1 observed member stars (i.e. selected as members based on our analysis). If we then limit this comparison to the turn-off region ($24 < I_{\mathrm{DRC}} < 25$), we find $\sim$ 490 residual contaminating stars in the Besançon model out of 7447 likely member stars, thus yielding a residual contamination of $\sim$ 6%. We therefore expect a negligible impact of such a small residual contamination on the following analysis, and we safely performed the synthethic CMD fitting considering the diagram that occupies panel c) in Figure 3.2.

### 3.3.2 Artificial stars experiments

For the determination of the SFH of Liller 1, an accurate determination of photometric errors and incompleteness of the adopted data is needed (see Section 3.2). To this aim, we performed extensive artificial star experiments following the approach described in Dalessandro et al. (2015) with some ad-hoc modifications that are detailed below. We generated a catalog of simulated stars with an I-band input magnitude ($I_{in}$) extracted from a flat luminosity function (LF) extrapolated beyond the observed limiting magnitude in the (I-K, I) observed CMD. Then, to each star extracted from the LF, we assigned an input K magnitude ($K_{in}$) from a randomly extracted value of color in the interval 2 <(I-K)< 9 to homogeneously sample the range of magnitudes and colors occupied by stars in the observed CMD.

We then added artificial stars to real images adopting the same PSF models resulting

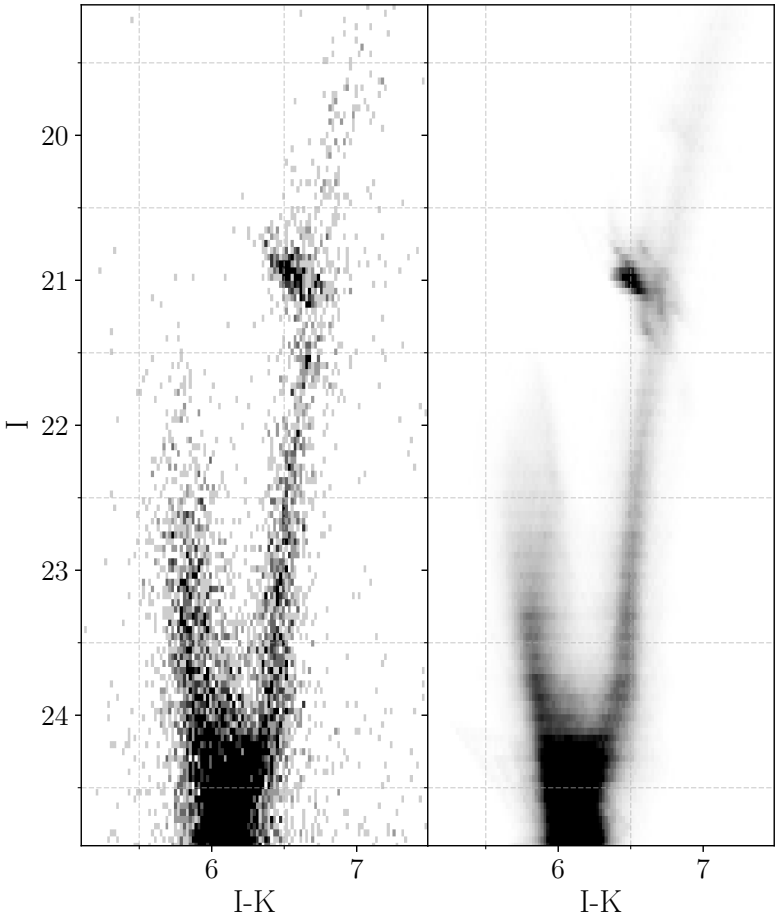


**Figure 3.4:** Hess diagrams for the observed CMD (left) and the best-fit synthetic CMD (right).

from the photometric analysis by means of the `DAOPHOTIV/ADDSTAR` package. Artificial stars were placed into the images in such a way they follow the stellar density profile obtained by Saracino et al. (2015) for Liller 1 (the parameters of this model are summarized in Table 1.1). To avoid artificial crowding, stars were placed in a regular grid composed by $20 \times 20$ pixel cells (which correspond to $\sim$10 times the stellar FWHM in the HST images), where only one artificial star was allowed to lie. In this way, for each run we could add a maximum number of $\sim$ 5000 artificial stars. We repeated this analysis several times to reach a final simulated catalog composed by more than 350,000 artificial stars, which is about 6 times larger than the number of observed stars. For each iteration, we performed the same photometric analysis described in Section 2.1.1. Those stars recovered after the photometric analysis have also values for $I_{out}$ and $K_{out}$.

The completeness is then defined as the ratio between the number of recovered artificial stars and that of the injected ones. Specifically, a star was not counted if it was not recovered during the photometric reduction, it was not included in the common ACS/WFC and GeMS field of views or it had a 0.75 brighter magnitude than its input to exclude cases where an artificial star is placed in the same spatial position as a real one with the same or brighter magnitude. The left panels of Figure 3.3 show the completeness curves as a function of both the $I$ and $K$ bands and obtained for four concentric annuli at different cluster-centric distances. The right panels show the distributions of the ($I_{in}$-$I_{out}$) and

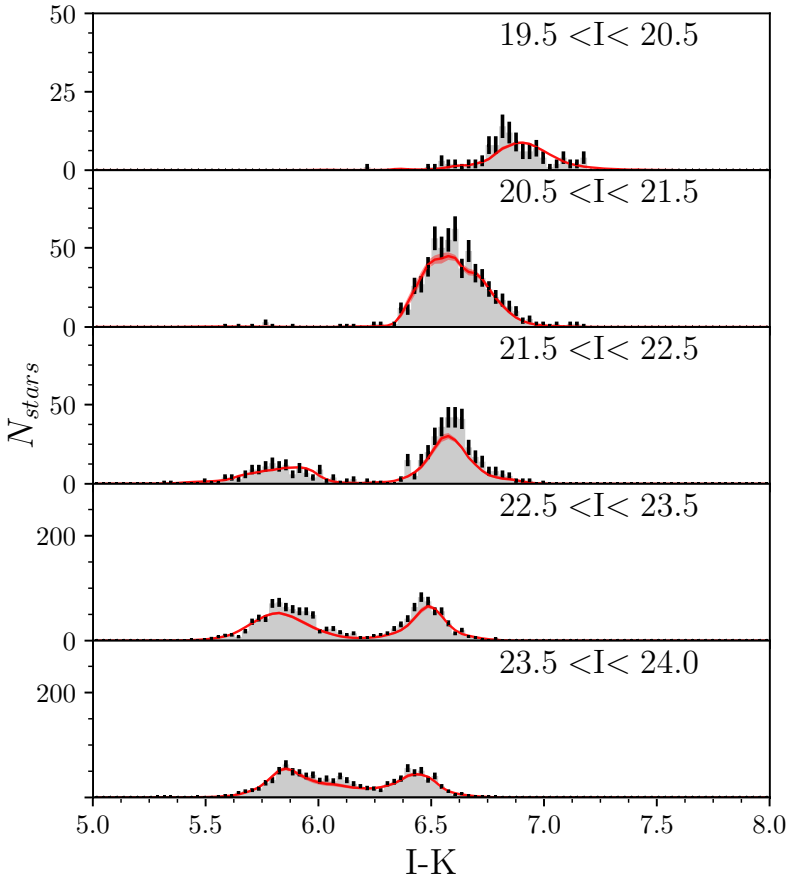


**Figure 3.5:** Observed color distributions of Liller 1 in four magnitude bins (grey shaded areas), compared to those obtained from our best-fit SFH solution (red lines). The black vertical segments correspond to the Poissonian error in each color bin, while the uncertainty in the synthetic distribution is marked by the red-shaded areas.

($K_{in}$-$K_{out}$) as a function of the input $I$ and $K$ bands, respectively. These distributions are used to quantify the photometric errors and the fraction of possible blends as a function of the magnitude and color.

### 3.3.3 The best-fit star formation history

The SFH was determined using the population synthesis routine SFERA (Cignoni et al. 2015, see Section 3.2), applied to the differential reddening and PM-cleaned CMD shown in the right panel of Figure 3.2, and adopting the set of input parameters as describe in Section 3.2.2. The severe crowding conditions of the innermost regions of Liller 1 hindered the possibility to effectively use the turn-off region for the entire available FOV. For this reason we decided to limit the SFH analysis to stars at cluster-centric distances larger than 15″, where the photometric completeness is generally larger than 80% for $I \sim 25$ (see Figure 3.3). We estimate that with such a selection we sample $\sim 40\%$ of the total mass of Liller 1.

SFERA estimated a best fit extinction corrected distance modulus of 14.65 and foreground reddening of $E(B-V) = 4.52$. These values nicely compare with those previously derived in Section 2.1.5. In Figure 3.4 we compare the observed and the best-fit

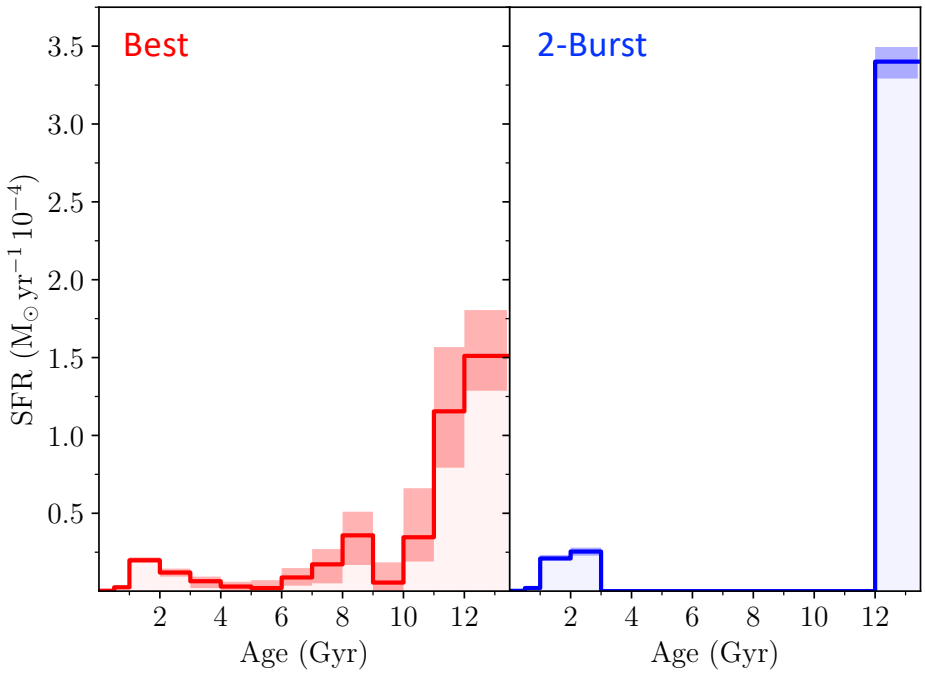


**Figure 3.6:** Best (red) and '2-burst' (blue) SFHs of Liller 1. The shaded areas define the regions between the 5th and 95th percentile values.

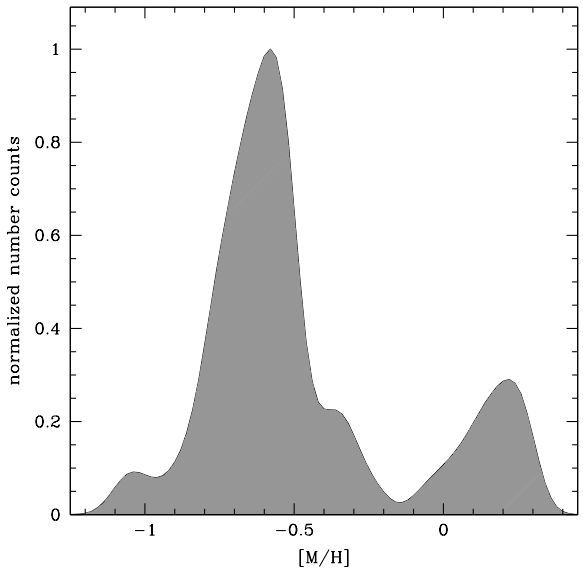


**Figure 3.7:** Generalized histogram of the metallicity distribution of Liller 1 as constrained from the best-fit SFH.

synthetic CMDs (left and right panels respectively) by showing their Hess diagrams for a first visual check. At a qualitative analysis, the synthetic CMD indeed nicely reproduces the main features of the observed one. In fact, it matches the observed turn-off, the color and magnitude extension of the blue plume, the RGB color width as well as the color extension and inclination of the red clump. For a more quantitative analysis, in Figure 3.5 we directly compare the color distributions obtained from the observed and the best-fit

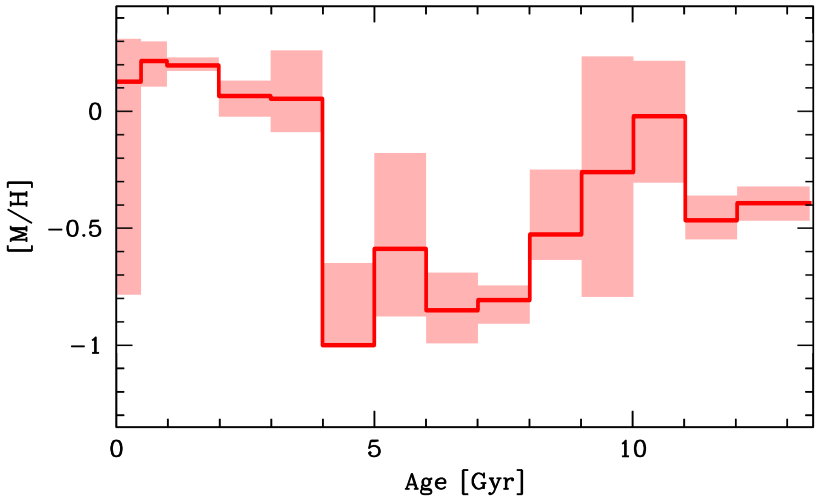


**Figure 3.8:** Age-metallicity distribution as recovered from the best-fit SFH. The shaded areas corresponds to the 5th and 95th percentile values.

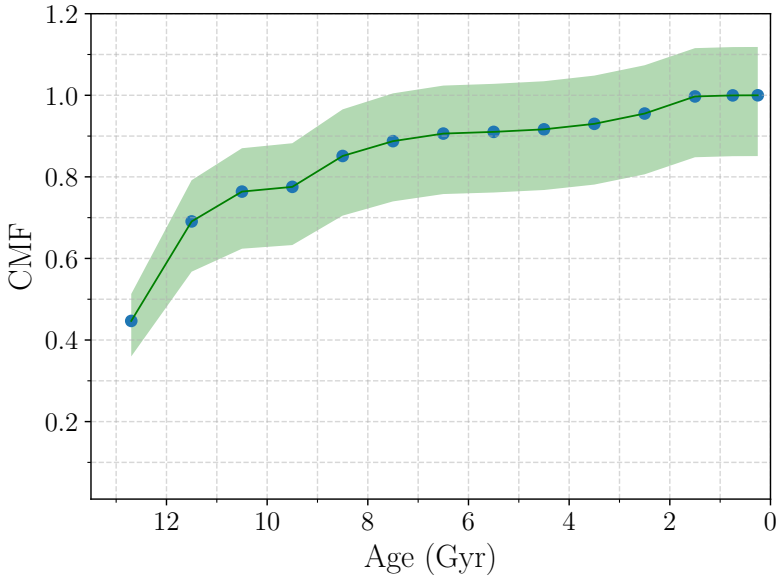


**Figure 3.9:** Cumulative mass distribution for the recovered SFH.

synthetic CMDs in four magnitude bins. The best-fit synthetic CMD reproduces fairly well the mean color and the width of all the main observed evolutionary sequences, even if in the mid/bright portion of the RGB and along the young MS ($21.5 < I < 23.5$) the best-fit synthetic CMD tends to slightly under-predict the number of observed stars. This difference can be ascribed to residual contamination from bulge + disk stars along the line of sight (see Section 3.3.1) and to a slight overestimate of the photometric completeness at the turn-off magnitude level of the old population ($I \sim 25$), which then produces smaller number counts at brighter magnitudes in the synthetic CMDs.

The resulting best-fit SFH is shown in red in Figure 3.6. The boundaries of the light-red shaded rectangles correspond to the 5th and 95th percentile values of the distribution of all the synthetic CMDs produced by SFERA and compared with the observations. The first key result emerging from Figure 3.6 is that Liller 1 has been active in forming stars

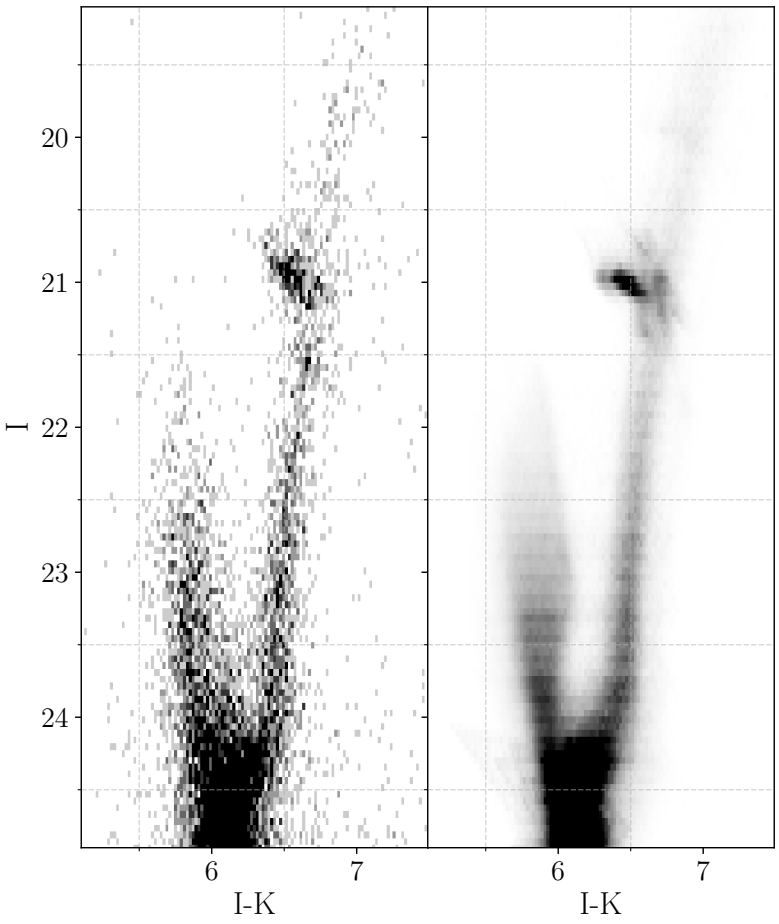


**Figure 3.10:** As in Figure 3.4, but now for the '2-burst' SFH solution.

over the entire Hubble time. More specifically, three SF episodes are clearly detected: 1) a dominant one, occurred 12-13 Gyr ago with a tail extending for up to $\sim 3$ Gyr; 2) an intermediate burst, between 6 and 9 Gyr ago; 3) a recent one, between 1 and 3 Gyr ago. In addition, our analysis shows robustly that about 1 Gyr ago Liller 1 stopped forming stars. It is worth stressing here that we can exclude this result arises because of saturation issues. In fact, saturation appears to become important at $I_{\rm DRC} < 19$, which is more than 3 magnitudes brighter than the turn-off magnitude of the 1 Gyr population.

In the best-fit recovered SFH, we find a broadly bimodal metallicity distribution (see Figure 3.7). The stellar metallicity mostly fluctuates in the range $-0.8 <$ [M/H] $< -0.4$ dex at the older epochs, then it increases with time and the metallicity of the younger populations (t$<$ 3 Gyr) peaks at [M/H] $\sim +0.2$ (Figure 3.8).

The cumulative mass distribution related to such a SFH is presented in Figure 3.9. It shows that more than $\sim 70\%$ of the total mass was produced during the first event of SF ($t > 10$ Gyr), thus confirming that the bulk population of Liller 1 is old (Ferraro et al., 2021). The remaining $\sim 30\%$ is then almost equally split between the second and third SF events, with the latter producing no more than $\sim 10\%$ of the total mass. We should recall at this point that the fraction of mass produced in the last 3-4 Gyr might be underestimated because of the radial selection adopted to perform the analysis. In fact, the younger stellar population of Liller 1 is more centrally concentrated than the older

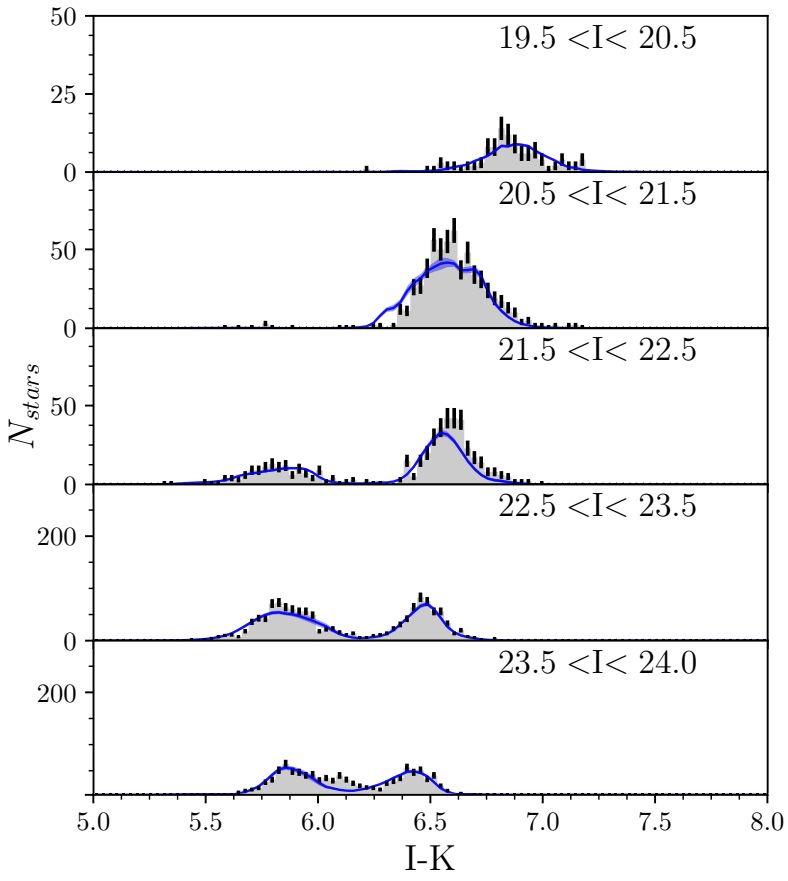


**Figure 3.11:** As in Figure 3.5, but now for the '2-burst' SFH solution.

ones and the number ratios between the young and old populations, is $0.98 \pm 0.04$ and $0.66 \pm 0.02$ for distances smaller and larger than 15″, respectively (see Ferraro et al. 2021). We also stress here that, while Blue Straggler Stars overlap with the distribution of young stars in the CMD, they have only a limited impact on the recovered SFH of the young component (< 3 Gyr) as they are expected to represent the $5 - 10\%$ of the total number of the blue plume population (see Section 2.1.5 for details about the number counts.)

### 3.3.4 An alternative star formation history solution

We tested the possible impact of poorly modeled observational uncertainties on the recovered SFH, and in particular on the results related to the older component where they can be more important because of the poorer ability to effectively distinguish populations with relatively small age differences. More specifically, we checked whether the old and the intermediate SF episodes can be safely considered as two separate events and, whether the resulting non negligible duration ($\sim 3$ Gyr) of the old SF episode is real. To this aim, we reperformed the SFH analysis by imposing a '2-burst' solution in which the first SF episode is older than 12 Gyr and the more recent one is younger than 3 Gyr. The resulting SFH (blue slope) is compared with the previous one (red slope) in Figure 7. The Hess diagram and the color number count distribution corresponding to the newly derived SFH are shown in Figure 3.10 and Figure 3.11 respectively. Although a reasonable match

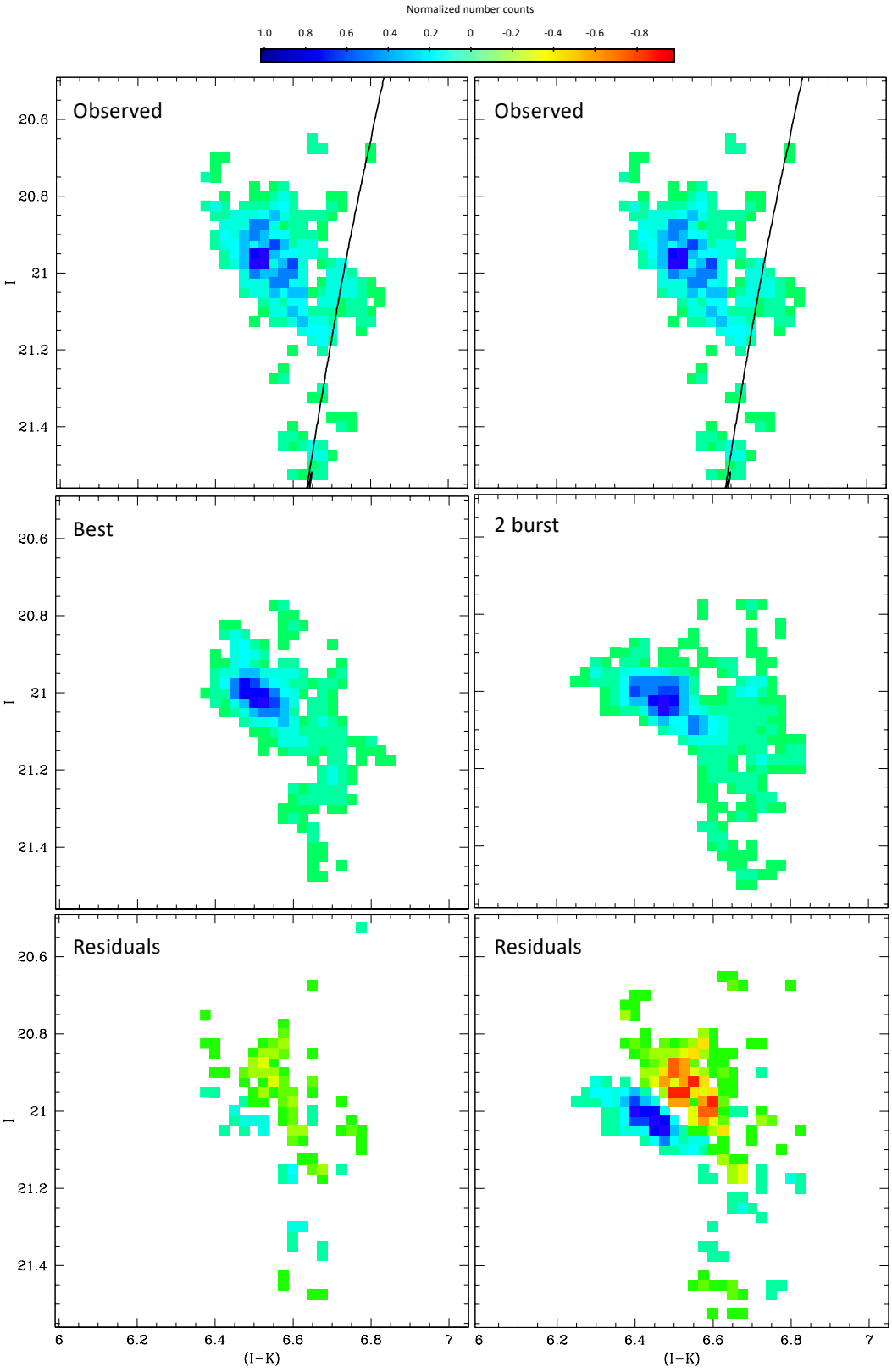


**Figure 3.12:** Upper panels: 2D distribution of the observed CMD density number counts in the red clump region. Middle panels: distributions of the synthetic stars as obtained from the best-fit and 2 burst SFH solutions. Lower panels: CMD distribution of the difference between the number of observed and synthetic stars.

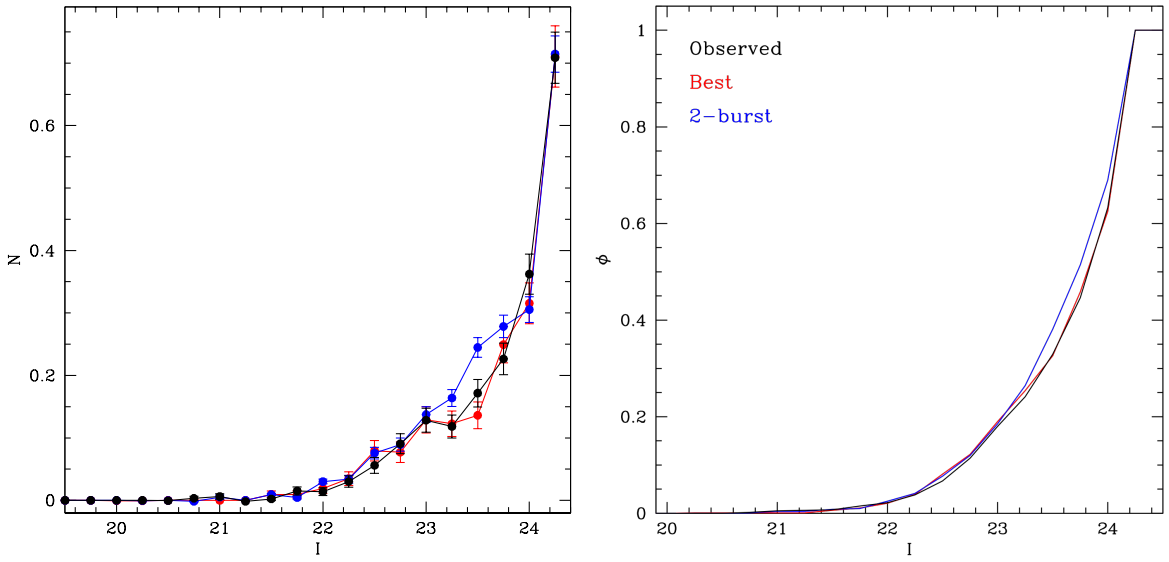


**Figure 3.13:** Upper panel: Normalized luminosity functions of the young MS population (I< 24, I-K< 6.3). In black is the observed distribution, while the red and blue curves refer to the best and 2 burst SFH solutions, respectively. Lower panel: the difference between the best and 2 burst LFs with respect to the observed are shown.

between the observed and the synthetic CMDs seems to be achieved also in this case, a closer look shows that the two SFHs show non negligible differences in specific CMD regions.

First, we note that when only two episodes of SF are assumed, the RC gets more horizontal than the observations and does not provide an adequate match to the observed color and magnitude distributions. In Figure 3.12 we compare the CMD star density distributions in the RC region of the difference between the observations and the two SFH solutions. Clearly, in the case of a SF with two discrete bursts the residuals gets larger and more structured. The main responsible for such a mismatch is likely the lack of stars with ages in the range $7 - 12$ Gyr and likely more metal-rich than the old component. In addition, we note that the '2-burst' SFH solution provides a worse match also of the young population MS distribution ($I < 24$, $(I - K) < 6.3$). In Figure 3.13, we compare the differential and cumulative luminosity functions (LFs) obtained from the observations (black line), with that resulting from the two SFH solutions (red and blue). The LF obtained with the best-fit SFH provides a better match of the observations. A KS test on the cumulative LF demonstrates that the '2-burst' LF is extracted from a different parent distribution than the observed one with a high degree of confidence ($P_{KS} \sim 5 \times 10^{-3}$).

Therefore, although we cannot completely exclude that the SFH of Liller 1 is bimodal and characterized by a very narrow old SF episode, we stress that a SFH with three episodes, and characterized by a first event with possibly an extended tail, followed by an intermediate and a young SF episode, provides an overall better match to the observations.

## 3.4 Another brick in the Bulge: the Star Formation History of Terzan 5

The application of the synthetic CMD fitting method to the BFF candidate Liller 1 showed the amount of information we can retrieve from the photometry of such complex stellar systems that is not evident from the sole application of isochrone fitting to their CMDs. The duration of the star formation episodes, as well as the presence of intermediate (and previously undetected) star formation bursts, are important discriminating factors in supporting the BFFs scenario. We therefore conducted an analogous analysis on Terzan 5, for which previous photometric studies (Ferraro et al. 2009, 2016, see Section 1.2.3 for a summary) detected an old and a young MS-TO, measuring an age of $\sim 12$ Gyr and $\sim 4.5$ Gyr, respectively. However, as shown in the case of Liller 1, this can be considered as a first order estimate of the SFH behind the CMD of Terzan 5, that requires a deeper investigation to shed further light on its formation mechanism. Specifically, the detection of a complex and extended SFH can rule out alternative formation scenarios that explain the presence of a young stellar population in this system by mergers with field GMCs (Bastian & Pfeffer 2022). Indeed, since such mergers are extremely rare events as predicted by current simulations (McKenzie & Bekki 2018), we should not observe a SFH characterized by several star, or rather extended, formation episodes (see also the discussion in Bastian & Pfeffer 2022).

### 3.4.1 Input catalog

As shown in Section 3.3, the combination of high-resolution IR and optical photometric data is a successful choice for analyzing the SFH of heavily extincted stellar systems like Terzan 5 and Liller 1. We therefore exploited the catalog built through the photometric reduction described in detail in Section 2.2. The catalog contains magnitudes in the $I$ (from HST-ACS/WFC) and $K$ (from MAD at VLT) bands, high-resolution differential reddening corrections, and PMs for the stars within the black square shown in Figure 3.14, that is the field of view covered by the infrared observations.

In order to ensure that the recovered SFH is not affected by bulge or disk interlopers, we estimated the degree of residual field contamination expected from the adopted PMs selection. The selection of cluster member stars is shown in Figure 3.15. Specifically, the rightmost panels displays the relative - and therefore centered on $(0, 0)$ - PMs distributions used to cleaned the CMD (vector point diagrams, VPDs). Following the criterion of Massari et al. (2015), we flagged as members of Terzan 5 all the stars within a radius of $1.5\,\mathrm{mas\,yr^{-1}}$ from the origin of the VPD plane. The result of this selection is shown in the first three panels of Figure 3.15, where we plot the CMDs made of likely field objects and bona fide member stars (middle and right panels, respectively), and we compare them to the uncleaned CMD (left panel). We quantitatively estimated the fraction of field interlopers by using two different methods. First, we used a Monte Carlo approach: we fitted with Gaussian functions the two PM components ($\Delta$X, $\Delta$Y) observed in the VPD (red points in Figure 3.15), and subsequently we drew 1000 realizations of such Gaussians, each time counting the number of randomly simulated field stars falling within

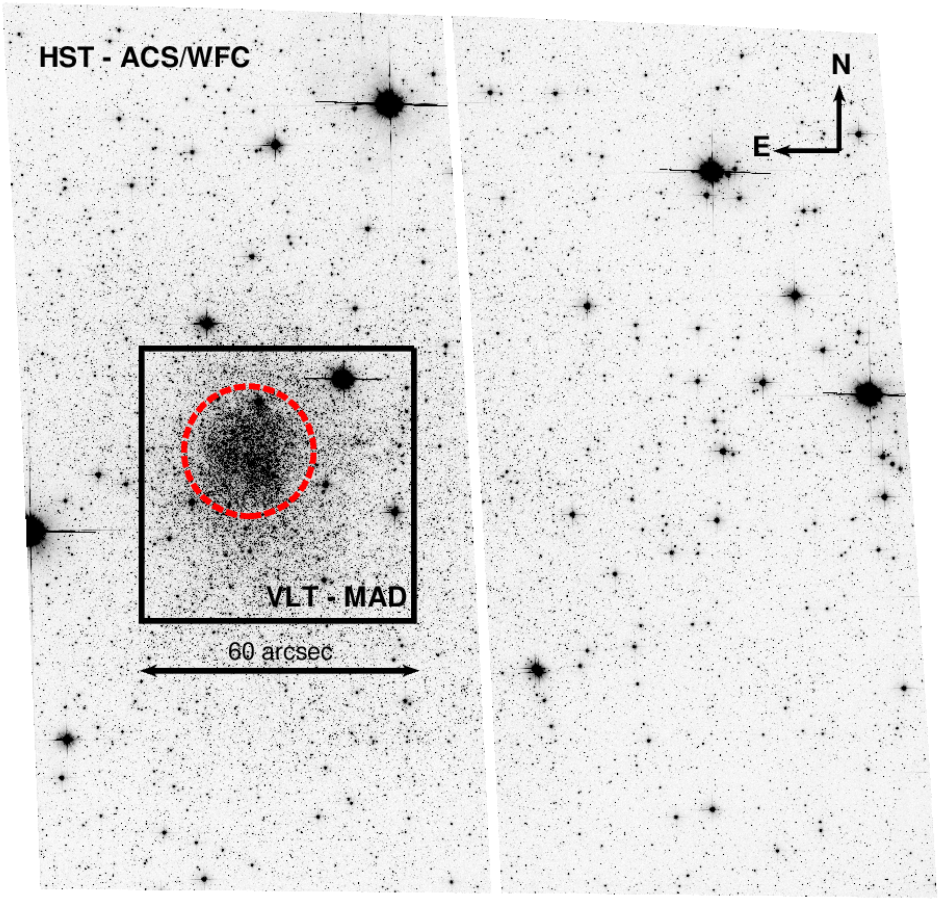


**Figure 3.14:** HST-ACS/WFC image of Terzan 5 in the F814W filter. The field of view is $204'' \times 204''$. The black box corresponds to the VLT-MAD pointing ($60'' \times 60''$). The region used for the SFH reconstruction is that beyond the red circle, corresponding to a radius of $15''$. North is up, east is to the left.

the $1.5\,\mathrm{mas\,yr^{-1}}$ radial limit. The contamination fraction is computed as the mean over the 1000 realizations. Second, we utilized the Python package `scikit-learn` (Pedregosa et al. 2011) to exploit the Gaussian mixture model (GMM) statistics. We forced the code to fit with two components the distribution of points observed in the VPDs, and we looked at the weight of the field stars component. In both cases, we obtained a contamination fraction lower than 5%, which is not expected to influence the SFH analysis. The low fraction of field objects is somehow expected, since we are considering a relatively small field of view centered on Terzan 5.

### 3.4.2 Photometric errors and incompleteness

A new photometric analysis has been necessary also for the determination of the incompleteness and photometric errors through artificial star tests. In fact, this method requires to re-perform the same photometric analysis that produced the observed catalog once artificial stars are placed onto the images.

Following the same procedure adopted in the case of Liller 1 (Section 3.3.2), we created a catalog of artificial stars extracting input magnitudes in the $I$ band ($I_{in}$) from a flat

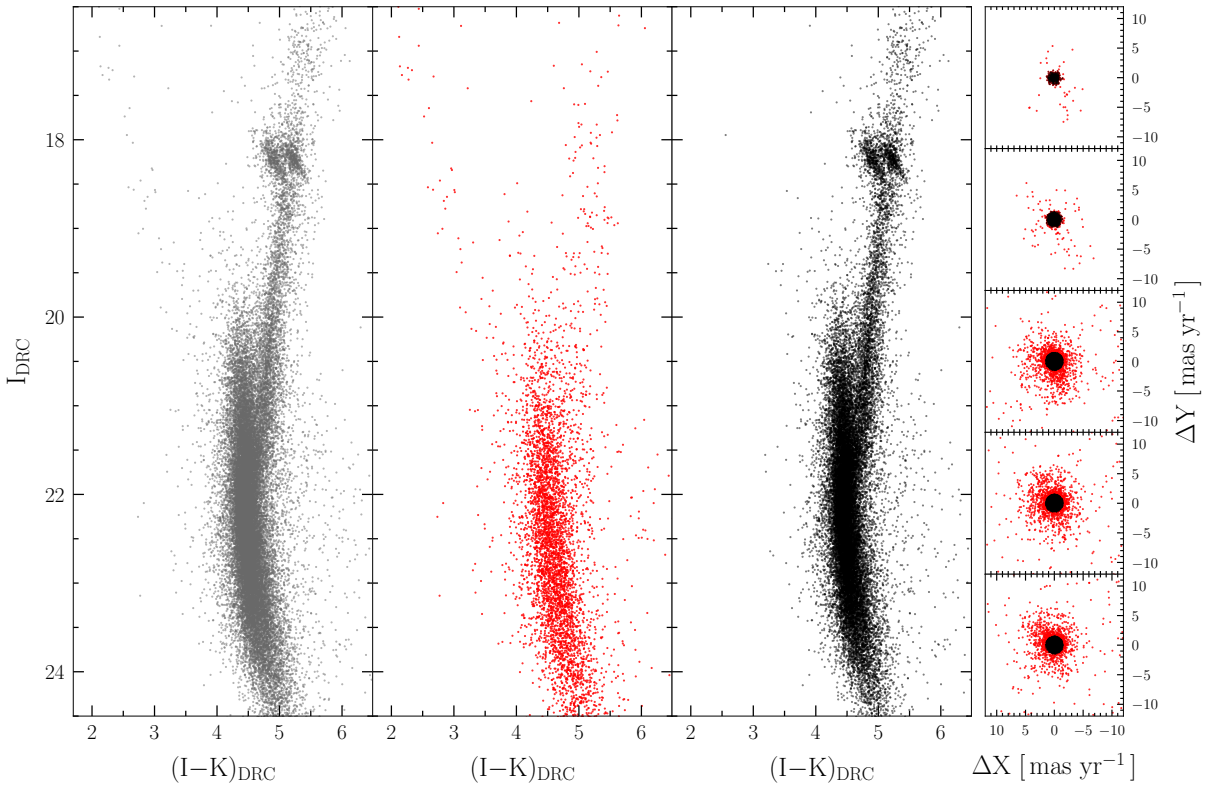


**Figure 3.15:** Left panel: DRC (I,I-K) CMD of the stars included in the MAD footprint, with measured PMs from Massari et al. (2015). Middle panel: CMD of the field population as selected from the VPDs as those with PMs not compatible with that of Terzan 5. Right panel: PM-cleaned CMD of Terzan 5 obtained by using only the likely cluster members selected from the VPDs shown in the rightmost column. Rightmost column: VPDs of the measured stars divided in 5 bins of 1.5 mag each, starting at $I_{DRC} = 16.5$. Black dots represent the stars selected as likely cluster members according to the criterion of Massari et al. (2015).

luminosity function (LF). The extremes of the LF were chosen to match the observed CMD. We added the input artificial stars on the images with the PSF models and Poisson noise resulting from the photometric analysis thanks to the `DAOPHOT/ADDSTAR` package. The stars were placed on the ACS/WFC images following the stellar density profile modeled by Lanzoni et al. (2010), which corresponds to a King model (King 1966) with structural parameters $c = 1.49$, $r_{core} = 9''$, and $r_t = 4.6'$. To avoid overcrowding, we divided the images into cells of $20 \times 20\,\mathrm{pixel}^2$ (more than 10 times the FWHM measured in the ACS/WFC), where only one artificial star was allowed to lie. We assigned to each artificial star a $K_{in}$ and a $V_{in}$ magnitude from a randomly extracted color in the range of the observed $(I - K)$ and $(V - I)$. In this way, we could homogeneously cover the color-magnitude plane of the observed stars. Thanks to the geometrical transformation between the different detectors and exposures calculated by `DAOMATCH`, we ensured to place artificial stars in the same location in the $V$, $I$ and $K$ images. We then performed the same photometric analysis described in Section 2.2.1 on the images containing artificial stars, and, at the end of the reduction, we cross-matched the output catalog with the one containing only input artificial stars. We iterated this procedure until the final catalog of artificial stars counted $\sim 700,000$ objects within the common FOV between the optical

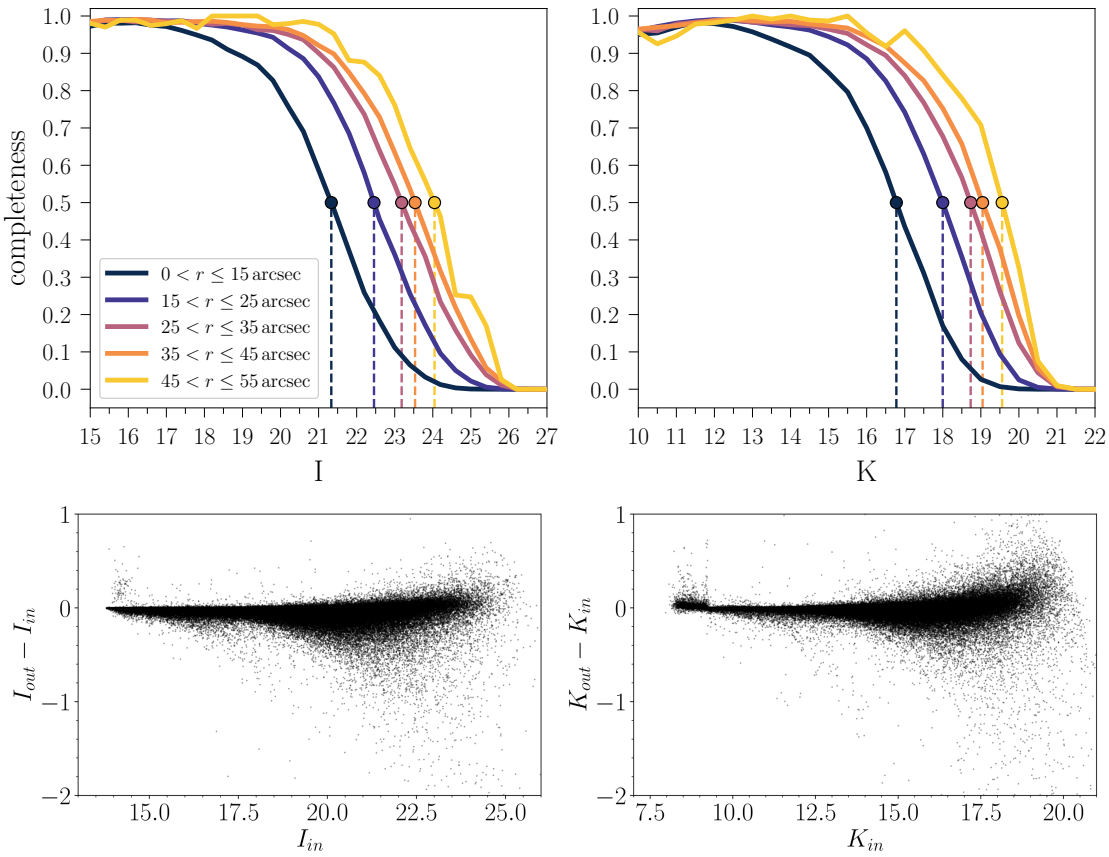


**Figure 3.16:** *Upper panels:* completeness curves as a function of the $I$ and $K$ magnitudes in different concentric annuli from the cluster's center. The colored dots and vertical lines highlight the limit magnitude at which the 50% is reached within the respective radial annulus. *Lower panels:* photometric errors, i.e. the difference between the input and output magnitudes, in $I$ and $K$ bands recovered from the artificial star tests.

and IR data sets (see Figure 3.14).

In this way, we could retrieve two important measures: on the one hand, it is possible to count the fraction of stars lost during the photometric procedure, obtaining an estimate of the completeness of the photometric catalog; on the other, for the recovered stars, the difference between the input and the output magnitude provides a more realistic estimate of the photometric errors. Specifically, the completeness was define as the ratio of the number of recovered stars and that of the injected ones. A star was considered lost if it was not detected in the $I$ or $K$ filter, or its recovered magnitude differed from the input value by more than 0.75 mag. This ratio is a function of the crowding conditions, as shown by the completeness curves displayed in the upper panles of Figure 3.16. These curves were built by diving the FOV in annuli centered on the cluster center of gravity (from Lanzoni et al. 2010). As shown Figure 3.16, the 50% completeness significantly drops in the first 15″ from the cluster center, with a corresponding magnitude of I = 21.3 and K = 16.8 (which is $\sim$ 0.3 mag brighter with respect to the MS-TO of the old population, see the red isochrone in Figure 2.12). On the other hand, at larger radii, the photometric completeness is equal or better than 80% at the MS-TO level. We concluded that the severe crowding of the innermost 15″ of Terzan 5 irremediably hampers the use of the MS-TO for the

determination of its SFH, and therefore we restricted the analysis to larger radial distances. The radial limit of 15″ is marked by a dashed red circle in Figure 3.14. Adopting this radial cut, we still sample the $\sim 45\%$ of the total mass of Terzan 5, computed considering the best King model of Lanzoni et al. (2010) from the projected density distribution.

Photometric errors and blends are assigned to the synthetic stars by using the distributions of $(I_{out} - I_{in})$ and $(K_{out} - K_{in})$ displayed in the bottom panels of Figure 3.16. As expected, the distributions become broader towards fainter magnitudes, indicating larger photometric uncertainties and blend effects.

### 3.4.3 SFERA best-fit solution

The reconstruction of the SFH was performed exploiting the code SFERA (Cignoni et al. 2015, see Section 3.2) applied to the DRC and PM-cleaned CMD of Terzan 5 showed in the right panel of Figure 3.15 (see the CMD made of black dots). We run the code following the input parameters described in Section 3.2.2, and we convolved the model CMDs with photometric errors and incompleteness as obtained from artificial star tests described in Section 3.4.2.

Figure 3.17 shows the set of outputs provided by SFERA corresponding to the best-fit solution. We let SFERA free to recover both distance modulus and average absolute color excess needed to best fit the observations. We obtain $\mu_0 = 13.75$ and $E(B-V) = 2.45$. The distance modulus is in agreement, within the uncertainties, with the value quoted in Valenti et al. (2007), while the color excess is 0.07 mag higher, being only marginally in agreement with the $E(B-V)$ calculated in the same work. However, it is worth recalling the remarkable variation of $E(B-V)$ across the FOV of the observations (see Section 2.2.2, but also Massari et al. 2012).

The upper-left panel of Figure 3.17 displays the density plots corresponding to the observed data (left panel) and the best-fit synthetic CMD (right panel) used to perform the minimization of the residuals. From a visual inspection of the Hess diagrams, it is evident that the best-fit solution nicely reproduces the extension and the color of the blue plume, the old MS-TO, and the complexity of the RC region. To quantitatively analyze the Hess diagrams, in the lower-left panel of Figure 3.17 we display the data (grey histogram) and best-fit solution (red lines) color functions in four different magnitude bins. These functions are a direct comparison of the number of model and observed stars in each CMD cell. Thus, they constitute a valuable tool to check the quality of the fit. Overall, the model color function satisfactorily reproduces the width and the mean color corresponding to the old MS-TO ($21 < I < 22$) and the blue plume ($20 < I < 21$), modelling young stars even in the last magnitude bin before the RC region ($19 < I < 20$). On the other hand, for magnitudes brighter than 21, it tends to slightly underestimate the number of redder stars and, focusing on the bright portion of the CMD, the color width of the RGB. As already discussed in Section 3.3.3, an overestimate of the completeness in the lower part of the CMD can lead to a lack of old stars in the bright regime of the CMD. This is also evident from the color function in the RC magnitude bin ($17 < I < 19$), where we observe a larger discrepancy between the model and the data at bluer colors, which are associated to the RC of the old stellar population (see Figure 1.9).

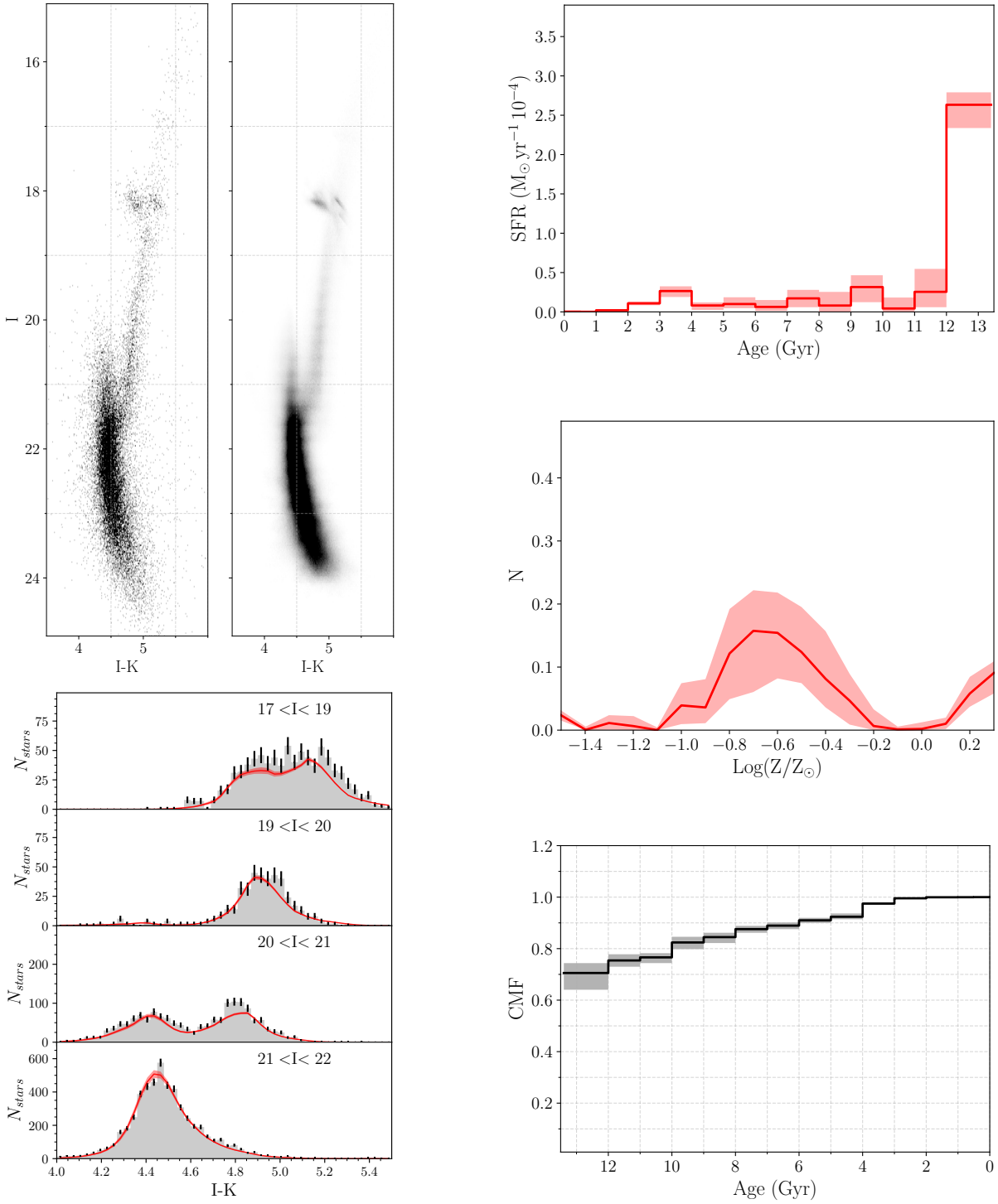


**Figure 3.17:** Results of the synthetic CMD method associated to the best-fit solution with $E(B-V) = 2.45$. *Upper-left panel:* Hess diagrams of the observed (left) and best-fit model (right) CMD. *Lower-left panel:* Color functions of the CMDs in four different magnitude bins; the data and relative Poissonian uncertainty are displayed in grey, while the models are the superimposed red line. *Upper-right panel:* recovered SFH. *Middle-right panel:* metallicity distribution as derived from the best-fit solution. *Lower-right panel:* cumulative stellar mass function for the recovered SFH. In all the panels, the red shaded areas are the uncertainties associated to the model computed from a bootstrap method, and they mark the 5th and 95th confidence level.

The red line in the upper-right plot of Figure 3.17 shows the SFH associated to the best-fit synthetic CMD. The corresponding shaded areas are its statistical uncertainties performed via bootstrap tests on the data, corresponding to the 5th and 95th percentiles of the distribution. If compared to the best-fit solution obtained for Liller 1 (see Section 3.3.3), the SFH of Terzan 5 exhibits a narrower main burst of SF at $t < 12$ Gyr, that confirms the age of the old population inferred by isochrone fitting (Ferraro et al. 2016). However, for ages younger than 11 Gyr, we can appreciate an ongoing star formation composed of several peaks, with the most relevant ones occurring at $\sim 7 - 10$ Gyr, and between $2 - 4$ Gyr ago. It is worth noticing that the youngest SF episode is remarkably statistically robust and extended over $\sim 2$ Gyr. This result differs from the conclusion of Ferraro et al. (2016), where only a single young population (that, in this framework, we could interpret as a young burst of star formation) was detected and approximated with an isochrone of 4.5 Gyr.

The metallicity distribution recovered from the best-fit solution (middle-right panel) shows a main broad peak in the range $-0.8 < [M/H] < -0.4$ dex, as in the case of Liller 1 (Figure 3.7). The mean metallicity $[M/H] \sim 0.7$ dex, which is associated to the old population, is $\sim 0.3$ dex lower with respect to the value measured in Massari et al. (2014) via high-resolution spectroscopy. On the other hand, the metallicity of the supersolar peak ($0.1 < [M/H] < 0.3$ dex), associated to stars younger than 4 Gyr, is nicely in agreement with previous spectroscopic studies.

Finally, we present the cumulative stellar mass function (CMF) associated to this solution in the lower-right panel of Figure 3.7. It shows that the bulk of the SF is due to the first burst, which built the 70% of the mass. Given the multiple SF burst, the CMF of Terzan 5 grows more gradually and less steeply with respect to the one of Liller 1, showed in Figure 3.5. Specifically, $\sim 10\%$ of the mass was built in the young SF episode. This barely reconciles with the estimate from Ferraro et al. (2016), which amounts to $\sim 38\%$ of the total mass, obtained by RC stars counts. However, due to observational limitations, we excluded from the analysis the first $15''$ from the cluster center, where a high concentration of young stars is expected because of the observed mass segregation of the young population (Lanzoni et al. 2010, Massari et al. 2014, see also Figure 1.11). Hence, the fraction of mass ascribable to the young stellar populations could be underestimated in this analysis.

### 3.4.4 An alternative star formation history

To explore the degree of degeneracy between metallicity and extinction, we derived a new SFH running a set of models fixing the value of reddening equal to $E(B-V) = 2.4$, more similar to the one quoted in literature ($E(B-V) = 2.38$[20], Valenti et al. 2007). The new Hess diagrams, as well as color distribution functions, SFH, metallicity distribution and CMF are shown in Figure 3.18, in the same order as displayed in Figure 3.17. The density CMDs and color number counts plots show clear discrepancies with respect to the data.

[20]However, it is important to specify that, in the case of Valenti et al. (2007), the mean color excess associated to Terzan 5 was determined by the analysis of the pure NIR plane (while we are basing our analysis on the hybrid CMD), and with no differential reddening corrections applied to the CMD.

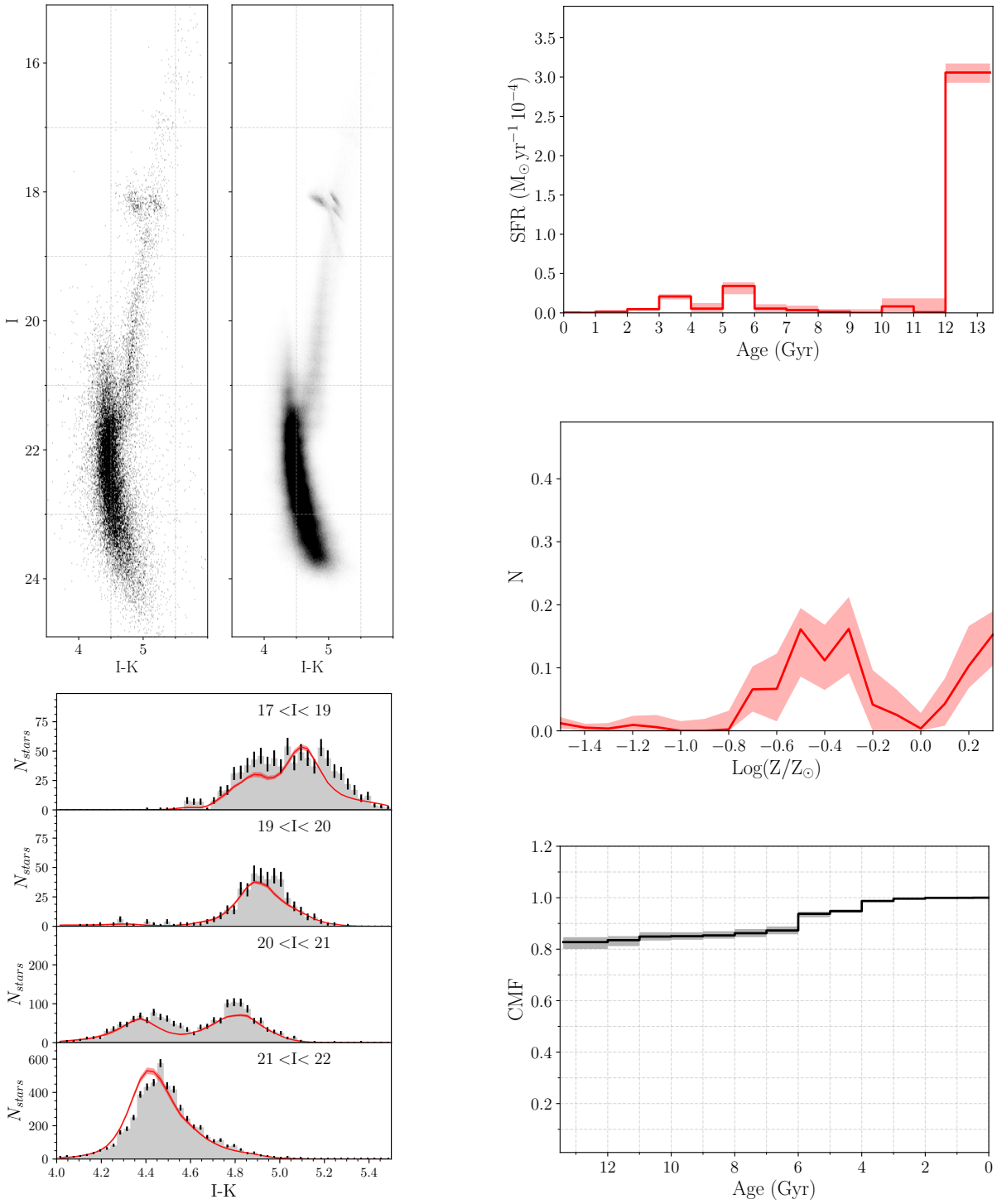


**Figure 3.18:** Same as in Figure 3.17. These results are associated to the best-fit solution considering $E(B-V) = 2.4$

The new solution predicts bluer colors in the region of the CMD corresponding to MS-TO of the old and the young stellar populations ($22 < I < 20$). In addition, this SFH provides a notable worse match of the RCs magnitude bin ($17 < I < 19$) with respect to the best-fit solution.

The SFH recovered by these models is still complex, showing multiple and discrete SF episodes at 3, 5 and 12 Gyr. Both recent SF peaks are recovered with a high statistical robustness, and they contribute almost in equal amount to the total SFH. The major difference between this solution and the best-fit one is represented by the intermediate burst at $\sim 5$ Gyr, which would be nicely in agreement with the age inferred to the young component of Terzan 5 via isochrone fitting (Ferraro et al. 2016). On the other hand, the most recent SF episode is compatible with the result described in the previous section, with only slightly lower SFR density for $t < 3$ Gyr. It is worth mentioning that this feature was not detected in previous photometric studies and it was unveiled by the new photometric catalog, that is characterized by a large, well-measured sample of stars.

The metallicity distribution recovered in this alternative SFH is once again broadly bimodal and similar to the result obtained through intermediate and high-resolution spectra. Indeed, the subsolar peak of the distribution ($-0.6 < [\mathrm{M/H}] < -0.2$ dex) is now shifted to higher metallicities, in agreement with the distribution observed in Massari et al. (2014), within the uncertainties (the metallicity distribution from Massari et al. 2014 is shown in the upper panel of Figure 1.10). However, we note that the fraction of metal-rich stars ($[\mathrm{M/H}] > 0$ dex) predicted by the model is increasing more rapidly with respect to the metallicity distribution associated to the best-fit solution (Figure 3.17). This in turn creates a supersolar peak with comparable height with respect to the subsolar one. This feature is undetected in the observed metallicity distribution, which, however, had been constructed by considering stars lying in the brightest part of the RGB, being naturally biased to the old and subsolar component.

Given the higher SFR associated to the main burst of SF, the CMF now predicts that more than 80% of the stellar mass is enclosed in the old stellar population. The remaining 15% was built through the subsequent SF events, of which only $\sim 5\%$ is due to the most recent burst.

Although this experiment shows, as expected, that exists a sensitive degeneracy between metallicity and reddening, on the other hand we can safely conclude that, in both cases, the SFH behind the CMD of Terzan 5 is bursting, showing multiple peaks (more than two) of SF at different ages. The most surprisingly fact is the overall time extension of the recent star formation activity, that would be barely reconcilable with the predicted (McKenzie & Bekki 2018) short timescales in which GMCs would form stars. Indeed, the measured young star formation activity needs a constant supply of gas to fuel SF bursts with a duration of more than 1 Gyr.

## 3.5 Summary of the star formation history investigation

Liller 1 and Terzan 5 are with no doubt among the most peculiar and interesting stellar systems in the Milky Way, and their origin is still strongly debated. Their present-day

properties, such as their chemical abundance patterns and their similarity with those of the Galactic bulge (Ferraro et al., 2009; Origlia et al., 2011), their present-day orbits (Massari et al., 2015), as well as their age-metallicity relations (Pfeffer et al., 2021) would suggest they are genuine Galactic stellar systems and would exclude they are the remnants of an external massive stellar system accreted by the Milky Way, like a dwarf galaxy (e.g., Tolstoy et al. 2009) or its nuclear star cluster (e.g., Neumayer et al. 2020).

Two main ideas have been put forward for their formation. One suggests that Terzan 5 and Liller 1 are the remnants of primordial massive systems, likely produced by the fragmentation of an early disk, that formed in situ and contributed to generate the bulge some 12 Gyr ago. The detection of similar structures in the star forming regions of high-redshift galaxies confirms that such massive fragments likely existed at the epoch of the Milky Way assembly. The second scenario suggests that both Liller 1 and Terzan 5 are the result of a relatively recent encounter between an old and massive GC formed in the bulge and a GMC orbiting the Galactic disk (Bastian & Pfeffer, 2022). Such an encounter should have been able to provide the necessary gas reservoir for the formation of the young populations observed in these systems (McKenzie & Bekki, 2018). The latter scenario is expected to produce two discrete and well separated SF episodes. Hence, to shed new light on the physical mechanisms driving the formation of Liller 1 and Terzan 5, in this chapter we present the first detailed analysis of their SFHs.

To this aim, we have used deep optical HST and IR Adaptive Optics data (GeMS/GSAOI and VLT/MAD) used in combination with a synthetic CMD analysis to derive the SFH of these systems. The best-fit solutions suggest that Liller 1 and Terzan 5 have been actively forming stars almost for their entire lifetime.

Specifically, in the case of Liller 1 we can identify three SF episodes. The main episode started $12-13$ Gyr ago with a tail extending for up to $\sim 3$ Gyr. This SF event is responsible for $\sim 70\%$ of the present-day total mass of Liller 1. The second peak occurred between 6 and 9 Gyr ago contributing to an additional $\sim 15\%$ of the system's mass. The most recent event started some 3 Gyr ago and stopped $\sim 1$ Gyr ago, when a quiescent phase started. Our analysis shows that the young population contributes at least to $\sim 10\%$ of the total mass of Liller 1. We also find that the best match with the observations is obtained by assuming a global average metallicity $[\mathrm{M/H}] = -0.5$ dex for the older stars, in quite good agreement with the few high resolution spectroscopic abundance measurements available in the literature (quoted in Section 1.3), and with $[\mathrm{M/H}] \sim +0.2$ dex for stars that were born in the last $\sim 3$ Gyr.

The best-fit solution associated to Terzan 5 predicts a main and narrow burst of SF around 13 Gyr ago, coupled with a decreasing and prolonged SF activity between 5 and 12 Gyr ago, and combined with a prominent recent SF episode started 4 Gyr ago and extended for $\sim 2$ Gyr. The fraction of total mass formed in the first SF episode amounts to $\sim 70\%$, while the subsequent SF bursts gradually built up the remaining 30%, with the younger SF episode being responsible for $\sim 10\%$. The average metallicity of the older stars assumed by the best-fit models peaks at $[\mathrm{M/H}] \sim -0.6$ dex, resulting more metal-poor with respect to metallicity measurements from previous spectroscopic screenings of Terzan 5 (Origlia et al. 2011, Massari et al. 2014). Nonetheless, young

($t < 5$ Gyr) stars are fitted by supersolar models peaking at [M/H] = 0.25 dex, in excellent agreement with the literature. The observed metallicity distribution function can be an important observational standard for critically evaluating the solution provided by SFERA, given that no metallicity priors, or rather age-metallicity relations, are assumed. On the other hand, this photometry-based MDF could be easily subject to a large dispersion and offset dependent on the degeneracy between reddening and metallicity, together with other observational limitations (uncertainty of magnitudes calibration, systematic offsets in the determination of photometric errors via artificial stars, and the extreme reddening conditions). In this regard, it is not surprising that the retrieved MDF is impressively similar to the one obtained for Liller 1 through this methodology. In both cases, the CMD fitting routine is struggling to properly reproduce the metallicity of the old, metal-rich (Massari et al. 2014; Crociati et al. 2023) and $\alpha$-enhanced (Origlia et al. 2011, 2013) stellar populations, suggesting that an additional responsible for this discrepancy can be the adopted set of solar-scaled isochrones. Future releases of the code SFERA will be optimize to deal with other set of stellar isochrones (e.g., BaSTI stellar evolution models; Pietrinferni et al. 2004, 2006) that will allow also to perform CMD fitting through $\alpha$-enhanced stellar models and evaluate possible bias in the recovered SFH.

For Liller 1, we performed an ad-hoc simulation including 'by hand' only two SF episodes at $t \sim 12$ Gyr and $t < 3$ Gyr. Although the CMD derived by using this approach is still broadly compatible with the data, we find that the specific number count distribution of the RC and young MS in the CMD (Figures 3.12 and 3.13) cannot be properly reproduced with such a configuration, but they are better fit by adopting a larger number of SF events lasting for a longer time. An alternative SFH was also recovered for Terzan 5, forcing the code to find the best-fit solution while reddening the stellar models with the literature value of $E(B-V)$ from Valenti et al. (2007). This configuration provides a metallicity distribution function nicely in agreement with literature spectroscopic measurements; however, the recovered synthetic CMD constitutes a notably worse match to the observed one. Nonetheless, this solution still predicts a complex SFH composed of three SF bursts at $\sim 13, 5$ and 3 Gyr ago.

The missing critical information to move the SFH analysis of these systems to another step of detail is to probe their chemical abundance patterns on a statistically significant sample, possibly including the young population. Especially in the case of Liller 1, we still lack of any robust spectroscopic screening, and the chemical abundance patterns of its populations are still unconstrained. On the other hand, this kind of investigation would greatly benefit from metallicity distribution functions based on a large and unbiased sample of stars (see the discussion in Section 3.4.4), that possibly could offer a more meaningful benchmark for evaluating the results provided by the CMD fitting method.

This chapter is based on the results presented in
Dalessandro, Crociati et al. (2022)
Crociati et al. (2024, in prep.)

# 4 The MUSE analysis of the Bulge Fossil Fragments

## 4.1 The missing chemical information

Multiple chemical screenings of the stellar population of Terzan 5 (Origlia et al. 2011, 2013; Massari et al. 2014, see also the introductory Section 1.2.3) demonstrated that it hosts at least two major subpopulations, ascribable to different star formation events: the first occurred $\sim 12$ Gyr ago, formed out of $\alpha$-rich ([$\alpha$/Fe]$= +0.34$ dex) gas exclusively enriched by CC-SNe up to [Fe/H] $\sim -0.3$ dex, while the second is much more recent (dating back to $2-4$ Gyr ago) and fueled by gas with supersolar metallicity ([Fe/H] $= +0.3$ dex) and solar-scaled [$\alpha$/Fe]. A third, minor (possibly older) component with [Fe/H] $= -0.79$ dex and [$\alpha$/Fe]$= +0.36$ dex seems also to be present (Origlia et al. 2013). This chemical pattern, which is typical of massive and dense environments that experienced star formation at very high rates, suggests that the progenitor system (the proto-Terzan 5) was massive enough (as the high-redshift clumps) to retain gas ejected by both CC-SNe and type Ia SNe, before igniting a second burst of star formation. The [$\alpha$/Fe] *vs* [Fe/H] pattern drawn by the subpopulations of Terzan 5 is perfectly consistent with that of bulge field stars, while it is incompatible with those of the Milky Way halo and Local Group dwarf galaxies (Tolstoy et al. 2009). Indeed, the observed pattern unambiguously demonstrates the Terzan 5 kinship with the bulge and strongly supports an in-situ origin, thus classifying it as a valuable candidate remnant of a massive clump that contributed to generate our spheroid.

This scenario can be further supported by the discovery that another GC-like object in the bulge, Liller 1, hosts two distinct populations with remarkably different ages: 12 Gyr for the oldest one, just 1-2 Gyr for the youngest component. The spectroscopic information currently available for Liller 1 suggests that its old population has a chemistry fully compatible with that measured for the old population of Terzan 5: [Fe/H] $= -0.3$ dex and [$\alpha$/Fe]$= +0.3$ dex (Origlia et al. 2002). However, this is based on just two giant stars, and no information is available for the young component, although photometric evidence suggests that it could be supersolar (see Section 2.1.5 and 3.3.3). In fact, the reconstructed star formation history of Liller 1 derived from the analysis of its color-magnitude diagram suggests the occurrence of three main bursts producing an overall bimodal iron abundance distribution (see Figure 3.7). Clearly, the detailed chemical characterization of the stellar populations in Liller 1 is urgent and of paramount importance: firmly assessing that Liller 1 is a multi-iron stellar system, with a tight chemical connection to the bulge, would

strongly indicate that, like Terzan 5, it is a Bulge Fossil Fragment, i.e. the living remnant of one of the primordial massive clumps that 12 Gyr ago contributed to the Galactic bulge formation.

As first step of this investigation, here we take advantage of the performance of the Multi Unit Spectroscopic Explorer (MUSE) at the VLT of the European Southern Observatory (ESO) to perform a preliminary screening of the iron abundance in a large number of stars in Liller 1. The iron abundance has been estimated from the equivalent width (EW) of CaII triplet (CaT) lines and adopting calibration relations provided in the literature. Specifically, Husser et al. (2020) provide a CaT-metallicity relation expressly calibrated for MUSE spectra, which links the EW of CaT lines at 8542 and 8662 Å and the difference between the star magnitude and the horizontal branch (HB) level in the HST F606W filter, with the iron abundance [Fe/H]. The relation holds for stars that are undergoing the red giant branch (RGB) or the HB evolutionary phase, and it has been calibrated using 19 Galactic GCs (from Dias et al. 2016) with metallicities ranging from [Fe/H] $\sim -2.3$ dex up to [Fe/H] $\sim -0.4$ dex. However, photometric (Ferraro et al. 2021) and spectroscopic (Origlia et al. 2002, 1997) studies suggest that the stellar populations in Liller 1 are more metal-rich (MR) than [Fe/H] $\sim -0.4$ dex. Therefore, as sanity check, we first tested the validity of this relation by analysing the MUSE spectra of three MR bulge clusters with [Fe/H] measurements from high-resolution spectroscopic studies, namely NGC 6569 ([Fe/H] $\sim -0.8$ dex; Valenti et al. 2011), NGC 6440 ([Fe/H] $\sim -0.5$ dex; Origlia et al. 2008), and NGC 6528 ([Fe/H] $\sim -0.17$ dex; Origlia et al. 2005).

Then, we decided to apply the same method to both Liller 1 and Terzan 5. In the case of Liller 1, we aim at retrieving the first metallicity distribution for this cluster, because, as already mentioned, the chemical pattern of its stellar populations is still unconstrained. In the case of Terzan 5, on the one hand we will be able to check the behaviour of the calibration relation in the supersolar metallicity regime, if any of the MR stars is detected; on the other, we have the possibility to perform the first *unbiased* metallicity distribution of this cluster (given that MUSE is an integral field spectrograph, we can potentially analyze the spectrum of each star included within its field of view). Indeed, previous spectroscopic screenings of the stellar populations of Terzan 5 are based on bright RGB stars , and they could be naturally biased to the detection of the old and subsolar population, hampering the evaluation of the real relative fraction of the different stellar components. Hence, this study can be considered as a trailblazer in the search for Bulge Fossil Fragments systems, constituting a novel approach for discovering new candidates and analyzing their properties.

## 4.2 Data Set

In this study we analized data acquired with the integral field spectrograph (IFS) MUSE mounted ad the ESO-VLT. The instrument is composed of 24 identical IFU modules that - when using the Wide Field Mode (WFM) - cover a field of view of $1' \times 1'$ , with a spatial sampling of $0.2''$ pixel$^{-1}$. WFM observations can be performed either with natural seeing (i.e., WFM-noAO), or combined with the Ground Layer Adaptive Optics mode (i.e.,

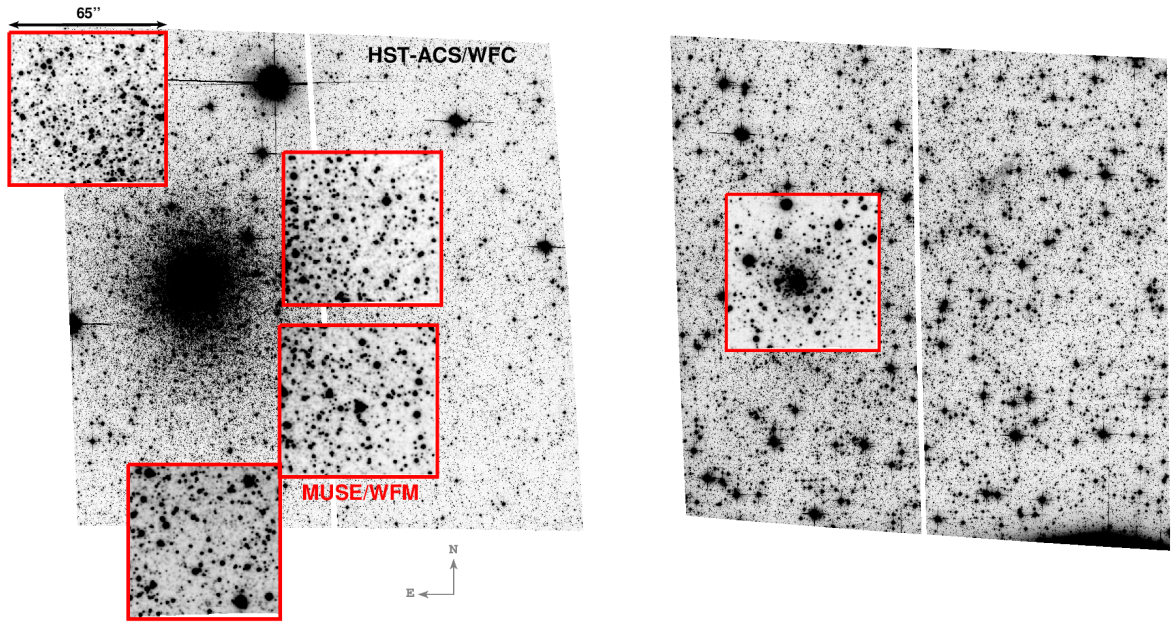


**Figure 4.1:** Reconstructed F814W images of the MUSE/WFM pointings (red boxes) used in the analysis of Terzan 5 (left) and Liller 1 (right). The field of view covered by each MUSE/WFM pointing is $\sim 65'' \times 65''$. The MUSE/WFM images are superimposed on HST-ACS/WFC observations of the relative stellar cluster in the F814W filter ($204'' \times 204''$). The HST images are the ones used to produce proper motions (PMs) and high-resolution photometric catalogs involved in the following chemical analysis (see Section 4.3). North is up, east is to the left.

WFM-AO) of the VLT Adaptive Optics Facility (AOF, Arsenault et al. 2008) through the GALACSI AO module (Ströbele et al. 2012). In addition, GALACSI enables the so-called Narrow Field Mode (NFM): a $7.5'' \times 7.5''$ Laser Tomography AO corrected field of view sampled at 25 mas pixel$^{-1}$. Spectrally, MUSE covers most of the optical range - i.e., 4800 - 9300 Å (nominal filter) and 4650 - 9300 Å (extended filter) - with a sampling of 1.25 Å and a resolution of $R \sim 3100$ at 8000 Å.

In the following we report the details concerning the data sets analyzed for the three reference GCs, Liller 1 and Terzan 5:

- NGC 6528 - For this cluster, we used four WFM-noAO archival observations that are part of the WFM science verification run (program ID: 60.A-9343(A)). Each exposure is 150 s long and was secured with a DIMM seeing of $\sim 0.85''$. The secured MUSE pointing was roughly centered on the center of the cluster.

- NGC 6440 - The data set for this cluster has been secured as part of the Multi Instrument Kinematic Survey of Galactic GCs (ESO-MIKiS survey; see Ferraro et al. 2018b,c; Lanzoni et al. 2018a,b; Leanza et al. 2023), a spectroscopic survey aimed at using the current generation of spectrographs mounted at the VLT to characterize the internal kinematics of a representative sample of GCs. Specifically, the data were acquired during the NFM science verification run (program ID: 60.A-9489(A), PI: Ferraro) and they consist of a mosaic of four MUSE/NFM pointings sampling approximately the innermost $15''$ of the cluster. This data set has been presented in Leanza et al. (2023) to discuss the kinematic properties of NGC 6440. Here we

analyzed the northern pointing with respect to the cluster center. Each exposure is 850 s long and the DIMM seeing during the observations ranged from 0.45″ to 0.8″.

- NGC 6569 - The observations of NGC 6569 are also part of the ESO-MIKiS survey and have been acquired under the Large Program ID: 106.21N5.003 (PI: Ferraro). They consist of seven MUSE/NFM pointings suitably displaced to sample the innermost 10″ from the cluster center. For each pointing, three 750 s long exposures were obtained, with a resulting DIMM seeing better than 0.7″. In this case, all the 7 pointings were used. The detailed description of this data set and the kinematic analysis of this cluster can be found in Pallanca et al. (2023).

- Liller 1 - The data set was acquired within the program 105.20B9 (PI: Ferraro) and is composed of five exposures in the MUSE/WFM-noAO configuration centered on the cluster center (see the right panel of Figure 4.1). All the exposures are 880 s long, with an average DIMM seeing ranging from 0.8″ to 0.9″.

- Terzan 5 - The WFM-noAO exposures used in this case of study come from the observing program 097.D-0869(A) (PI: Ferraro). This proposal acquired a total of 10 ring-shaped pointings covering a radial radial range from 50″ to 200″. Among all the pointings, we considered the ones overlapping the HST-ACS/WFC footprint of the observations exploited in Massari et al. (2015) for the proper motions (PMs) measure of the stars in the direction of Terzan 5. As extensively discussed in the following Section 4.3, an important prerequisite for the safe success of this analysis is the involvement of high-resolution and PMs based photometric catalogs, containing magnitudes in the F606W filter. Hence, we restricted the investigation to the four MUSE pointings displayed in the left panel of Figure 4.1. This configuration covers a radial distance of $\sim$ 50″-120″ from the cluster center. The observations are composed of three exposures, each of which is $\sim$ 870 s long, except for the southernmost pointing, which is composed of two $\sim$ 830 s long exposures. The DIMM seeing during the observations ranged from 0.48″ to 1.4″.

## 4.3 Data Analysis

For all the stellar clusters analyzed in this study, we adopted the same data analysis procedure, which can be summarized in five main steps: (1) reduction of the MUSE data and combination of the multiple exposures into the final datacube, (2) extraction of the spectra from the MUSE datacube, (3) measure of the radial velocity (RV) of each of the extracted spectra, (4) measure of the EW of the two strongest CaT lines, and (5) determination of the star metallicity.

*(1) Reduction of the MUSE data* - The data reduction was performed making use of the most recent version of the standard MUSE pipeline (Weilbacher et al. 2020). In this step, bias subtraction, flat fielding, wavelength calibration, sky subtraction, astrometric and flux calibration, and heliocentric velocity correction are performed for each exposure of each individual IFU. Subsequently, the processed data coming from all the 24 IFUs are

combined in a single datacube. Finally, we combined all the available exposures together, obtaining the final datacube for each stellar cluster.

*(2) Extraction of the spectra from the MUSE datacube* - As second step, we extracted individual star spectra from the final datacube by using the software PampelMuse (Kamann et al. 2013). This pipeline is recommended for extracting spectra from observations of crowded stellar fields, since it can perform source deblending through a wavelength-dependent point spread function fitting. For a successful extraction, PampelMuse requires as input a fiducial photometric catalog with high spatial resolution, high photometric completeness and high astrometric accuracy. Hence, for each considered cluster, we adopted an accurate photometric catalog obtained from HST observations, also including differential reddening corrections and PM information. In the case of NGC 6528, we used the photometric catalog published in Lagioia et al. (2014), which includes F606W and F814W magnitudes measured from the HST-ACS/WFC camera. For NGC 6440, we adopted the catalog presented in Pallanca et al. (2021a), based on HST/WFC3 observations in the same filters. This was also adopted in Leanza et al. (2023) for the extraction of the MUSE spectra for the entire data set discussed there, while here we used the spectra acquired in the northern pointing only. The high resolution photometric catalog available for NGC 6569 is the one presented in Saracino et al. (2019), providing HST/WFC3 optical images in the F555W and F814W filters, together with near-infrared (NIR) $J$ and $K_s$ images acquired with the Gemini multi-conjugate adaptive optics system GeMS. The photometric catalog used for Liller 1 is described in detail in Section 2.1.1. It is based on high-resolution HST-ACS/WFC observations in the filters F606W and F814W, once more combined with $J$ and $K_s$ images acquired with Gemini/GeMS (see also Saracino et al. 2015). The photometric cataolg used for Terzan 5 is the one summarized in Ferraro et al. (2016). It contains magnitudes in the F606W and F814W filters derived from the reduction of HST-ACS/WFC images. Moreover, it benefits from the PM measurements and differential reddening corrections from the works of Massari et al. (2015) and Massari et al. (2012), respectively.

PampelMuse needs in input a specific photometric band and an analytical PSF model. We choose as input magnitudes those in the F814W filter - except for Terzan 5, for which we considered magnitudes in the F606W band - and as PSF model, the Moffat function in case of WFM observations, and the MAOPPY function (Fétick et al. 2019) in the case of NFM data (see Leanza et al. 2023 for additional details about the extraction and the reduction of the NFM data set). For the following analysis, we only considered extracted spectra flagged as "adequate" by the software, which correspond to a required signal-to-noise ratio $S/N \geq 10$.

*(3) Measure of the radial velocity* - The next step is the determination of the stars' RV, used to check and possibly further constrain the cluster membership already inferred from the available proper motions. For NGC 6440 and NGC 6569 we used the RV catalogs obtained, respectively, in Leanza et al. (2023) and Pallanca et al. (2023), while for NGC 6528, Liller 1, and Terzan 5 we computed the RVs following the procedure explained in Leanza et al. (2023). This is based on the measure of the Doppler shift of the CaT lines from the comparison between the observed stellar spectrum and the relative best-

fit synthetic model chosen from a library of templates. Our library was composed of synthetic spectra generated with the SYNTHE code (Sbordone et al. 2004 and Kurucz 2005) spanning a metallicity range from $-0.5$ dex to $+0.5$ dex with a step of 0.25 dex, and temperatures varying from 3750 K to 4750 K with a step of 250 K. Once the observed spectrum is normalized to the continuum by means of a spline fitting in the 7300 - 9300 Å wavelength range, the procedure computes the residuals between the observed spectrum and each template shifted in velocity in steps of 0.1 km s$^{-1}$. We considered as the best-fit synthetic spectrum the one providing the distribution of the residuals with the smallest standard deviation. As a consequence, the RV of the star is obtained from the minimum of the distribution. As already shown in Valenti et al. (2018) and Leanza et al. (2023), considering the metallicity range of our interest ([Fe/H] $\geq -1$), the typical uncertainty on the estimated of individual RV is $\sim 8$ km s$^{-1}$ for the stars with the lowest $S/N$ ratio and it decreases up to $\sim 1.5$ km s$^{-1}$ for the targets with the highest $S/N$ (i.e., $S/N \geq 40$).

In Figure 4.2 we show the RV distributions of all the spectra extracted with PampelMuse (grey histograms). As can be seen, in the considered cases, the population of cluster members is clearly distinguishable as a narrow, strongly peaked component, while the bulge and disk field components appear as a sparse population, spanning a wide range of RVs (see the cases of NGC 6569 and NGC 6528), or define a broad distribution peaking at a different mean value (as clearly visible in the cases of Terzan 5 and Liller 1).

The cluster systemic velocity ($V_{\rm sys}$) has been estimated as the mean value of the sole likely cluster members after a $3\sigma$-clipping rejection removing stars with clearly discrepant RVs. It is worth of emphasizing that in the case of Liller 1, only 11 stars over the 171 PM-selected ones show RV inconsistent with the cluster systemic velocity. This provide a further confirmation that the PM-selected sample discussed in the previous chapters (see Section 2.1 and 3.3) is largely dominated by stars belonging to Liller 1, and only marginally affected by residual bulge contamination. Similarly, looking at the RV distribution of Terzan 5 member stars according to the only PM-based criterion (see the blue histogram in the lowest panel of Figure 4.2), the contamination caused by field interlopers is not remarkably important. Even if the PM distribution of bulge field stars basically overlaps the one drawn by Terzan 5 members (see Massari et al. 2015), and here this effect could have been exacerbated since we are considering an external corona with respect to the cluster center, only the 6% of the 402 PM-selected objects (blue histogram) is excluded by the $\sigma$-rejection procedure (i.e., stars not included in the orange histogram). However, this estimate shows that the joint RV and PM selection is still fundamental to properly disentangle cluster member stars from field interlopers.

By construction, for NGC 6569 and NGC 6440 we obtain $V_{\rm sys}$ values (see labels) fully consistent with those quoted in Pallanca et al. (2023) and Leanza et al. (2023), respectively. For NGC 6528, Liller 1, and Terzan 5 we found $V_{\rm sys} = 211.7 \pm 0.3$ km s$^{-1}$, $V_{\rm sys} = 67.9 \pm 0.8$ km s$^{-1}$, and $V_{\rm sys} = -81.3 \pm 0.7$ km s$^{-1}$, respectively. While the value obtained for NGC 6528 is in agreement with that ($V_{\rm sys} = 211.86 \pm 0.43$ km s$^{-1}$) quoted in Baumgardt & Hilker (2018), in the case of Liller 1 it turns out to be significantly different ($V_{\rm sys} = 60.36 \pm 2.44$ km s$^{-1}$), possibly due to a residual contamination from field stars in the sample analyzed by Baumgardt & Hilker (2018). Conversely, a nice agreement is found for Terzan 5,

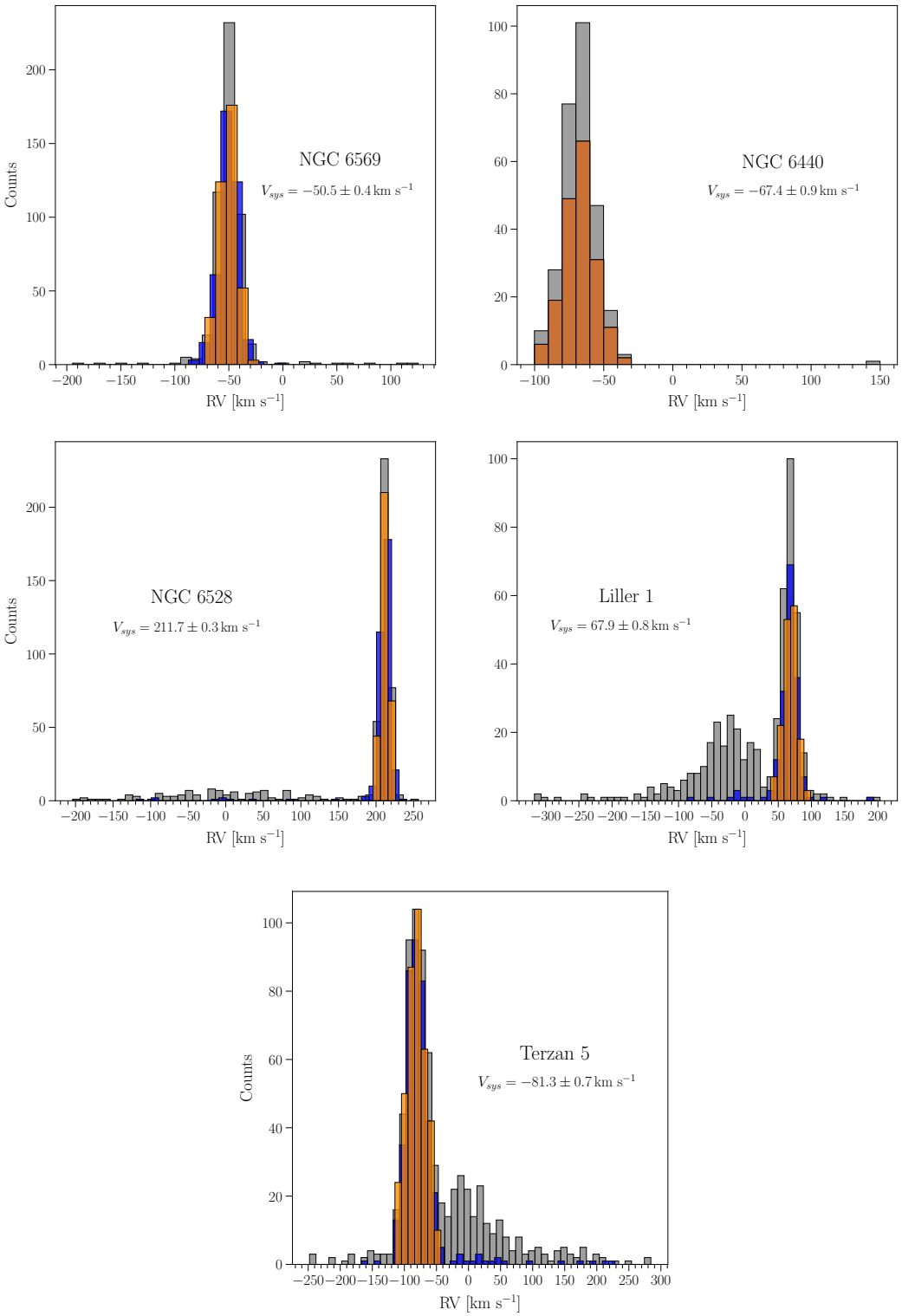


**Figure 4.2:** The grey histrograms show the RV distributions for all the stars extracted with PampelMuse (i.e., having spectra with $S/N \geq 10$) in the three reference clusters (NGC 6569, NGC 6440 and NGC 6528), in Liller 1 (from top-left, to bottom-right: see labels), and Terzan 5 (lowermost panel). The histograms shown in blue and orange colors correspond, respectively, to the sub-sample of PM-selected member stars, and the one further refined with a $3\sigma$-rejection applied to the measured RVs. The mean RV ($V_{sys}$), with the relative error, of the orange distributions are also labelled in the panels.

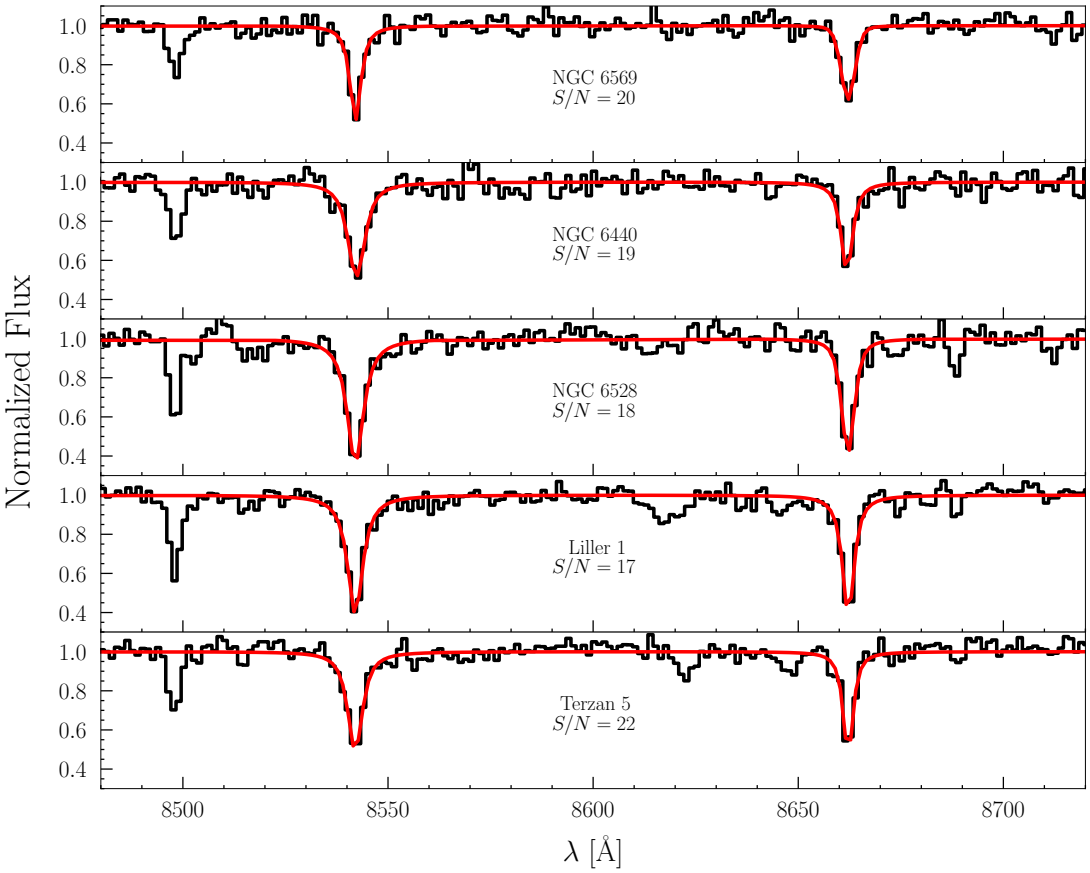


**Figure 4.3:** Examples of normalized spectra with $S/N > 15$ for each of the 5 stellar systems analyzed in this Chapter. The observed spectra are shown in black, while the best fitting Voigt models for the two strongest CaT lines are overplotted in red.

considering that the $V_{\rm sys}$ quoted in the database of Baumgardt & Hilker (2018) is equal to $V_{\rm sys} = -81.96 \pm 0.85$ km s$^{-1}$.

The values of $V_{\rm sys}$ thus derived have been used for the selection of member stars, taking into account the PM information and requiring that the RV is within $3\sigma$ the cluster systemic velocity. Only for a few objects in Liller 1, for which no measured PM was available, the membership is based only on the RV value. The sample of member stars thus obtained counts a total of 387 stars in NGC 6569, 184 stars in NGC 6440, 322 stars in NGC 6528, 160 stars in Liller 1, and 378 in Terzan 5.

*(4) Measure of the EW of the two strongest CaT lines* - Following the prescriptions presented in Husser et al. (2020), we computed the EW of the CaT lines for all the member stars selected in step (3). First, we normalized the spectra by fitting a second-degree polynomial to the region of the spectrum that they adopted for the definition of the continuum (specifically, 8674-8484 Å, 8563-8577 Å, 8619-8642 Å, 8700-8725 Å, and 8776-8692 Å). According to their approach, we used as "observational quantity" the sum of the equivalent widths (ΣEW) of the two broader lines at 8542 Å and 8662 Å. Hence, we fit

a Voigt profile to each of the two considered lines in the wavelength ranges 8522-8562 Å and 8642-8682 Å, respectively. The integration of the best-fit model in the considered wavelength ranges yields the EW of the two lines, and finally ΣEW. To determine the parameters of the best-fit Voigt function, as well as the uncertainties associated to the measured EWs, we applied the Markov Chain Monte Carlo (MCMC) sampling technique using the `emcee` code (Foreman-Mackey et al. 2019) to sample the posterior probability distribution. We assumed the following log-likelihood:

$$\ln \mathscr{L} \propto -\frac{\chi^2}{2} = -\sum_{i=1}^{N} \left( \frac{F_{\mathrm{mod},i} - F_{\mathrm{obs},i}}{\sqrt{2}\delta F_{\mathrm{obs},i}} \right)^2, \tag{4.1}$$

where $N$ is the number of pixels in the line bandpass, $F_{\mathrm{mod},i}$ is the $i$th value of the Voigt model, $F_{\mathrm{obs},i}$ is the $i$th value of the normalized observed flux, and $\delta F_{\mathrm{obs},i}$ is the associated flux uncertainty (which is provided in output by PampelMuse) once normalized to the same observed continuum.

For each absorption line, we run the MCMC adopting flat priors on the Voigt function parameters. Every 500 steps of the final chain, we extracted the corresponding function parameters and calculated the relative EW. We assumed as best-fit Voigt model the one corresponding to the 50th percentile, while the errors correspond to the 16th and 84th percentiles. This analysis suggested that to minimize the overall uncertainty in the measure of the EWs, a spectrum with a relatively high $S/N$ ratio is required. For this reason we conservatively decided to limit the quantitative measure of the EWs only to the stellar spectra with $S/N \geq 15$. This assumption sensibly reduces the number of stars actually measured in each cluster, but it guarantees an appropriate characterization of the continuum and a solid evaluation of the CaT line intensities. For the sake of illustration, in Figure 4.3 we show five normalized spectra (one for each cluster) with comparable $S/N$ ratios, and the corresponding best-fit models.

*(5) Determination of the star metallicity* - Following Husser et al. (2020), we then computed for each star the mean reduced EW ($W'$), which is defined as:

$$W' = \Sigma\mathrm{EW} + 0.442(V - V_{\mathrm{HB}}) - 0.058(V - V_{\mathrm{HB}})^2, \tag{4.2}$$

where and $V - V_{\mathrm{HB}}$ is the difference in magnitude between every considered star and the cluster Horizontal Branch level, both measured in the F606W HST filter. The definition of the mean reduced EW therefore includes a combination of the measured ΣEW and the brightness of the observed stars, under the assumption that, at fixed metallicity, the strength of the CaT lines mainly depends on the stellar luminosity. To calibrate the relation between $W'$ and [Fe/H], Husser et al. (2020) adopted the metallicity values listed by Dias et al. (2016) for a sample of 19 Galactic GCs, and they presented three possible solutions corresponding to a linear, quadratic, and cubic best-fit to the data. In the following analysis we adopted the linear calibration:

$$[\mathrm{Fe/H}] = (-3.61 \pm 0.13) + (0.52 \pm 0.03)W'. \tag{4.3}$$

This is indeed the most conservative and safe assumption for a work devoted to the exploration of the MR end of the GC iron distribution. In fact, the relations of Husser et al. (2020) must be essentially extrapolated at [Fe/H] $> -0.5$ dex, because this metallicity regime is not properly sampled by their calibrators. However, it is well known that extrapolating a quadratic or cubic relation is always much more dangerous than extrapolating a linear one. In addition, the iron abundance of their most MR calibrator (NGC 6624) possibly is significantly overestimated: while Husser et al. (2020) adopted [Fe/H] $= -0.36$ dex from the compilation of Dias et al. (2016), high-resolution spectra provide [Fe/H] $= -0.69 \pm 0.06$ dex for this cluster (Valenti et al. 2011).

The error on the individual [Fe/H] measure was estimated computing the quadratic sum of the propagated uncertainty and the root mean square of Equation 4.3 (see Husser et al. 2020 for details). Considering the assumed $S/N$ ratio cut, the median uncertainty on the individual [Fe/H] measure turns out $\sim 0.15$ dex.

The magnitude of the HB was estimated as the mean value of the stars observed along this evolutionary sequence in the differentially reddening corrected (DRC) CMD. In the case of NGC 6569, for which only magnitudes in the F555W filter were available, we converted the measured magnitude difference into the F606W filter by using PARSEC isochrones (Bressan et al. 2012) computed considering the cluster parameters obtained by Saracino et al. (2019). We have verified that the derived metallicity distribution remains unchanged even if the $V - V_{\rm HB}$ magnitude differences are computed in the F555W filter.

## 4.4 Results and discussion

### 4.4.1 Validation benchmarks

As mentioned, before estimating the metallicity distribution of Liller 1 and Terzan 5, we tested the validity of the method in a metallicity regime suitable for bulge star clusters. To this purpose, we first analyzed the selected benchmark GCs (NGC 6569, NGC 6440 and NGC 6528), for which high-resolution spectroscopic values of [Fe/H] are available and can thus be compared with those obtained from Equation 4.3.

As discussed in Section 4.3, we considered as bona fide targets for the metallicity analysis only the stars with $S/N \geq 15$. Moreover, we excluded saturated objects in the F606W filter, since Equation 4.3 requires reliable measures of the star magnitude in this band. This selection led to a final sample of 108 stars for NGC 6569, 100 stars for NGC 6440 and 199 stars for NGC 6528. The metallicity distributions derived for each cluster are shown in the left panels of Figures 4.4, 4.5 and 4.6, together with the locations of the adopted star samples in the PM-selected and DRC CMD, which are provided in the right panels.

As can be seen, the derived metallicity distributions are fully compatible with a single peak component in all the three reference clusters. This is also confirmed by the Gaussian mixture model (GMM) statistics, computed by using the scikit-learn python package (Pedregosa et al. 2011). We let the code free to explore from one to four components during the fit to the derived metallicity distributions. In all the cases, both the Bayesian

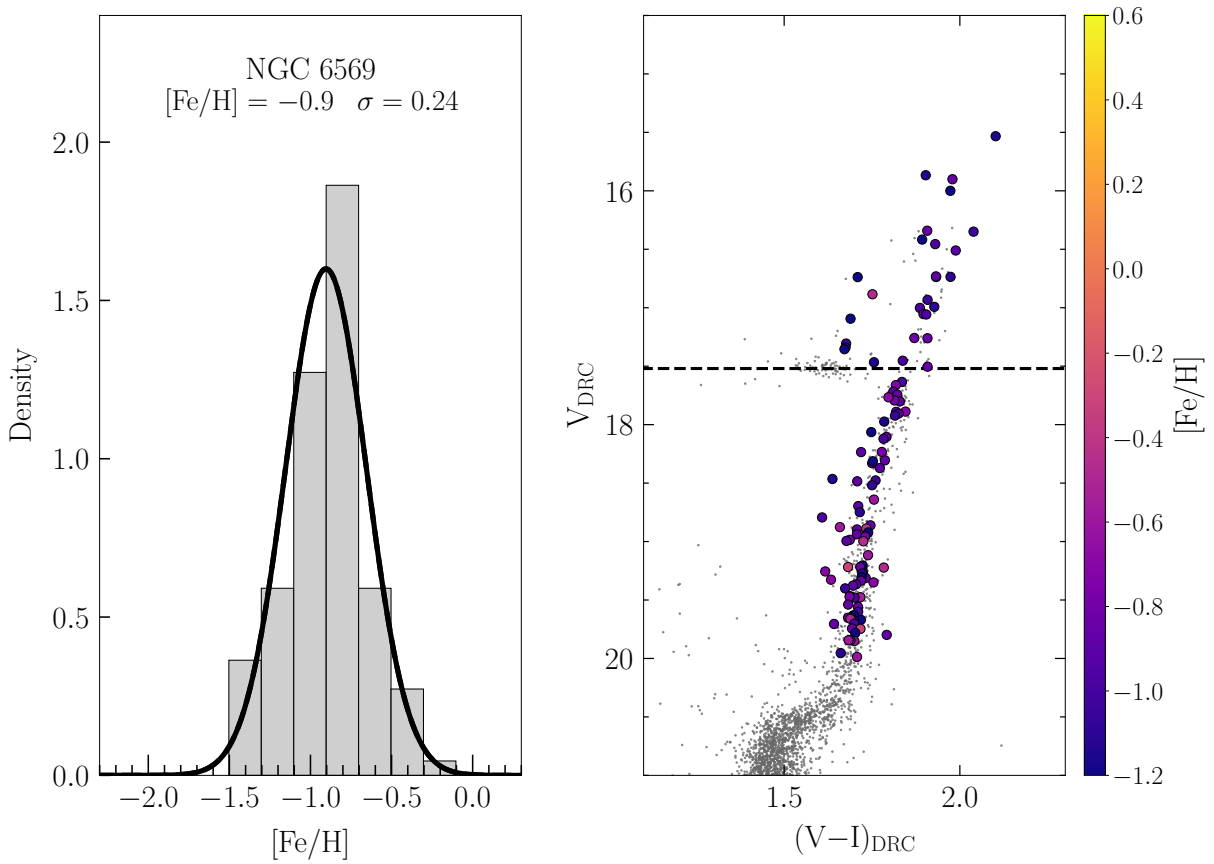


**Figure 4.4:** *Left panel*: Metallicity distribution of NGC 6569 (grey histogram) and its best-fit Gaussian solution (black line). The distribution is normalized such that the total area of the histogram equals 1. The mean [Fe/H] value and the standard deviation derived from the Gaussian fit are also labelled in the panel. *Right panel*: PM selected and DRC CMD of NGC 6569 (grey dots) from the photometric catalog of Saracino et al. (2019). The stars for which the metallicity has been measured are plotted as large circles colored according to their [Fe/H] value (see the color bar on the right). The black dashed line marks the adopted magnitude level of the HB ($V_{\rm HB} = 17.52$).

(BIC) and the Akaike (AIC) information criteria gave as best result a single component. In addition, for all our benchmark clusters, we obtained a metallicity determination nicely in agreement with the literature values. Specifically, for NGC 6569 we obtained [Fe/H] = −0.9 dex, with a dispersion $\sigma = 0.24$. This value is in good agreement with high-resolution spectroscopic determinations, which range from [Fe/H] = −0.87 dex (Johnson et al. 2018) to [Fe/H] = −0.79 dex (Valenti et al. 2011). In the case of NGC 6440, we find that the mean of the distribution is equal to [Fe/H] = −0.53 dex, with $\sigma = 0.2$, which is in excellent agreement with high-resolution spectroscopy studies: [Fe/H] = −0.5 dex (Muñoz et al. 2017), [Fe/H] = −0.56 dex (Origlia et al. 2008). Finally, for NGC 6528 we find a mean value of [Fe/H] = −0.23 dex with $\sigma = 0.19$. Taking into account the (large) dispersion of the distribution, we conclude that also in this case the derived value is in satisfactory agreement with previous measures from high-resolution spectra: Muñoz et al. (2018) and Origlia et al. (2005) quote [Fe/H] = −0.2 dex and [Fe/H] = −0.17 dex, respectively, and Schiavon et al. (2017) obtained a value of [Fe/H] ∼ −0.2 dex from two APOGEE (Majewski et al. 2017) stars.

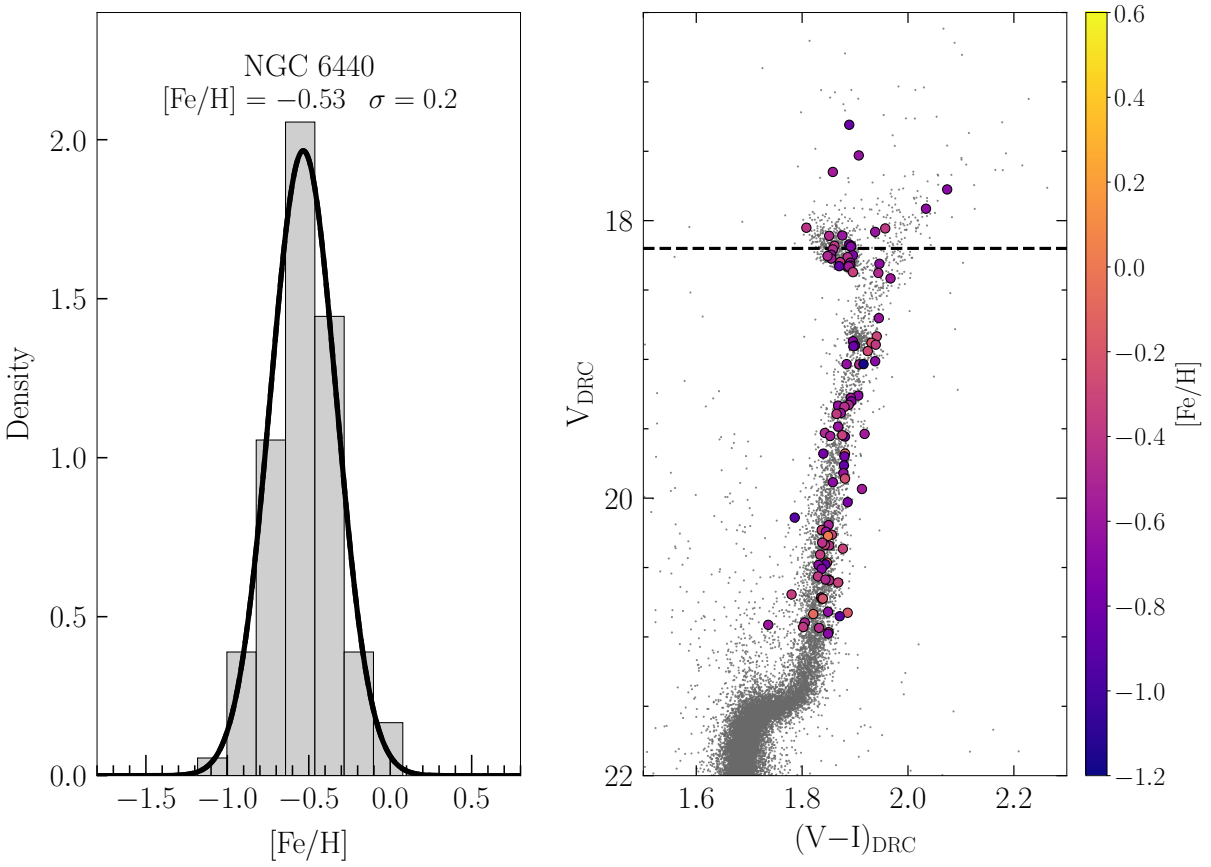


**Figure 4.5:** As in Figure 4.4, but for NGC 6440. Here we considered the photometric catalog presented in Pallanca et al. (2021a) and we assumed $V_{\rm HB} = 18.2$.

Thus, the first results of this analysis are that the approach proposed by Husser et al. (2020) to determine the metal content of star clusters from the CaT lines, and the linear calibration shown in Equation 4.3 hold also in the high-metallicity regime typical of bulge GCs, yielding iron distributions fully in agreement with the literature.

### 4.4.2 Liller 1

To determine the metallicity distribution of Liller 1, we selected the stars according to the criteria described in Section 4.4.1 and we further excluded spectra of extremely cool objects, with colors $(I - K) \geq 7.5$ (see Figure 4.7), because strong TiO molecular bands fall in the CaT wavelenght range. After this selection, the final sample counts 64 stars. The positions of these objects in the PM-selected and DRC optical $(V, V - I)$ and hybrid $(I, I - K)$ CMDs are shown in Figure 4.7, where the points are color coded on the basis of their derived metallicity. As apparent, at odds with what found for the benchmark GCs, a significant iron spread is already appreciable from this plot.

Figure 4.8 shows the obtained metallicity distribution. In spite of the same $S/N$ cut and the same bin size, the histogram of Liller 1 is clearly different from those presented in Section 4.4.1 for the three reference clusters, showing a clear bimodality, with at least 14 stars having supersolar metallicity. To statistically verify the multi-modality of the iron distribution of Liller 1, we run the GMM code letting it free to assess the

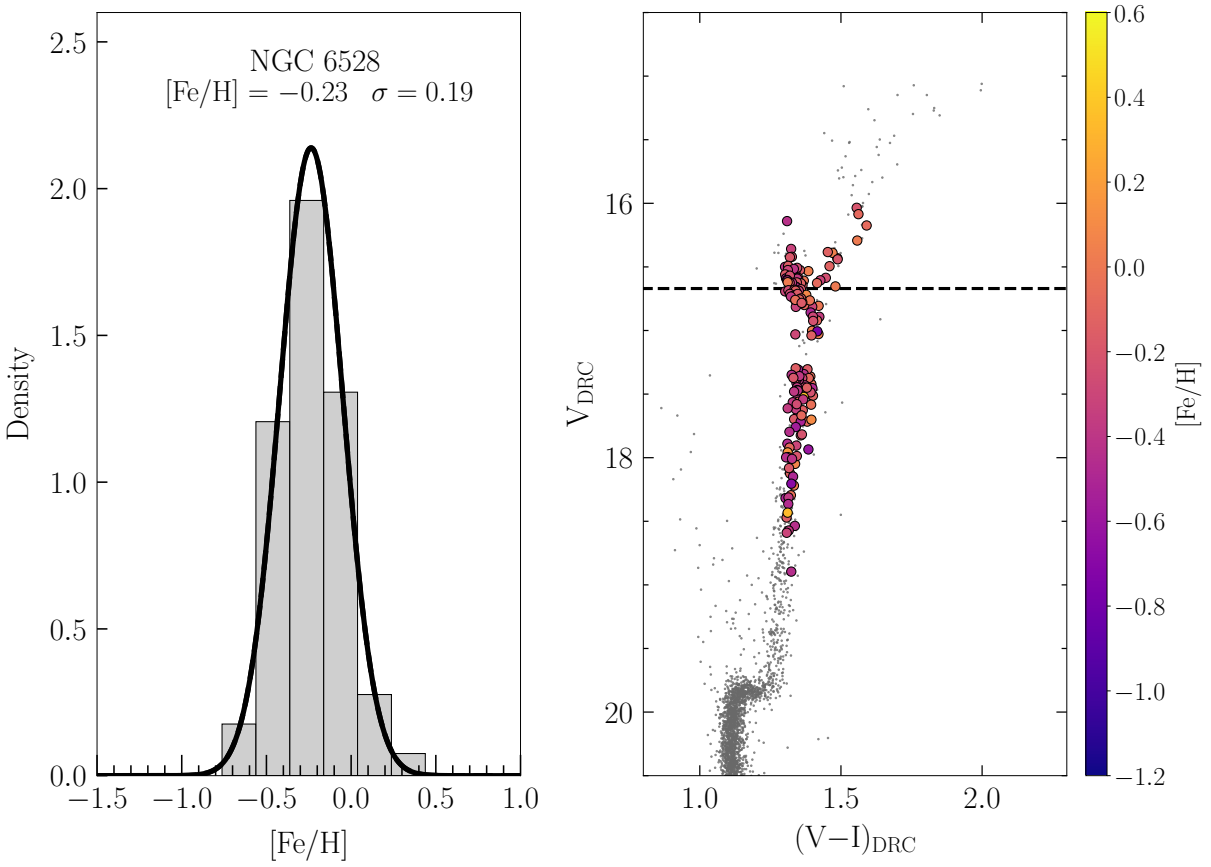


**Figure 4.6:** As in Figure 4.4, but for NGC 6528. Here we considered the photometric catalog presented in Lagioia et al. (2014) and we assumed $V_{\rm HB} = 16.7$.

number of components. Indeed, both the BIC and the AIC analysis give the best result for two Gaussian components. Considering the mean values and dispersions obtained from the GMM, the two peaks correspond to [Fe/H] $= -0.48$ dex (with $\sigma = 0.22$) and [Fe/H] $= +0.26$ dex (with $\sigma = 0.17$). The two components that reproduce the overall shape of the iron distribution of Liller 1 are shown with different colors in Figure 4.8. This is the first spectroscopic confirmation of a supersolar stellar population in Liller 1, as strongly suggested by the photometric analysis presented in the previous chapters of this thesis. We emphasize that a bimodal distribution is found also if the quadratic calibration of Husser et al. (2020) is adopted, in place of the linear one. The only variations are that both the MR and the metal-poor (MP) components show a larger dispersion, and the MR peak is found at [Fe/H] $\simeq 1$ dex (indeed, such an unrealistically high value of iron abundance further suggests that the linear calibration is the most appropriate choice in the high-metallicity regime; see the discussion in Section 4.3).

We checked for possible spurious effects that could have artificially generated the MR peak observed in Figure 4.8. First, we noted that the vast majority (12 out of 14) of the identified supersolar stars have both RV and PM measurements, thus guaranteeing their membership to Liller 1. This is also supported by their radial distribution. The modelling of the observed metallicity distribution with the two Gaussian components discussed above allows us to assign to each star a probability of belonging to the subsolar or to the supersolar component. With this additional information we can probe the spatial

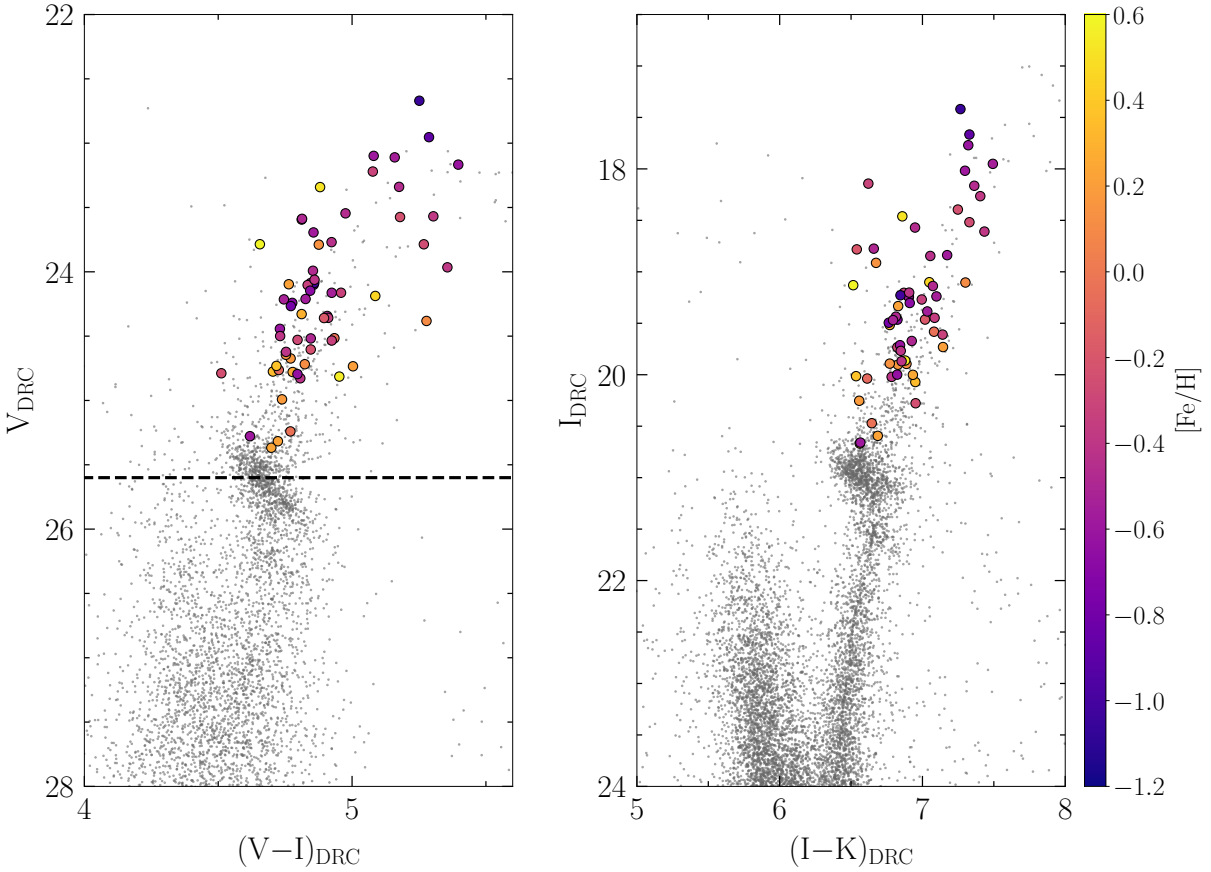


**Figure 4.7:** PM-selected and DRC optical and hybrid CMDs of Liller 1 (black dots) from the photometric catalog presented in Ferraro et al. (2021). The stars with measured metallicity are plotted as circles colored according to their [Fe/H] (see the color bar on the right). The black dashed line in the left panel marks the adopted HB level optical magnitude ($V_{HB} = 25.6$).

distribution of the stars belonging to the two populations. Very interestingly, we find that stars with a probability larger than 0.5 to belong to the supersolar component appear more centrally concentrated than the subsolar population. This is shown in Figure 4.9, where the difference between the two distribution is clearly distinguishable also by eyes. The cumulative radial distributions of the two components fully confirm this indication, and allow us to evaluate the statistical significance of the difference. The Kolmogorov-Smirnov test applied to the two components shows that the probability that they are extracted from the same parent distribution is essentially zero (p=0.000), indicating that the two distributions are different at more than $5\sigma$ of statistical significance.

We also verified the absence of trends with the differential reddening value used to correct the F606W magnitudes that enter Equation 4.2. In fact, Liller 1 is one of the most extincted bulge stellar clusters, with an average $E(B-V) = 4.52 \pm 0.10$ and a maximum variation of reddening of $\delta E(B-V) \sim 0.9$ due to highly spatially variable interstellar extinction in its direction (Pallanca et al. 2021b). This phenomenon heavily affects magnitudes, especially in the optical bands. Figure 4.10 demonstrates that there is no trend between $\delta E(B-V)$ and the derived metallicity values. This is also confirmed by the Pearson coefficient which turns out to be $\sim -0.2$, thus confirming the absence of correlations among the two quantities. Thus, we can safely exclude that the MR component

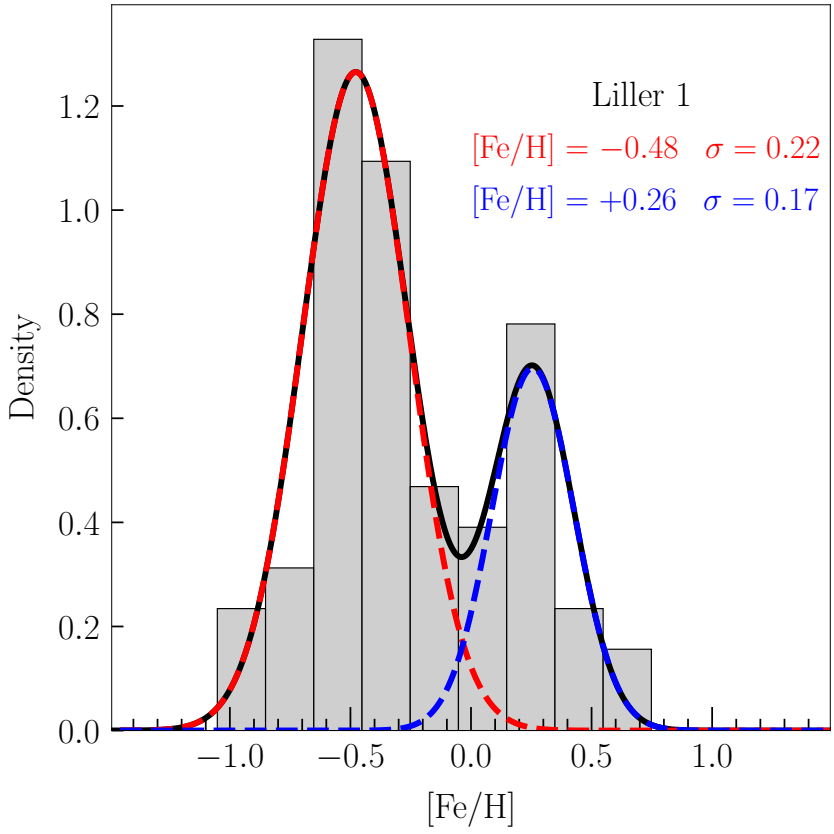


**Figure 4.8:** Metallicity distribution of Liller 1 bona-fide targets (grey histogram). The solid black line shows the function that best reproduces the observed distribution. It is the combination of the two Gaussian functions shown as red and blue dashed lines and indicating the presence, respectively, of a MP and a MR subpopulations in Liller 1. The mean [Fe/H] values and the standard deviations of the two individual Gaussian components are also labelled in the panel.

is due to any bias in the measures.

### 4.4.3 Terzan 5

To built the MUSE metallicity distribution of Terzan 5, we followed the prescriptions discussed in the previous sections. To summarize, we selected stars with $S/N \geq 15$ as calculated by PampelMuse. Among these objects, we retained likely member stars with RV within $2.5\,\sigma$ with respect to the cluster system velocity (specifically, $-110\,\mathrm{km\ s^{-1}} < \mathrm{RV} < -55\,\mathrm{km\ s^{-1}}$) and PM compatible with the cluster (Massari et al. 2015). Moreover, we excluded stars with $V_{\mathrm{DRC}} < 19$, which corresponds to the saturation limit of the utilized HST images. This magnitude cut is also a conservative choice to avoid bright spectroscopic targets likely affected by TiO molecular bands, which, as already mentioned in the previous paragraph, alter the shape of the spectrum in the CaT wavelength range. Following this selection, the bona fide sample counts 265 stars, among which at least 18 objects with supersolar metallicity (i.e., measured [Fe/H] greater than 0.1). The optical, DRC corrected and PM-cleaned CMD composed of these objects is shown in the right panel of Figure 4.11, where the spectroscopic targets are color-coded by the measured [Fe/H]. The black dashed line marks the adopted $V_{\mathrm{HB}}$ level, equal to $V_{\mathrm{HB}} = 21.2$.

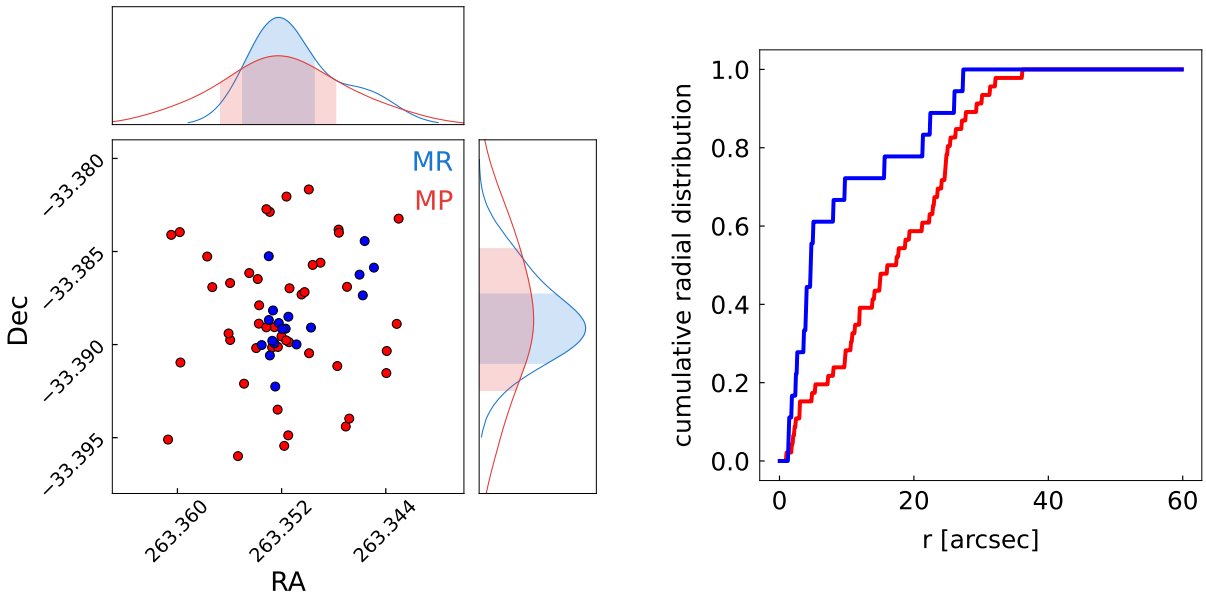


**Figure 4.9:** *Left panel:* Spatial distribution of the stars with measured metallicity in Liller 1. The red circles mark the stars with a probability $\geq 0.5$ to belong to the MP component, the blue circles are those with a probability $\geq 0.5$ to belong to the MR subpopulation. The projected 1D distributions of the two sub-samples, along the right ascension and the declination directions, are shown in the top and right side panels, respectively, with the shaded areas corresponding to the $1\sigma$ confidence level of the distributions. *Righ panel:* Cumulative radial distributions of the MP (red line) and the MR (blue line) subpopulations of Liller 1.

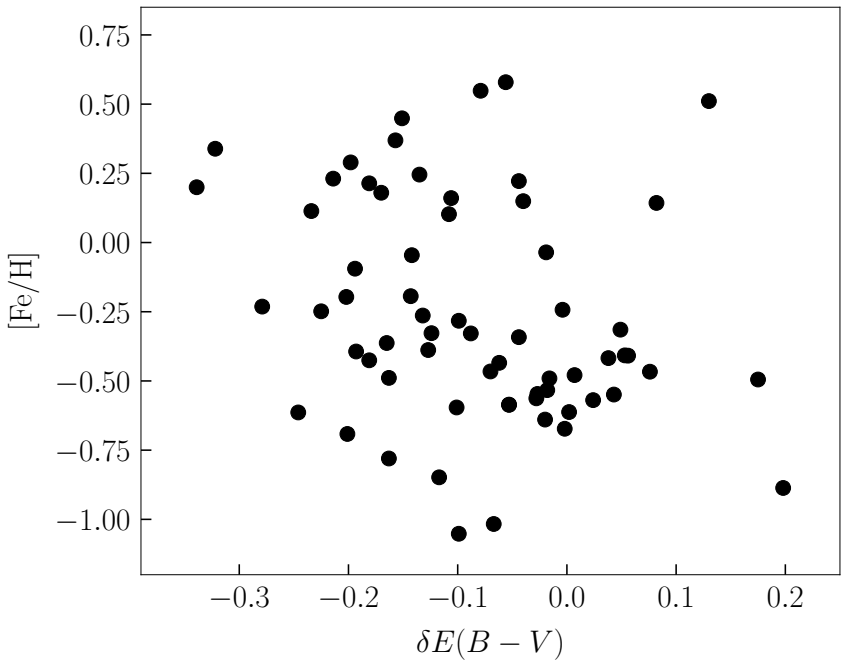


**Figure 4.10:** Measured values of [Fe/H] as a function the differential color excess $\delta E(B-V)$ (from Pallanca et al. 2021b) used to build the DRC CMD of Liller 1.

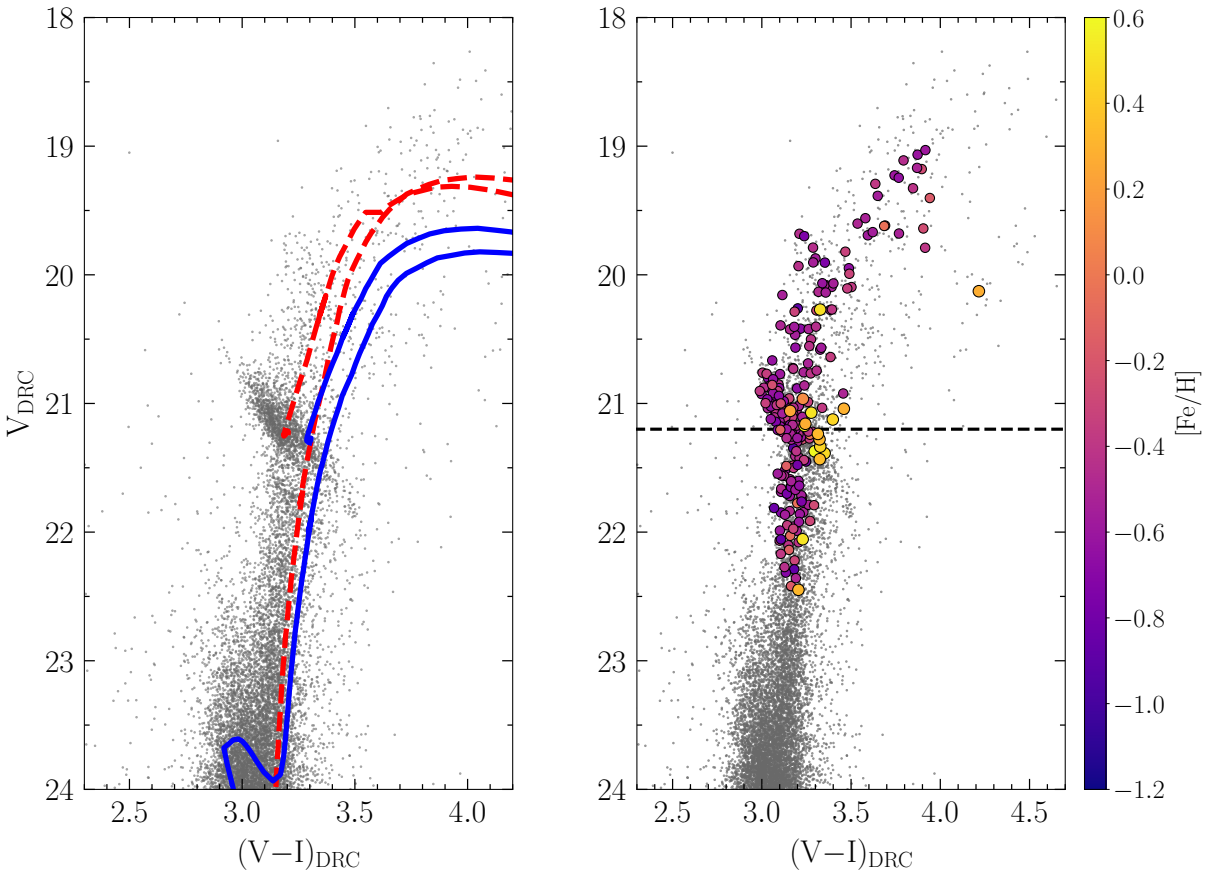


**Figure 4.11:** PM-selected and DRC optical CMD of Terzan 5 (grey dots) from the photometric catalog presented in Massari et al. (2015). In the right panel, the stars with measured metallicity are plotted as circles colored according to their [Fe/H] (see the color bar on the right). The black dashed line in the left panel marks the adopted HB level optical magnitude ($V_{HB} = 21.2$). In the left panel, we overlay on the CMD two isochrones corresponding to $t = 12$ Gyr with [M/H] $= -0.2$ (red dashed line), and $t = 4.5$ Gyr with [M/H] $= +0.3$ (blue solid line). The distance modulus is equal to $\mu = 13.87$ (from Valenti et al. 2007), while the adopted $E(B-V)$ is equal to 2.3.

The first remarkable difference with respect to Liller 1 is that we were able to extract spectra not only for stars along the bright part of the RGB, but also for objects tracing the double RC and the fainter RGB. This is due to the fact that the overall $S/N$ ratio is higher, since the extinction in the direction of Terzan 5 ($E(B-V) = 2.38$, Valenti et al. 2007) is slightly less extreme with respect to the case of Liller 1. To guide the eye, in the left panel of the same figure we display two isochrones representing an old and subsolar stellar population (red dashed line), and a young and supersolar one (blue solid line). These models were calculated according to the fit presented in Ferraro et al. (2016), considering an age of 12 Gyr and a global metallicity of [M/H] $= -0.2$ dex for the old stars, and an age of 4.5 Gyr and [M/H] $= +0.3$ dex for the young ones. As visible from Figure 4.11, the measured MR stars (orange and yellow points) occupy the region of the CMD predicted by the young and supersolar stellar model. Specifically, as expected, we detect the majority of the supersolar (and younger) objects in the He-burning phase, because of the rapid evolution of such young stars in other evolutionary phases. It is

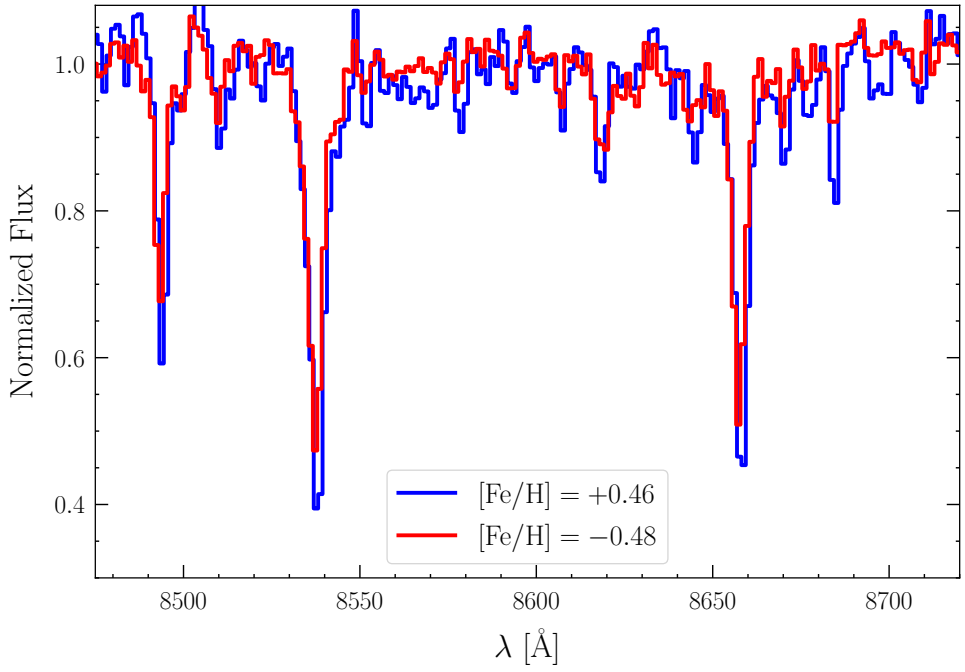


**Figure 4.12:** Examples of two normalized spectra of member stars of Terzan 5 belonging to the metal-poor (red line) and metal-rich (blue line) RC.

worth of emphasizing that the MR stars nicely trace *only* the RC predicted by the young and metal-rich isochrone. However, to reinforce this result, in Figure 4.12 we show two normalized spectra with comparable $S/N$ representing a randomly extracted star from the subsolar (red spectrum, $S/N = 20$) and supersolar (blue spectrum, $S/N = 22$) RC. As can be seen from the direct comparison, the MR star shows deeper chemical features along all the wavelength range of interest. These evidences represent a solid confirmation that the adopted methodology and calibration relation success in detecting supersolar cluster stars, validating the results presented for Liller 1. Indeed, it is worth of recalling that, at the moment, no other metallicity distributions for Liller 1 are available in the literature.

The histogram representing the obtained metallicity distribution, built considering a bin size of 0.15 dex, is shown in Figure 4.13. Following the same procedure adopted for the benchmark cases and for Liller 1, we exploited the GMM statistics to infer the most likely number of Gaussian components that describe the overall distribution. The GMM algorithm returned as the best result two components: a subsolar peak, corresponding to a mean metallicity of $[\mathrm{Fe/H}] = -0.5$ dex (with $\sigma = 0.15$), and a supersolar one, with mean $[\mathrm{Fe/H}] = +0.33$ dex (with $\sigma = 0.19$). The two different components are highlighted by different colors in Figure 4.13.

The mean metallicity obtained via MUSE spectra for the MP peak of Terzan 5 is perfectly equal to the one retrieved for Liller 1, adding further evidence to the kinship between these two stellar systems. However, this metallicity measure of the MP population results more metal-poor with respect to previous spectroscopic studies based on high-resolution data sets, which report a value of $[\mathrm{Fe/H}] \sim -0.3$ dex (Origlia et al. 2011; Massari et al. 2014). On the other hand, the measurement obtained for the MR population is perfectly in agreement with the aforementioned studies, which quote a value of $[\mathrm{Fe/H}] \sim$

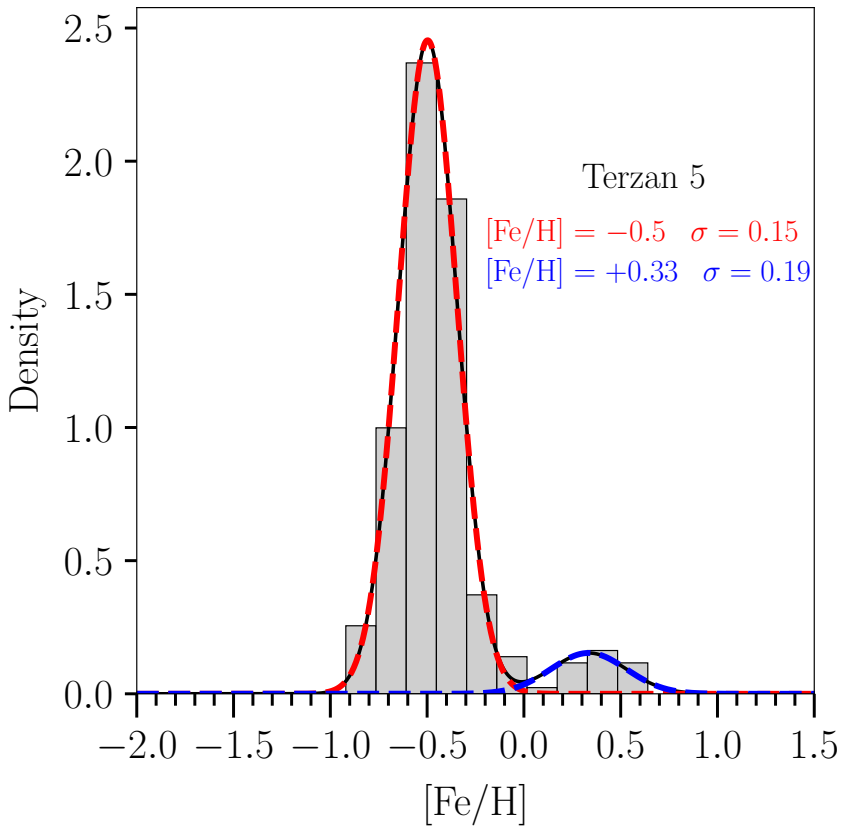


**Figure 4.13:** Metallicity distribution of Terzan 5 bona-fide targets (grey histogram). The solid black line shows the function that best reproduces the observed distribution. Also in this case, the number of Gaussian components from the GMM that best reproduces the distribution is two, shown as red and blue dashed lines, marking the MP and a MR peak of Terzan 5. The mean [Fe/H] values and the standard deviations of the two individual Gaussian components are also labelled in the panel.

+0.3 dex. This result definitively demonstrates that the extrapolation in the supersolar regime of the relation proposed by Husser et al. (2020) safely works, as corroborated by the comparison with high-resolution spectroscopic studies. We also stress here that the relative small number of MR stars is a direct symptom of the external area mapped by our MUSE observations. In fact, it has been already shown that MR stars are more centrally concentrated with respect to the MP population (Massari et al. 2014).

We compared our sample to the high-resolution one (hereafter, HR sample) presented in Massari et al. (2014). In this study, the authors determined the metallicity distribution of Terzan 5 by using a sample of 137 optical high-resolution spectra ($R \sim 16,200$) of bright RGB stars ($V_{\rm DRC} \leq 21.1$) acquired with FLAMES at the VLT. From their catalog, which contains member stars selected on the basis of RVs, we considered only the objects in the radial range that overlaps our observations, that is $55'' < r < 110''$ from the cluster center. Following this selection, the HR sample counts a total of 45 stars. Moreover, we recall that the authors adopted the same magnitude cut ($V_{\rm DRC} \sim 19$) for excluding bright and cool objects affected by TiO contamination. We show the direct comparison between the MUSE and the HR sample distributions in the upper panel of Figure 4.14 (blue and orange histogram, respectively). As can be seen, the peak of the MUSE distribution is shifted

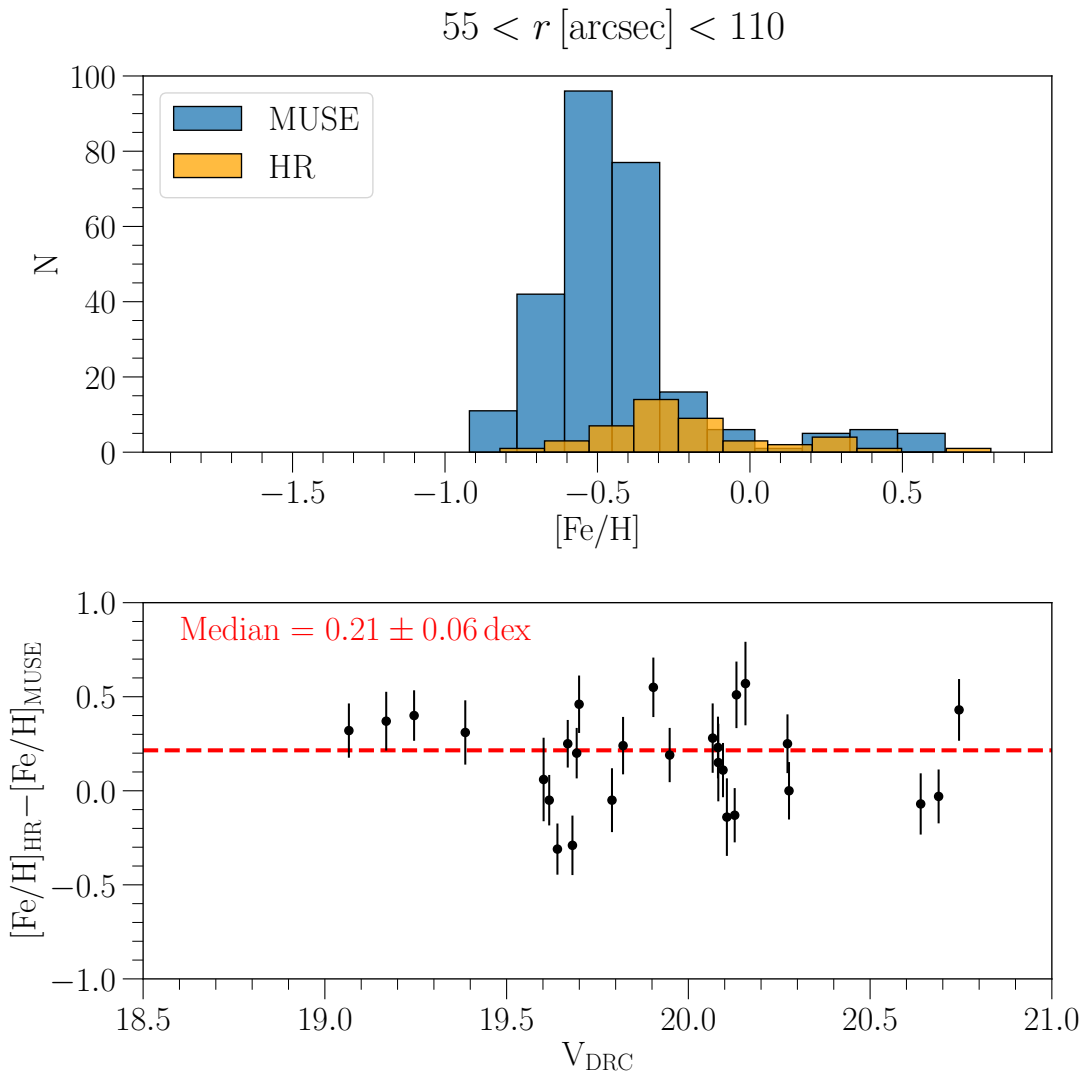


**Figure 4.14:** *Upper panel:* Comparison between the metallicity distribution obtained via MUSE (blue histogram, this work) and high-resolution (HR) FLAMES spectra (orange histogram, Massari et al. 2014) of stars included in the $55'' < r < 100''$ radial range. *Lower panel:* Distribution of the difference between the iron measurements of Massari et al. (2014) ($[Fe/H]_{HR}$) and this work ($[Fe/H]_{MUSE}$), as a function of the differenetial reddening corrected $V$ magnitudes. Only member stars, according to the RV and PM criteria, are shown in the plot. The dashed red line represents the median value of the distribution, and its value is labelled in the panel.

towards lower metallicities. Nevertheless, the HR distribution can be still considered within the dispersion of the MUSE one. To actually compute the offset between the two data sets, we cross-matched the two catalogs and we calculated the difference between the two iron measurements. We considered only the objects satisfying our RV and PM requirements, for a total of 38 common stars. As shown in the lower panel of Figure 4.14, we determined the offset by calculating the median of these data points, confirming a shift of $\sim 0.2$ dex between the two old populations. Among the stars in common, we found a supersolar target (with $[Fe/H] = +0.27 \pm 0.12$ from the CaT EW) in perfect agreement with the HR measure ($[Fe/H] = +0.14 \pm 0.08$), further confirming the validity of this method in the supersolar metallicity regime.

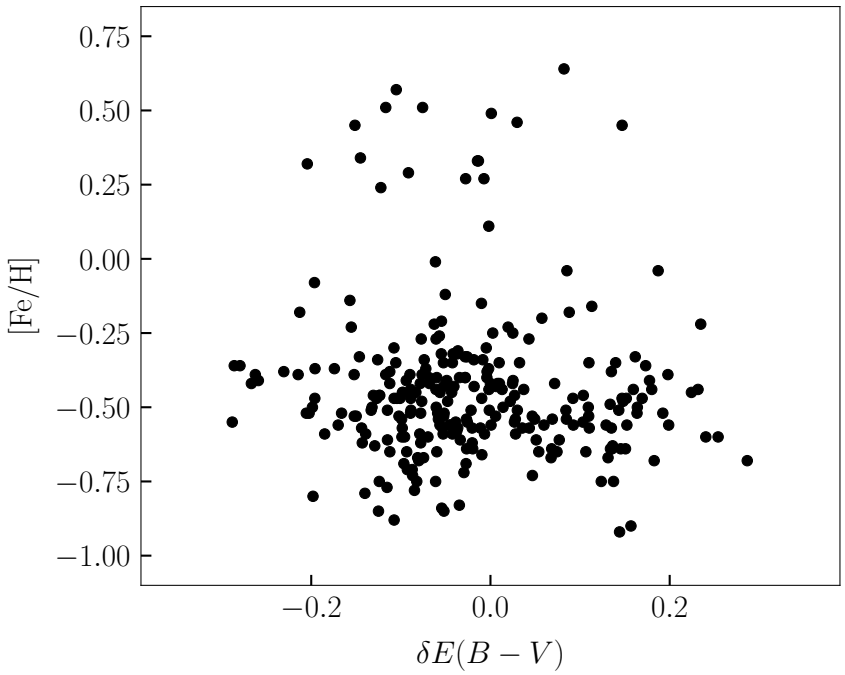


**Figure 4.15:** Measured values of [Fe/H] of Terzan 5 stars as a function of the differential color excess $\delta E(B-V)$ (from Massari et al. 2012) used to build the DRC CMD.

We detect a higher absolute number of MR objects in this radial range, counting 21 stars with a probability larger than 50% to belong to the supersolar peak, compared to 9 MR stars of the HR sample. On the other hand, as also visible from the histograms, the percentage of MR stars with respect to the total number of object is lower in the MUSE distribution: we find that, in our catalog, the $\sim 8\%$ of the total sample is represented by the MR peak, while the fraction increases to the 18% in the HR sample. Indeed, if we focus on the bright portion of the RGB ($V_{\rm DRC} \leq 20.7$) of Figure 4.11 - where all the spectroscopic targets of Massari et al. (2014) are placed - we detect only 2 stars in the same magnitude range. However, the lower statistics in the catalog of Massari et al. (2014), coupled a residual contamination from field stars, could be at the basis of this discrepancy. Nonetheless, we confirm the presence of genuine MR member stars even at such large radii from the cluster center.

Finally, we checked if observational effects, related to the differential reddening corrections used in this analysis, could have biased the resulting metallicity distribution, with particular attention to the supersolar population. As in the case of Liller 1, also Terzan 5 suffers from a remarkable variable extinction in its direction, as shown in Section 2.2.2. Here, we used the differential reddening corrections of Massari et al. (2012), who calculated a maximum variation of $E(B-V)$ equal to $\sim 0.7$ mag. In Figure 4.15, we confirm the absence of trends among $\delta E(B-V)$ and the derived [Fe/H] measures. To statistically prove this, we performed once again the Pearson test on the MP and MR population: we obtained $-0.05$ and 0.16 respectively, demonstrating that no trend exists between the two quantities.

## 4.5 Summary

In this chapter we present the first chemical analysis of the Bulge Fossil Fragments Liller 1 and Terzan 5 by means of an IFS facility, specifically MUSE at the VLT. On the one hand, this study provided the first spectroscopic metallicity distribution ever obtained for the stellar system Liller 1, which has been determined from the analysis of MUSE spectra of 64 individual member stars. On the other hand, thanks to the blind selection of the spectroscopic targets, we performed the first unbiased metallicity distribution of Terzan 5, measuring the [Fe/H] abundance for 265 member stars covering the entire extension of the RGB and the RC of the cluster.

The determination of stars' metallicity was performed through the measure of the EW of the CaT lines following the prescriptions described in Husser et al. (2020). These authors presented three relations linking the CaT EW to [Fe/H], obtained from linear, quadratic, and cubic fits to the data provided by their calibration sample (19 Galactic GCs from Dias et al., 2016). However, since the MR regime is poorly represented in that sample[21], to avoid hazardous extrapolations we have adopted their linear calibration (see Equation 4.3). Then, to test its validity in the high metallicity regime, as a sanity check, we first determined the iron distribution of three reference bulge GCs of known metallicity (namely NGC 6569, NGC 6440, and NGC 6528). In all cases we found unimodal distributions peaked at a mean iron abundance that is fully consistent with the spectroscopic values reported in the literature.

The application of the same methodology to Liller 1 yielded, instead, a completely different result: a clear bimodal iron distribution is obtained, with a main peak at [Fe/H] $\sim -0.5$ dex and a secondary peak at [Fe/H] $\sim +0.3$ dex. Indeed, both the BIC and the AIC analyses confirm that the overall distribution is best represented by a combination of two Gaussian components. The metallicity of the MP population is fully consistent with the value quoted by Origlia et al. (2002) ([Fe/H] $= -0.3 \pm 0.2$ dex), while the secondary peak detected here is the first spectroscopic confirmation of the presence of a supersolar stellar population in Liller 1. This finding is in perfect agreement with what suggested by the photometric analyses presented in Chapter 2 and Chapter 3. In addition, because the analyzed MUSE pointing covers the internal region of this cluster (see the right panel of Figure 4.1), we proved that the supersolar stars are more centrally concentrated than the subsolar ones, validating the preliminary photometric indications (Section 2.1.5). Interestingly, this finding is strikingly similar to what previously found in Terzan 5 (Ferraro et al. 2009; Lanzoni et al. 2010). Indeed, the two main components of the metallicity distribution of Terzan 5 share exactly the same behavior, with the MR population being more centrally segregated than the metal poor one (see Section 1.2.3).

A bimodal iron distribution is also found applying the same procedure to Terzan 5. We detect a subsolar, main peak at [Fe/H] $\sim -0.5$ dex, and a supersolar minor component at [Fe/H] $\sim +0.33$ dex. While the MR peak is nicely in agreement with previous high-

[21] Specifically, four GCs are considered in the metallicity regime of interest for this study, namely NGC 104, NGC 6388, NGC 6441 and NGC 6624. Excluding NGC 6624, for which high-resolution spectroscopic measurements disagree with the metallicity value derived in Dias et al. (2016), the MR sample considered by Dias et al. (2016) spans a metallicity range from $\sim -0.7$ dex up to $\sim -0.5$ dex.

resolution spectroscopic studies (Origlia et al. 2011; Massari et al. 2014), the MP one results more metal-poor, with an overall shift of 0.2 dex. Considering the intrinsic dispersion of this distribution, we can confirm a satisfactory agreement with high-resolution determinations. However, this evidence suggests that the linear relation of Husser et al. (2020), while notably working in the supersolar regime, still needs proper constraints in the metallicity range covered by the most metal-rich bulge stellar clusters. It is worth of emphasizing that this methodology led us to measure unbiased number fractions of the MP and the MR component within the radial range of our study ($50'' < r < 110''$), showing that at least the 8% of the total sample is composed of MR stars within this external region. We also note that the metallicity distribution of Terzan 5 obtained in Section 3.4, through the technique for reconstructing the star formation history via CMD fitting, is in perfect agreement with the one obtained here. This fact can suggest an intrinsic offset and dispersion, with respect to the high-resolution measurements, when dealing with photometry-based methodologies.

This chapter is based on the results presented in

Crociati et al. (2023)

Crociati et al. (2024, in prep.)

# 5 Conclusions

The formation of galaxy bulges is currently highly debated in the literature: several different mechanisms, ranging from dissipative collapse, to dynamical secular evolution of unstable discs and merging/coalescence of primordial substructures, have been proposed (e.g., Combes et al. 1990; Immeli et al. 2004b; Elmegreen et al. 2009). On the other hand, the detection of the so-called "clumpy" or "chain galaxies" observed at high-redshift (for example, Carollo et al. 2007; Elmegreen et al. 2009) suggests that the coalescence of primordial substructures is a promising channel that could have played a relevant role in the assembling process of galactic spheroids. Indeed, numerical simulations (e.g., Immeli et al. 2004b; Elmegreen et al. 2008; Bournaud & Elmegreen 2009; Bournaud 2016; Dekel et al. 2023) have shown that primordial massive clumps (with masses of $10^{7-9} M_{\odot}$) can form from violent disk instabilities and eventually migrate to the centre and dissipatively coalesce generating the bulge. The same simulations also show that, while the majority of such primordial clumps coalesces to form the bulge, a few of them can survive the total disruption and be still present in the inner regions of the host galaxy, roughly appearing as massive GCs. At odds with genuine GCs, however, these fossil relics are expected to host multi-iron and multi-age subpopulations, because their progenitors were massive enough to retain the iron-enriched ejecta of supernova explosions and likely experienced multiple bursts of star formation. This scenario should hold also for the formation of the Milky Way spheroid and, intriguingly, two peculiar stellar systems promising to be the fossil records of this hierarchical assembly process have been discovered in our Galaxy: the bulge stellar systems Terzan 5 and Liller 1.

## 5.1 The emerging scenario: a new class of objects

The properties of the old stellar populations observed in Liller 1 and Terzan 5 demonstrate a concurrent genesis of these two systems, collocating them at the early epoch of the Galaxy assembly. The discovery (Helmi et al. 2018; Massari et al. 2018) of an increasing number of stellar streams, interpreted as the relics of cannibalism events experienced by the Milky Way in its past history, may suggest that Terzan 5 and Liller 1 are nuclear star clusters of massive satellites accreted after the epoch of the Galaxy formation. However, the abundance patterns observed for the old stellar population in Terzan 5 clearly indicate that it formed from a high metallicity (half-solar) cloud enriched exclusively by the ejecta of CC-SNe. This chemical signature is strikingly similar to that observed for the bulge field stars and, in fact, it is typical of massive and dense environments that experienced star

formation at very high rates, as the bulge and the high-z clumps. It therefore seems very unlikely that such an event could occur in a low-mass satellite galaxy, and strongly supports, instead, an in situ origin of Terzan 5. Although the complete chemical characterization (i.e., in terms of $\alpha$-elements) of the old stellar population of Liller 1 is still lacking, its similarity with Terzan 5, in terms of location (the bulge), age, and iron content, strongly supports a common origin for these two systems, and their common link with the Galactic bulge. In fact, a scenario where, just by chance, the Milky Way bulge and the nuclear star clusters of two different satellite galaxies independently followed the same chemical enrichment process and are now all observed in the same region of the Milky Way is, in our view, quite unlikely. Conversely, the age and similarity observed for the old populations in these two systems suggest that both Terzan 5 and Liller 1 are primordial structures that formed in situ from highly metal-enriched gas, as expected in the environment where the proto-bulge assembled.

The differences between the young populations detected in the two systems indicate that the subsequent star formation events were activated and occurred over quite different time-scales, possibly tracing different histories of strong interactions with the local environment or other substructures, also depending on the respective orbits within the Galactic potential. On the other hand, the properties of the young populations, which appear to be more metal-rich and more centrally segregated than the old populations (in agreement with what is expected in a self-enrichment scenario), confirm that these systems were massive enough to retain the SN ejecta. Thus, the combination of the available observational evidence defines these structures as the likely remnants of primordial massive systems that formed in situ and contributed to generate the bulge $\sim 12$ Gyr ago: this can be considered a new class of astrophysical objects, that we named Bulge Fossil Fragments (BFFs).

The detection (e.g., Elmegreen et al. 2009; Shibuya et al. 2016) of similar structures in the star forming regions of high-redshift galaxies confirms that such massive fragments existed at the epoch of the Milky Way assembly. By using the mass-metallicity relation (Mannucci et al. 2009) for galaxies at $z = 3 - 4$, an initial mass of a few $10^9$ $M_\odot$ is expected (Ferraro et al. 2016) for these BFFs. Thus, about ten of such primordial massive structures could have provided the entire mass budget ($\sim 2 \times 10^{10}\, M_\odot$, Valenti et al. 2016) of the Galactic bulge (Hopkins et al. 2012). Most of these structures merged together to form the bulge, but, for a combination of reasons, a few of them survived the total disruption and are now observable as BFFs. In this respect their discovery provides the first observational proof that hierarchical assembly played a role also in the formation of the Galactic bulge. Thus, these findings, on one side reconcile the Milky Way bulge formation process with the observations at high-z, on the other side, they suggest that bulge formation has been more complex than previously thought, with a significant contribution from both the merger of preformed, internally-evolved stellar systems and the formation and secular evolution of the bar and other substructures (e.g., Portail et al. 2017).

In support of this hypothesis, the star formation history of Liller 1 and Terzan 5 suggests that it was characterized by several main bursts combined with a low, but constant, activity of star formation over the entire lifetime of the systems. Therefore, these complex stellar systems unlikely formed through the merger between an old globular cluster and a Giant

Molecular Cloud, as recently proposed by Bastian & Pfeffer (2022). In this respect, it is worth stressing that stellar systems with original stellar masses larger than several $10^6 M_\odot$ are expected (see Bailin & Harris 2009) to be able to retain a fraction of their SN ejecta even without the additional contribution of a dark matter halo, thus providing further support to the self-enrichment scenario. Bastian & Pfeffer (2022) discuss the caveat that massive systems (such as Liller 1 and Terzan 5) in the dense inner Galaxy may be able to capture field stars characterized by a range of metallicities and ages. However, the expected number of captured stars is still small (of the order of a few percent), while the extended SF of Terzan 5 and Liller 1 contributes to more than 30% of their present-day mass. We should also note that the age spread needed to best-fit the old stellar population of Liller 1 is clearly not compatible with the assumption that it was originally a genuine GC. On the same line, the extended duration ($\Delta t \sim 2 - 3$ Gyr) of the young SF event measured in both the systems appears to be hardly compatible with the encounter between a GMC and a massive GC.

The survival of a few BFFs up to now suggests that they evolved in an environment significantly less violent than the forming bulge. Their properties also demonstrate that for several Gyrs they retained a large amount of gas ejected by SN explosions, before producing a new generation of stars. Such bursty star formation histories, with long periods of quiescence, are not rare in the Universe (VandenBerg et al. 2015) and in the Galaxy. In particular, multiple star-formation episodes have been recently found to characterize the star formation history of the Galactic disk (Ruiz-Lara et al. 2020) and Galactic center (Nogueras-Lara et al. 2020), possibly related to gravitational interactions and the accretion of small satellite galaxies (as the Sagittarius dwarf galaxy). The epoch of the young star formation episodes appears to differ from BFF to BFF, for reasons that need to be further investigated, but are possibly related to major interactions with other bulge substructures or the Galactic bar. In this respect, reconstructing the orbit of these systems can bring new crucial information. Such interactions could also be responsible for the severe mass-loss suffered by these structures during their evolution, that significantly reduced their original mass ($\sim 10^{7-9} M_\odot$) to the current value ($\sim 10^6 M_\odot$; Lanzoni et al. 2010; Saracino et al. 2015). The recent discovery that Liller 1 belongs to this class of objects confirms the prediction (Ferraro et al. 2009, 2016) that other surviving remnants could still be hidden in the heavily obscured regions of the Milky Way bulge. Thus, a systematic search for other candidates is crucial in the next years.

## 5.2 Towards a complete comprehension of the Bulge Fossil Fragments

Despite many and important leaps forward in proving the theory of the BFFs, based on the known candidates, some important and decisive interrogatives are still unanswered. First of all, it is still unclear if these systems could manifest a distinctive feature common to all GCs: the presence of anti-correlations between light-elements (such as O, Mg, Al), that is a phenomenon called multiple populations (MPs). Although a commonly accepted theory about the origin of this feature is still lacking, all the scientific community agrees in stating

that MPs are unequivocally linked to the formation and the evolutionary mechanism of *genuine* GCs. Therefore, the detection (or rather the absence) of this phenomenon in the old populations of the BFFs would represent a key discriminant factor in supporting (or discarding) alternative formation scenarios that involve the gravitational capture of external gas by a common old GC. So far, the spectroscopic screenings of Terzan 5 (we would recall the reader that, at the moment, no information about the $\alpha$-elements abundances in Liller 1 is available) provided no evidence of the typical anti-correlation of MPs (Origlia et al. 2011). Yet, this result is not conclusive, since some element spreads are not detected among GCs as metal-rich as Terzan 5 (Pancino et al. 2017), and the typically small number statistic of high-resolution studies aggravates this problem. A new window on the detection of MPs in stellar clusters can be provided by a specific set of infrared photometric filters on board the James Webb Space Telescope (JWST) sensitive to some $\alpha$-elements variation among M-dwarf stars (Cadelano et al. 2023). Clearly, the high number statistic and sensitivity offered by this photometric strategy can overcome the observing limitations that hampered the detection of MPs in Terzan 5 and Liller 1 so far. In this regard, our team recently submitted a JWST observing program aimed at retrieving ultra-deep observations of Terzan 5 with the near-IR camera NIRcam.

In this thesis, we also demonstrated that IFS facilities, even if characterized by a spectral resolution as low as MUSE, provide the ideal primary target list for a detailed high-resolution spectroscopic screening of key chemical elements (iron-peak, $\alpha$-elements, etc.) that are needed for the full reconstruction of the enrichment history of these complex stellar systems. Indeed, the approach adopted in the investigation of Liller 1, strengthened by the remarkable results obtained for Terzan 5, represents a methodological reference benchmark for the study of any additional Bulge Fossil Fragment that will be discovered in the future: it provides an efficient way to determine a preliminary, but meaningful, metallicity distribution, which is able to unveil the presence of multi-iron subpopulations and to provide a list of top-priority targets for follow-up high-resolution spectroscopic investigations. Indeed, it is worth of emphasizing that the combined spectroscopic and photometric search for new Bulge Fossil Fragments is of primary importance to clarify the formation mechanism of our Galaxy. In fact, solid assessing the amount of stellar systems belonging to this new class of objects can provide invaluable pieces of information about the role played by merging processes in the build-up of the Milky Way bulge. In this regard, more and more deep and high-resolution observations of the still unexplored bulge stellar clusters will be available in the near future, thanks to approved HST Treasury Program (GO: 17435) which involves our team and several close collaborators.

Finally, we will soon have the possibility to perform a detailed chemo-kinematical analysis of Liller 1 exploiting the unique capabilities of the IFS ERIS/SPIFFIER at the VLT, the perfect facility (in terms of IR wavelength range, high spatial and spectral resolution) to unveil the origin of its multi-iron stellar populations. In fact, as principal investigator, I secured a set of observations that map the core of this cluster. The statistical robustness of the sample (from the photometric catalog built in Section 2.1.1, we forecast to get the spectra of $\sim 400$ member stars) will enable us to chemically tag the different subpopulations of Liller 1 and to derive, for the first time, accurate and unbiased metallicity [Fe/H] distributions, and abundance patterns [$\alpha$/Fe]. This fact, combined with

the homogeneous mapping of the central region, the large sample, and the available PMs, will let us to construct global and metallicity-based 3D kinematics maps of Liller 1, derive the still lacking central velocity dispersion profile, and detect possible rotation patterns or anisotropy hints, powerful tools to confirm or discard a self-enrichment origin of the metal-rich stars.

# Bibliography


Alonso-García, J., Mateo, M., Sen, B., Banerjee, M., & von Braun, K. 2011, AJ, 141, 146

Alonso-García, J., Minniti, D., Catelan, M., et al. 2017, ApJ, 849, L13

Ambachew, L., Fisher, D. B., Glazebrook, K., et al. 2022, MNRAS, 512, 3079-3097

Anderson, J., & Bedin, L. R. 2010, PASP, 122, 1035

Aparicio, A., & Hidalgo, S. L. 2009, AJ, 138, 558-567

Armandroff, T. E., & Zinn, R. 1988, AJ, 96, 92

Arsenault, R., Madec, P. Y., Hubin, N., et al. 2008, in Society of Photo-Optical Instrumentation Engineers (SPIE) Conference Series, Vol. 7015, Adaptive Optics Systems, ed. N. Hubin, C. E. Max, & P. L. Wizinowich, 701524

Athanassoula, E. 2005, MNRAS, 358, 1477-1488

Babusiaux, C., & Gilmore, G. 2005, MNRAS, 358, 1309-1319

Babusiaux, C., Gómez, A., Hill, V., et al. 2010, A&A, 519, A77

Bailin, J., & Harris, W. E. 2009, ApJ, 695, 1082-1093

Barbuy, B., Bica, E., & Ortolani, S. 1998, A&A, 333, 117-124

Bastian, N., & Pfeffer, J. 2022, MNRAS, 509, 614-618

Baumgardt, H., & Hilker, M. 2018, MNRAS, 478, 1520-1557

Bellini, A., Piotto, G., Bedin, L. R., et al. 2009, A&A, 507, 1393-1408

Bellini, A., Piotto, G., Milone, A. P., et al. 2013, ApJ, 765, 32

Bensby, T., Yee, J. C., Feltzing, S., et al. 2013, A&A, 549, A147

Bensby, T., Feltzing, S., Gould, A., et al. 2017, A&A, 605, A89

Bica, E., Ortolani, S., & Barbuy, B. 2016, , 33, e028

Bonatto, C., Campos, F., & Kepler, S. O. 2013, MNRAS, 435, 263-272

Bournaud, F. 2016, in Astrophysics and Space Science Library, Vol. 418, Galactic Bulges, ed. E. Laurikainen, R. Peletier, & D. Gadotti, 355

Bournaud, F., & Elmegreen, B. G. 2009, ApJ, 694, L158-L161

Bournaud, F., Elmegreen, B. G., & Elmegreen, D. M. 2007, ApJ, 670, 237-248

Bressan, A., Marigo, P., Girardi, L., et al. 2012, MNRAS, 427, 127-145

Cadelano, M., Ferraro, F. R., Istrate, A. G., et al. 2019, ApJ, 875, 25

Cadelano, M., Saracino, S., Dalessandro, E., et al. 2020, ApJ, 895, 54

Cadelano, M., Pallanca, C., Ferraro, F. R., et al. 2015, ApJ, 807, 91

Cadelano, M., Pallanca, C., Dalessandro, E., et al. 2023, A&A, 679, L13

Callingham, T. M., Cautun, M., Deason, A. J., et al. 2022, MNRAS, 513, 4107-4129

Cardelli, J. A., Clayton, G. C., & Mathis, J. S. 1989, ApJ, 345, 245

Carollo, C. M., Scarlata, C., Stiavelli, M., Wyse, R. F. G., & Mayer, L. 2007, ApJ, 658, 960-979

Casagrande, L., & VandenBerg, D. A. 2014, MNRAS, 444, 392-419

Chabrier, G. 2003, ApJ, 586, L133-L136

Chiappini, C., Matteucci, F., & Gratton, R. 1997, ApJ, 477, 765-780

Cignoni, M., & Tosi, M. 2010, Advances in Astronomy, 2010, 158568

Cignoni, M., Sabbi, E., van der Marel, R. P., et al. 2015, ApJ, 811, 76

Claeyssens, A., Adamo, A., Richard, J., et al. 2023, MNRAS, 520, 2180-2203

Clarke, A. J., Debattista, V. P., Nidever, D. L., et al. 2019, MNRAS, 484, 3476-3490

Clarkson, W., Sahu, K., Anderson, J., et al. 2008, ApJ, 684, 1110-1142

Clarkson, W. I., Sahu, K. C., Anderson, J., et al. 2011, ApJ, 735, 37

Combes, F., Debbasch, F., Friedli, D., & Pfenniger, D. 1990, A&A, 233, 82

Crociati, C., Valenti, E., Ferraro, F. R., et al. 2023, ApJ, 951, 17

Dalessandro, E., Ferraro, F. R., Massari, D., et al. 2015, ApJ, 810, 40

Dalessandro, E., Pallanca, C., Ferraro, F. R., et al. 2014, ApJ, 784, L29

Dalessandro, E., Ferraro, F. R., Massari, D., et al. 2013, ApJ, 778, 135

Dalessandro, E., Saracino, S., Origlia, L., et al. 2016, ApJ, 833, 111

Dalessandro, E., Zocchi, A., Varri, A. L., et al. 2018, MNRAS, 474, 2277-2288

Dalessandro, E., Crociati, C., Cignoni, M., et al. 2022, ApJ, 940, 170

Davidge, T. J. 2000, ApJS, 126, 105-126

Debattista, V. P., Ness, M., Gonzalez, O. A., et al. 2017, MNRAS, 469, 1587-1611

Debattista, V. P., Liddicott, D. J., Gonzalez, O. A., et al. 2023, ApJ, 946, 118

Dekel, A., Sari, R., & Ceverino, D. 2009, ApJ, 703, 785-801

Dekel, A., Tziperman, O., Sarkar, K. C., et al. 2023, MNRAS, 521, 4299-4322

Dessauges-Zavadsky, M., Schaerer, D., Cava, A., Mayer, L., & Tamburello, V. 2017, ApJ, 836, L22

Dias, B., Barbuy, B., Saviane, I., et al. 2016, A&A, 590, A9

Dolphin, A. 1997, , 2, 397-409

Dolphin, A. E. 2002, MNRAS, 332, 91-108

Dwek, E., Arendt, R. G., Hauser, M. G., et al. 1995, ApJ, 445, 716

Ellison, S. L., Nair, P., Patton, D. R., et al. 2011, MNRAS, 416, 2182-2192

Elmegreen, B. G., Bournaud, F., & Elmegreen, D. M. 2008, ApJ, 688, 67-77

Elmegreen, D. M., Elmegreen, B. G., Marcus, M. T., et al. 2009, ApJ, 701, 306-329

Erwin, P., Debattista, V. P., & Anderson, S. R. 2023, MNRAS, 524, 3166-3183

Ferraro, F. R., Fusi Pecci, F., & Buonanno, R. 1992, MNRAS, 256, 376-390

Ferraro, F. R., Massari, D., Dalessandro, E., et al. 2016, ApJ, 828, 75

Ferraro, F. R., Pallanca, C., Lanzoni, B., et al. 2015, ApJ, 807, L1

Ferraro, F. R., Sollima, A., Pancino, E., et al. 2004, ApJ, 603, L81-L84

Ferraro, F. R., Sollima, A., Rood, R. T., et al. 2006, ApJ, 638, 433-439

Ferraro, F. R., Dalessandro, E., Mucciarelli, A., et al. 2009, Nature, 462, 483-486

Ferraro, F. R., Lanzoni, B., Raso, S., et al. 2018a, ApJ, 860, 36

Ferraro, F. R., Mucciarelli, A., Lanzoni, B., et al. 2018b, ApJ, 860, 50

—. 2018c, The Messenger, 172, 18-23

Ferraro, F. R., Pallanca, C., Lanzoni, B., et al. 2021, Nature Astronomy, 5, 311-318

Fétick, R. J. L., Fusco, T., Neichel, B., et al. 2019, A&A, 628, A99

Fitzpatrick, E. L. 1999, PASP, 111, 63-75

Foreman-Mackey, D., Farr, W., Sinha, M., et al. 2019, The Journal of Open Source Software, 4, 1864

Fragkoudi, F., Di Matteo, P., Haywood, M., et al. 2017, A&A, 606, A47

Fragkoudi, F., Grand, R. J. J., Pakmor, R., et al. 2020, MNRAS, 494, 5936-5960

Freeman, K., Ness, M., Wylie-de-Boer, E., et al. 2013, MNRAS, 428, 3660-3670

Fritz, T. K., Linden, S. T., Zivick, P., et al. 2017, ApJ, 840, 30

Frogel, J. A., Kuchinski, L. E., & Tiede, G. P. 1995, AJ, 109, 1154

Fukugita, M., Hogan, C. J., & Peebles, P. J. E. 1998, ApJ, 503, 518-530

Gaia Collaboration, Brown, A. G. A., Vallenari, A., et al. 2021, A&A, 650, C3

Gilmore, G., Randich, S., Asplund, M., et al. 2012, The Messenger, 147, 25-31

Girardi, L., Bertelli, G., Bressan, A., et al. 2002, A&A, 391, 195-212

Gonzalez, O. A., Rejkuba, M., Zoccali, M., Valenti, E., & Minniti, D. 2011, A&A, 534, A3

Gonzalez, O. A., Rejkuba, M., Zoccali, M., et al. 2012, A&A, 543, A13

Guo, Y., Ferguson, H. C., Bell, E. F., et al. 2015, ApJ, 800, 39

Guo, Y., Rafelski, M., Bell, E. F., et al. 2018, ApJ, 853, 108

Harris, W. E. 1996, AJ, 112, 1487

Hasselquist, S., Zasowski, G., Feuillet, D. K., et al. 2020, ApJ, 901, 109

Helmi, A., Babusiaux, C., Koppelman, H. H., et al. 2018, Nature, 563, 85-88

Hernandez, X., Valls-Gabaud, D., & Gilmore, G. 1999, MNRAS, 304, 705-719

Hopkins, P. F., Kereš, D., Murray, N., Quataert, E., & Hernquist, L. 2012, MNRAS, 427, 968-978

Horta, D., Schiavon, R. P., Mackereth, J. T., et al. 2020, MNRAS, 493, 3363-3378

Husser, T.-O., Latour, M., Brinchmann, J., et al. 2020, A&A, 635, A114

Immeli, A., Samland, M., Gerhard, O., & Westera, P. 2004a, A&A, 413, 547-561

—. 2004b, A&A, 413, 547-561

Immeli, A., Samland, M., Westera, P., & Gerhard, O. 2004c, ApJ, 611, 20-25

Johnson, C. I., & Pilachowski, C. A. 2010, ApJ, 722, 1373-1410

Johnson, C. I., Rich, R. M., Caldwell, N., et al. 2018, AJ, 155, 71

Johnson, C. I., Rich, R. M., Kobayashi, C., Kunder, A., & Koch, A. 2014, AJ, 148, 67

Joyce, M., Johnson, C. I., Marchetti, T., et al. 2023, ApJ, 946, 28

Kamann, S., Wisotzki, L., & Roth, M. M. 2013, A&A, 549, A71

Kerber, L. O., Libralato, M., Souza, S. O., et al. 2019, MNRAS, 484, 5530-5550

King, I. R. 1966, AJ, 71, 64

Kroupa, P. 2001, MNRAS, 322, 231-246

Kunder, A., Koch, A., Rich, R. M., et al. 2012, AJ, 143, 57

Kunder, A., Rich, R. M., Koch, A., et al. 2016, ApJ, 821, L25

Kurucz, R. L. 2005, Memorie della Societa Astronomica Italiana Supplementi, 8, 76

Lagioia, E. P., Milone, A. P., Stetson, P. B., et al. 2014, ApJ, 782, 50

Lanzoni, B., Dalessandro, E., Ferraro, F. R., et al. 2007, ApJ, 668, L139-L142

Lanzoni, B., Ferraro, F. R., Dalessandro, E., et al. 2010, ApJ, 717, 653-657

Lanzoni, B., Ferraro, F. R., Mucciarelli, A., et al. 2018a, ApJ, 865, 11

—. 2018b, ApJ, 861, 16

Lanzoni, B., Ferraro, F. R., Dalessandro, E., et al. 2019, ApJ, 887, 176

Leanza, S., Pallanca, C., Ferraro, F. R., et al. 2023, ApJ, 944, 162

Lee, Y. W., Joo, J. M., Sohn, Y. J., et al. 1999, Nature, 402, 55-57

Legnardi, M. V., Milone, A. P., Cordoni, G., et al. 2023, MNRAS, 522, 367-380

Majewski, S. R., Patterson, R. J., Dinescu, D. I., et al. 2000, in Liege International Astrophysical Colloquia, Vol. 35, Liege International Astrophysical Colloquia, ed. A. Noels, P. Magain, D. Caro, E. Jehin, G. Parmentier, & A. A. Thoul, 619

Majewski, S. R., Schiavon, R. P., Frinchaboy, P. M., et al. 2017, AJ, 154, 94

Mannucci, F., Cresci, G., Maiolino, R., et al. 2009, MNRAS, 398, 1915-1931

Marigo, P., Girardi, L., Bressan, A., et al. 2017, ApJ, 835, 77

Massari, D., Breddels, M. A., Helmi, A., et al. 2018, Nature Astronomy, 2, 156-161

Massari, D., Koppelman, H. H., & Helmi, A. 2019, A&A, 630, L4

Massari, D., Mucciarelli, A., Dalessandro, E., et al. 2012, ApJ, 755, L32

Massari, D., Mucciarelli, A., Ferraro, F. R., et al. 2014, ApJ, 795, 22

Massari, D., Dalessandro, E., Ferraro, F. R., et al. 2015, ApJ, 810, 69

Matteucci, F. 2012, Chemical Evolution of Galaxies

—. 2021, A&A Rev., 29, 5

Mauro, F., Moni Bidin, C., Chené, A. N., et al. 2013, , 49, 189-207

McKenzie, M., & Bekki, K. 2018, MNRAS, 479, 3126-3141

McWilliam, A., & Rich, R. M. 1994, ApJS, 91, 749

McWilliam, A., & Zoccali, M. 2010a, ApJ, 724, 1491-1502

—. 2010b, ApJ, 724, 1491-1502

Messa, M., Dessauges-Zavadsky, M., Richard, J., et al. 2022, MNRAS, 516, 2420-2443

Milone, A. P., Piotto, G., Bedin, L. R., et al. 2012, A&A, 540, A16

Minniti, D., Lucas, P. W., Emerson, J. P., et al. 2010, , 15, 433-443

Muñoz, C., Villanova, S., Geisler, D., et al. 2017, A&A, 605, A12

Muñoz, C., Geisler, D., Villanova, S., et al. 2018, A&A, 620, A96

Nataf, D. M., Udalski, A., Gould, A., Fouqué, P., & Stanek, K. Z. 2010, ApJ, 721, L28-L32

Nataf, D. M., Gould, A., Fouqué, P., et al. 2013, ApJ, 769, 88

Neichel, B., Lu, J. R., Rigaut, F., et al. 2014, MNRAS, 445, 500-514

Ness, M., Freeman, K., Athanassoula, E., et al. 2012, ApJ, 756, 22

—. 2013, MNRAS, 430, 836-857

Ness, M., Zasowski, G., Johnson, J. A., et al. 2016, ApJ, 819, 2

Neumayer, N., Seth, A., & Böker, T. 2020, A&A Rev., 28, 4

Noguchi, M. 1999, ApJ, 514, 77-95

Nogueras-Lara, F., Schödel, R., Gallego-Calvente, A. T., et al. 2020, Nature Astronomy, 4, 377-381

Norris, J. E., Freeman, K. C., & Mighell, K. J. 1996, ApJ, 462, 241

O'Donnell, J. E. 1994, ApJ, 422, 158

Origlia, L., Ferraro, F. R., Fusi Pecci, F., & Oliva, E. 1997, A&A, 321, 859-866

Origlia, L., Massari, D., Rich, R. M., et al. 2013, ApJ, 779, L5

Origlia, L., Rich, R. M., & Castro, S. 2002, AJ, 123, 1559-1569

Origlia, L., Valenti, E., & Rich, R. M. 2005, MNRAS, 356, 1276-1282

—. 2008, MNRAS, 388, 1419-1425

Origlia, L., Rich, R. M., Ferraro, F. R., et al. 2011, ApJ, 726, L20

Ortolani, S., Barbuy, B., Bica, E., et al. 2001, A&A, 376, 878-884

Ortolani, S., Bica, E., & Barbuy, B. 1993, ApJ, 408, L29

—. 1996, A&A, 306, 134

Pallanca, C., Beccari, G., Ferraro, F. R., et al. 2017, ApJ, 845, 4

Pallanca, C., Dalessandro, E., Ferraro, F. R., Lanzoni, B., & Beccari, G. 2013, ApJ, 773, 122

Pallanca, C., Ferraro, F. R., Lanzoni, B., et al. 2019, ApJ, 882, 159

Pallanca, C., Ransom, S. M., Ferraro, F. R., et al. 2014, ApJ, 795, 29

Pallanca, C., Dalessandro, E., Ferraro, F. R., et al. 2010, ApJ, 725, 1165-1169

Pallanca, C., Lanzoni, B., Ferraro, F. R., et al. 2021a, ApJ, 913, 137

Pallanca, C., Ferraro, F. R., Lanzoni, B., et al. 2021b, ApJ, 917, 92

Pallanca, C., Leanza, S., Ferraro, F. R., et al. 2023, ApJ, 950, 138

Pancino, E., Ferraro, F. R., Bellazzini, M., Piotto, G., & Zoccali, M. 2000, ApJ, 534, L83-L87

Pancino, E., Romano, D., Tang, B., et al. 2017, A&A, 601, A112

Patsis, P. A., Skokos, C., & Athanassoula, E. 2002, MNRAS, 337, 578-596

Pedregosa, F., Varoquaux, G., Gramfort, A., et al. 2011, Journal of Machine Learning Research, 12, 2825-2830

Pfeffer, J., Lardo, C., Bastian, N., Saracino, S., & Kamann, S. 2021, MNRAS, 500, 2514-2524

Pietrinferni, A., Cassisi, S., Salaris, M., & Castelli, F. 2004, ApJ, 612, 168-190

—. 2006, ApJ, 642, 797-812

Pietrukowicz, P., Kozłowski, S., Skowron, J., et al. 2015, ApJ, 811, 113

Piotto, G., Zoccali, M., King, I. R., et al. 1999, AJ, 118, 1727-1737

Popowski, P. 2000, ApJ, 528, L9-L12

Portail, M., Gerhard, O., Wegg, C., & Ness, M. 2017, MNRAS, 465, 1621-1644

Queiroz, A. B. A., Anders, F., Chiappini, C., et al. 2020, A&A, 638, A76

Queiroz, A. B. A., Chiappini, C., Perez-Villegas, A., et al. 2021, A&A, 656, A156

Raha, N., Sellwood, J. A., James, R. A., & Kahn, F. D. 1991, Nature, 352, 411-412

Raso, S., Pallanca, C., Ferraro, F. R., et al. 2019, ApJ, 879, 56

Rattenbury, N. J., Mao, S., Sumi, T., & Smith, M. C. 2007, MNRAS, 378, 1064-1078

Renzini, A., Gennaro, M., Zoccali, M., et al. 2018, ApJ, 863, 16

Rich, R. M., Reitzel, D. B., Howard, C. D., & Zhao, H. 2007, ApJ, 658, L29-L32

Robin, A. C., Reylé, C., Derrière, S., & Picaud, S. 2003, A&A, 409, 523-540

Rodrigo, C., & Solano, E. 2020, in XIV.0 Scientific Meeting (virtual) of the Spanish Astronomical Society, 182

Rodrigo, C., Solano, E., & Bayo, A. 2012, SVO Filter Profile Service Version 1.0, IVOA Working Draft 15 October 2012

Rojas-Arriagada, A., Recio-Blanco, A., Hill, V., et al. 2014, A&A, 569, A103

Rojas-Arriagada, A., Recio-Blanco, A., de Laverny, P., et al. 2017, A&A, 601, A140

Rojas-Arriagada, A., Zasowski, G., Schultheis, M., et al. 2020, MNRAS, 499, 1037-1057

Romano, D., Ferraro, F. R., Origlia, L., et al. 2023, ApJ, 951, 85

Ruiz-Lara, T., Gallart, C., Bernard, E. J., & Cassisi, S. 2020, Nature Astronomy, 4, 965-973

Ruiz-Lara, T., Gallart, C., Beasley, M., et al. 2018, A&A, 617, A18

Saha, A., Vivas, A. K., Olszewski, E. W., et al. 2019, ApJ, 874, 30

Saito, R. K., Zoccali, M., McWilliam, A., et al. 2011, AJ, 142, 76

Salaris, M., Chieffi, A., & Straniero, O. 1993, ApJ, 414, 580

Salpeter, E. E. 1955, ApJ, 121, 161

Saracino, S., Dalessandro, E., Ferraro, F. R., et al. 2015, ApJ, 806, 152

—. 2019, ApJ, 874, 86

Sbordone, L., Bonifacio, P., Marconi, G., & Buonanno, R. 2004, Mem. Soc. Astron. Italiana, 75, 396

Schiavon, R. P., Johnson, J. A., Frinchaboy, P. M., et al. 2017, MNRAS, 466, 1010-1018

Schultheis, M., Rojas-Arriagada, A., García Pérez, A. E., et al. 2017, A&A, 600, A14

Schultz, G. V., & Wiemer, W. 1975, A&A, 43, 133-139

Shen, J., Rich, R. M., Kormendy, J., et al. 2010, ApJ, 720, L72-L76

Shibuya, T., Ouchi, M., Kubo, M., & Harikane, Y. 2016, ApJ, 821, 72

Sneden, C., Gehrz, R. D., Hackwell, J. A., York, D. G., & Snow, T. P. 1978, ApJ, 223, 168-179

Sollima, A., Pancino, E., Ferraro, F. R., et al. 2005, ApJ, 634, 332-343

Stanek, K. Z., Udalski, A., SzymaŃski, M., et al. 1997, ApJ, 477, 163-175

Stephens, A. W., & Frogel, J. A. 2004, AJ, 127, 925-937

Stetson, P. B. 1987, PASP, 99, 191

—. 1994, PASP, 106, 250

Ströbele, S., La Penna, P., Arsenault, R., et al. 2012, in Society of Photo-Optical Instrumentation Engineers (SPIE) Conference Series, Vol. 8447, Adaptive Optics Systems III, ed. B. L. Ellerbroek, E. Marchetti, & J.-P. Véran, 844737

Surot, F., Valenti, E., Hidalgo, S. L., et al. 2019, A&A, 623, A168

Tacchella, S., Carollo, C. M., Renzini, A., et al. 2015, Science, 348, 314-317

Tolstoy, E., Hill, V., & Tosi, M. 2009, ARA&A, 47, 371-425

Tolstoy, E., & Saha, A. 1996, ApJ, 462, 672

Tosi, M., Greggio, L., Marconi, G., & Focardi, P. 1991, AJ, 102, 951

Ubeda, L., Anderson, J., & ACS Team. 2012, in American Astronomical Society Meeting Abstracts, Vol. 219, American Astronomical Society Meeting Abstracts #219, 241.03

Valcarce, A. A. R., Catelan, M., & Sweigart, A. V. 2012, A&A, 547, A5

Valenti, E., Ferraro, F. R., & Origlia, L. 2007, AJ, 133, 1287-1301

—. 2010, MNRAS, 402, 1729-1739

Valenti, E., Origlia, L., & Rich, R. M. 2011, MNRAS, 414, 2690-2695

Valenti, E., Zoccali, M., Renzini, A., et al. 2013, A&A, 559, A98

Valenti, E., Zoccali, M., Gonzalez, O. A., et al. 2016, A&A, 587, L6

Valenti, E., Zoccali, M., Mucciarelli, A., et al. 2018, A&A, 616, A83

VandenBerg, D. A., Stetson, P. B., & Brown, T. M. 2015, ApJ, 805, 103

Vanzella, E., Castellano, M., Bergamini, P., et al. 2022a, ApJ, 940, L53

—. 2022b, A&A, 659, A2

Vasiliev, E., & Baumgardt, H. 2021, MNRAS, 505, 5978-6002

von Braun, K., & Mateo, M. 2001, AJ, 121, 1522-1532

Wegg, C., & Gerhard, O. 2013, MNRAS, 435, 1874-1887

Wegg, C., Gerhard, O., & Portail, M. 2015, MNRAS, 450, 4050-4069

Weilbacher, P. M., Palsa, R., Streicher, O., et al. 2020, A&A, 641, A28

Weisz, D. R., Zucker, D. B., Dolphin, A. E., et al. 2012, ApJ, 748, 88

Zanella, A., Daddi, E., Le Floc'h, E., et al. 2015, Nature, 521, 54-56

Zasowski, G., Schultheis, M., Hasselquist, S., et al. 2019, ApJ, 870, 138

Zinnecker, H., Keable, C. J., Dunlop, J. S., Cannon, R. D., & Griffiths, W. K. 1988, in The Harlow-Shapley Symposium on Globular Cluster Systems in Galaxies, ed. J. E. Grindlay & A. G. D. Philip, Vol. 126, 603

Zoccali, M., & Valenti, E. 2016, , 33, e025

Zoccali, M., Valenti, E., & Gonzalez, O. A. 2018, A&A, 618, A147

Zoccali, M., Renzini, A., Ortolani, S., et al. 2003, A&A, 399, 931-956

Zoccali, M., Gonzalez, O. A., Vasquez, S., et al. 2014, A&A, 562, A66

Zoccali, M., Vasquez, S., Gonzalez, O. A., et al. 2017, A&A, 599, A12